ISSN: 2153-1196 Volume 10, Number 6, May 2019

Scientific Research Publishing

Journal of Modern Physics

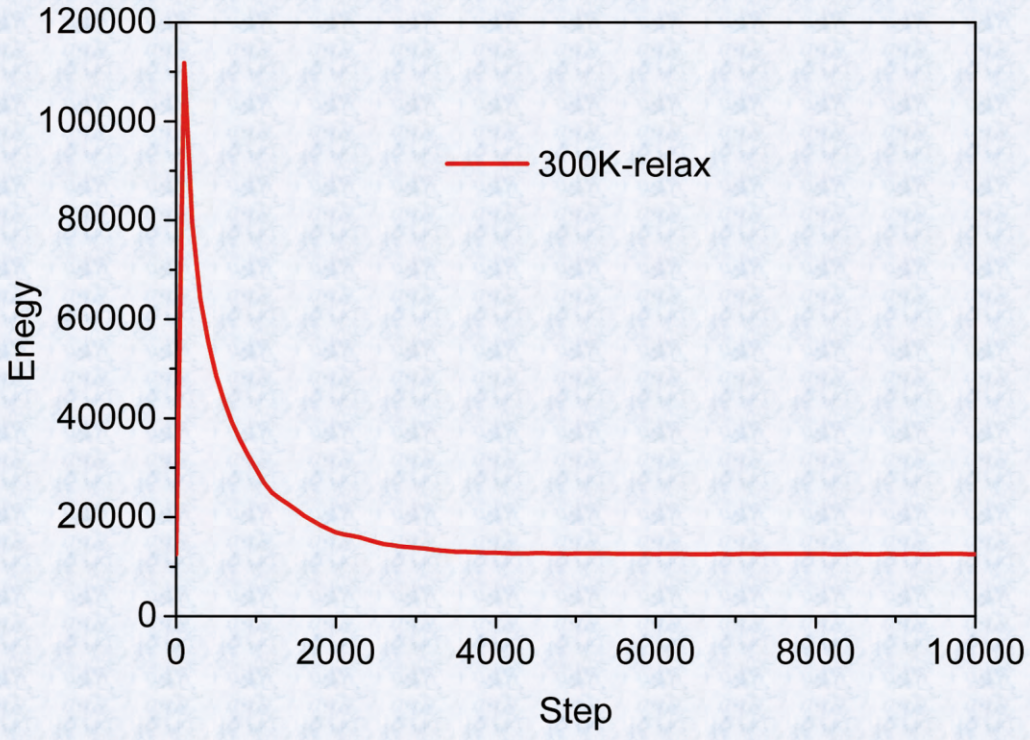

ISSN: 2153-1196
9 772153 119007 06

www.scirp.org/journal/jmp

Journal Editorial Board

ISSN: 2153-1196 (Print) ISSN: 2153-120X (Online)
http://www.scirp.org/journal/jmp

Editor-in-Chief

Editorial Board

Journal of Modern Physics, 2019, 10, 577-686
http://www.scirp.org/journal/jmp
ISSN Online: 2153-120X
ISSN Print: 2153-1196

Table of Contents

Volume 10 Number 6 May 2019

The figure on the front cover is from the article published in Journal of Modern Physics, 2019, Vol. 10, No. 6, pp. 577-584 by Jierong Guo and Lei Ma.

Journal of Modern Physics (JMP)
Journal Information

SUBSCRIPTIONS

The *Journal of Modern Physics* (Online at Scientific Research Publishing, www.SciRP.org) is published monthly by Scientific Research Publishing, Inc., USA.

Subscription rates:
Print: $89 per issue.
To subscribe, please contact Journals Subscriptions Department, E-mail: sub@scirp.org

SERVICES

Advertisements
Advertisement Sales Department, E-mail: service@scirp.org

Reprints (minimum quantity 100 copies)
Reprints Co-ordinator, Scientific Research Publishing, Inc., USA.
E-mail: sub@scirp.org

COPYRIGHT

PRODUCTION INFORMATION

For manuscripts that have been accepted for publication, please contact:
E-mail: jmp@scirp.org

Journal of Modern Physics, 2019, 10, 577-584
http://www.scirp.org/journal/jmp
ISSN Online: 2153-120X
ISSN Print: 2153-1196

Molecular Dynamics Simulation of Mechanical Properties for α-SiO_2 Crystal

Jierong Guo, Lei Ma

College of Mathematics and Physics Science, Hunan University of Arts and Science, Changde, China
Email: jierong_guo@126.com, mlml6277@126.com

How to cite this paper: Guo, J.R. and Ma, L. (2019) Molecular Dynamics Simulation of Mechanical Properties for α-SiO_2 Crystal. *Journal of Modern Physics*, **10**, 577-584.
https://doi.org/10.4236/jmp.2019.106040

Received: April 1, 2019
Accepted: April 23, 2019
Published: April 26, 2019

Abstract

The mechanical properties of the α-SiO_2 crystal are studied by molecular dynamics method with Tersoff potential function. The results show that the α-SiO_2 crystal goes through elastic deformation, plastic deformation and fracture deformation in the process of uniaxial loading at room temperature. The α-SiO_2 is from crystal phase transformation to amorphous phase in plastic deformation. And also by studying the influence of temperature on the tensile mechanical properties of α-SiO_2, it finds that the yield strength and elastic modulus of α-SiO_2 decrease gradually as the temperature increases. Moreover, the higher the temperature, the lower the fracture stress and fracture strain; the α-SiO_2 crystal is easy to be broke under high temperature uniaxial loading. And it also finds that the crack is able to decrease the mechanical properties of α-SiO_2 crystal.

Keywords

Mechanical Properties, Tensile, Molecular Dynamics

1. Introduction

The α-SiO_2 is the stable crystal at normal temperature. The research for α-SiO_2 crystal is mainly focused on the phase transition of amortization under high pressure. For example, Wang *et al.* [1] study the structural transformation of α-SiO_2 crystal under high temperature and high pressure, and point out that α-SiO_2 crystal is able to be synthesized on a small scale coesite under high temperature and high pressure. Palmer *et al.* [2] find the phase transition rule of α-SiO_2 by studying the pressurized phase transition process at room temperature. Zhang *et al.* [3] study the structural transformation of α-SiO_2 crystal at high temperature and high pressure and the experimental conditions of coesite formation through mechanical ball milling. Dubrovinsky *et al.* [4] study the

high-pressure phase transition of α-SiO_2, the results show that it obtains another phase structure of α-SiO_2 similar to the structure of α-PbO_2, and find that the stress between 25 GPa and 35 GPa resulting in an amorphous transformation, which is completely amorphous after unloading stress. However, with the rapid development of computer in recent years, it has become possible to study the mechanical properties, structural transformation and physical characteristics of crystal materials by means of large-scale parallel computation using molecular dynamics simulation [5] [6] [7] [8] [9]. For instance, Pan [10] simulates the high-pressure phase transition of α-SiO_2 with Morse potential using molecular dynamics simulation, and points out that the amorphous phase transition occurs when the stress of crystal is higher than 24.6 GPa, and the calculated results are in agreement with the experimental results. Therefore, computer simulations open up another effective way to study the mechanical properties of crystal, which can provide theoretical support for experimental research.

This paper is focused on investigating the basic mechanical properties of α-SiO_2 using molecular dynamics simulation. The stress-strain curves of α-SiO_2 have been studied with the temperature increasing. And the variation of yield stress, yield strain and elastic modulus is discussed for α-SiO_2 crystal in the process of uniaxial tension. The influence law of temperature on tensile mechanical properties is also discussed to comprehensively evaluate the mechanical properties of α-SiO_2. Meanwhile, it constructs the crack models of α-SiO_2 and analyzes the influence of crack on mechanical properties.

2. Atomistic Model and Simulation Method

Figure 1 shows the crystal structure of α-SiO_2. In silicon dioxide, silicon is located at the center of the tetrahedron, and four oxygen atoms are located at the four top angles of the tetrahedron. And then put the tetrahedron structure of SiO_2 into the body-center cubic and construct a crystal cell of α-SiO_2 as shown in Figure 1(A). Then the crystal structure of α-SiO_2 is established according to the Cartesian coordinates as shown in Figure 1(B). Where, the lattice constant a = 4.978 angstrom, b = 4.978 angstrom, c = 6.948 angstrom, the length of the box is $30a \times 30b \times 30c$, the total number of atoms is 324,000, and periodic boundary conditions are used in x-, y- and z-directions.

In molecular dynamics (MD) simulation, the Tersoff potential function [11] is adopted to describe the interaction between Si and O. the model is equilibrated under NPT ensemble at 300 k, and a Nose-Hoover thermostat is applied to maintain the system temperature. Figure 2 present the energy variation of the model in relaxation process, it can be obtained that the crystal model reaches the equilibrium after 10 ps. Then, the model is performed to uniaxial tensile test in z-direction using MD simulation with the time integration step of 1 fs under NPT ensemble. At the same time, the temperatures of 300 K, 500 K, 700 K and 900 K are selected to simulate the tensile mechanical properties of α-SiO_2 crystals at different temperatures. And the LAMMPS code [12] is applied to simulate the tensile mechanical properties.

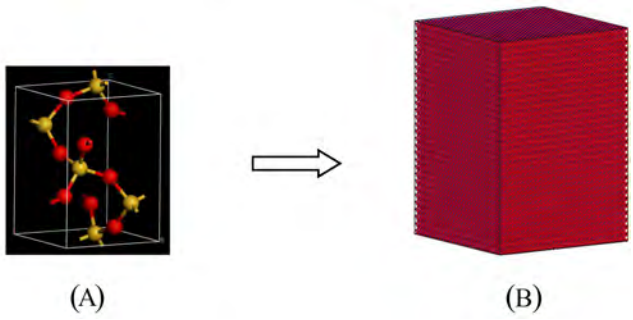

Figure 1. The initial model of α-SiO_2.

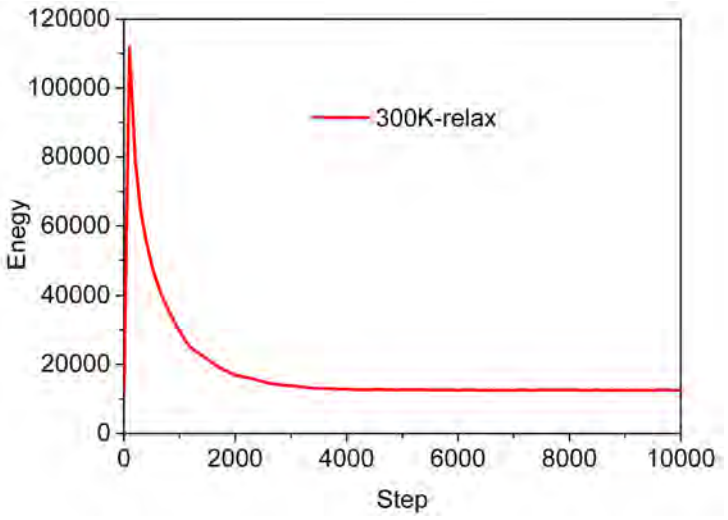

Figure 2. The energy variation of α-SiO_2 in relaxation process.

3. Results and Discussion

3.1. Analysis of Stress-Strain Curve

Figure 3 shows the stress-strain curve of α-SiO_2 under uniaxial tension at room temperature. The yield strain, yield stress, fracture strength and deformation characteristic and so on can be obtained by stress-strain curve, which can reflect the basic mechanical properties of the material. It can be seen from the Figure 3 that the elastic limit of α-SiO_2 crystal appears when the strain is up to 4.7% (as shown in Figure 3(A)), and the stress-strain curve present non-linear relationship. After A, the α-SiO_2 crystal enters the elastic deformation stage. When the strain is up to 32.6%, the stress reaches the first yield point, the yield stress is 22.6 GPa. Then the α-SiO_2 crystal enters the plastic deformation stage, the stress oscillates between point B and point C with the strain increasing, this moment the nanocrystal appears amorphous phase transition. When the stress passes C in Figure 3, the crystal structure is completely amorphous, the stress reaches the peak value—fracture strength (36 GPa), the α-SiO_2 crystal enter the stage of fracture. Then the stress falls rapidly to zero as the strain increases and the crystal breaks completely. It can be seen from the Figure 3 that α-SiO_2 crystal experiences the elastic stage, the plastic stage (amorphous phase transition) and the

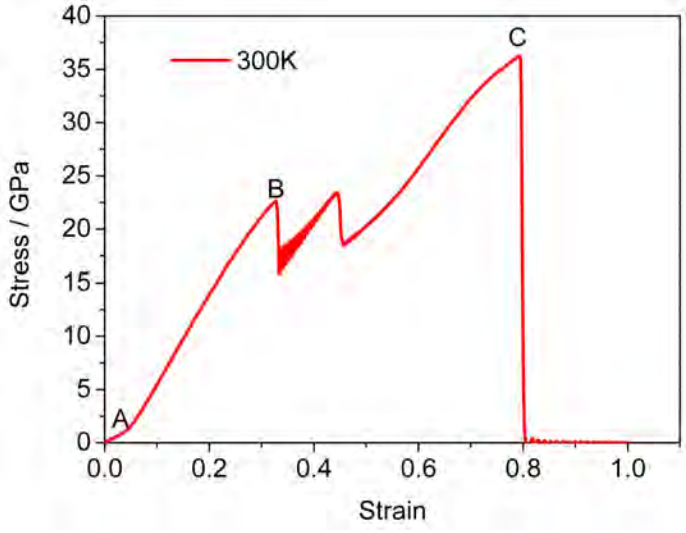

Figure 3. The stress-strain curve of α-SiO_2 in uniaxial tension at room temperature.

fracture stage during the uniaxial tensile process at room temperature, and the elastic modulus reached 69 GPa, so the α-SiO_2 crystal has excellent strength.

3.2. Temperature Effect

In order to discuss the influence of temperature on the tensile mechanical properties of the α-SiO_2 crystal, on the basis of room temperature, the temperatures of 500 K, 700 K and 900 K are selected, and then the mechanical properties of α-SiO_2 crystals are simulated at different temperatures. **Figure 4** shows the variation of the stress-strain curves of the α-SiO_2 crystal at different temperatures. The simulation results show that the yield stress and yield strain decrease with the increasing of temperature. It indicated that the higher the temperature is, the shorter the elastic deformation stage of α-SiO_2 crystal is, and the loading strain of achieving yield strength is smaller. Meanwhile, **Table 1** shows the mechanical parameters of α-SiO_2 under uniaxial tensile at different temperatures, the results present that the elastic modulus decreases gradually with the increasing of temperature. From the data of the calculated elastic model in **Table 1**, the elastic modulus of α-SiO_2 crystal is reduced by 2.3 GPa when the temperature increase from 300 K to 500 K. As the temperature rise from 500 K to 700 K, the elastic modulus of α-SiO_2 crystal is reduced by 1.34 GPa. The elastic modulus decreases by 1.26 GPa as the modulus increases from 700 K to 900 K. It can be concluded that although the elastic modulus of α-SiO_2 crystal decreases as a result of high temperature, but there is no large range of decrease. Therefore, the high temperature only slightly reduces the strength of the α-SiO_2 crystal and does not have much influence on the overall strength.

However, the temperature has a great influence on the fracture strength of the α-SiO_2 crystal. **Figure 5** shows the variation curves of fracture stress and fracture strain at different temperatures. As can be seen from the **Figure 5**, the fracture stress decreases from 36 GPa to 29 GPa with the increasing of temperature,

Table 1. Mechanical parameters of uniaxial tensile of α-SiO_2 at different temperatures.

α-SiO_2	ε_{yield} (GPa)	σ_{yield} (GPa)	E (GPa)
300 K	0.326	22.6	69.32
500 K	0.287	19.24	67.03
700 K	0.274	18.00	65.69
900 K	0.223	14.37	64.43

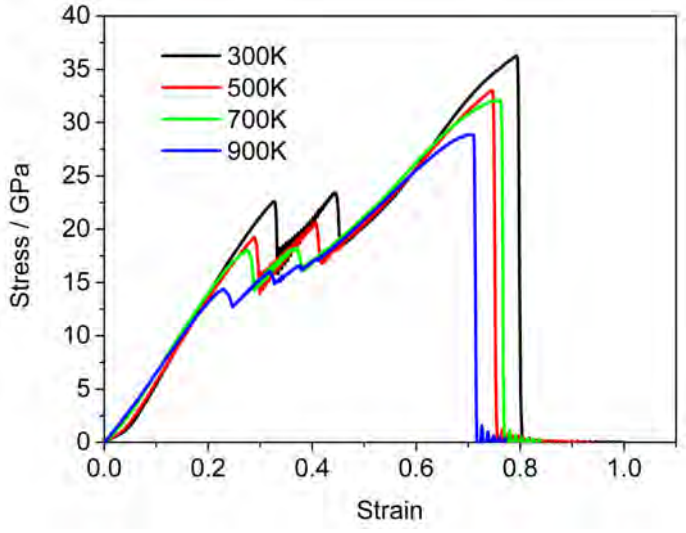

Figure 4. The tensile stress-strain curve of α-SiO_2 at different temperatures.

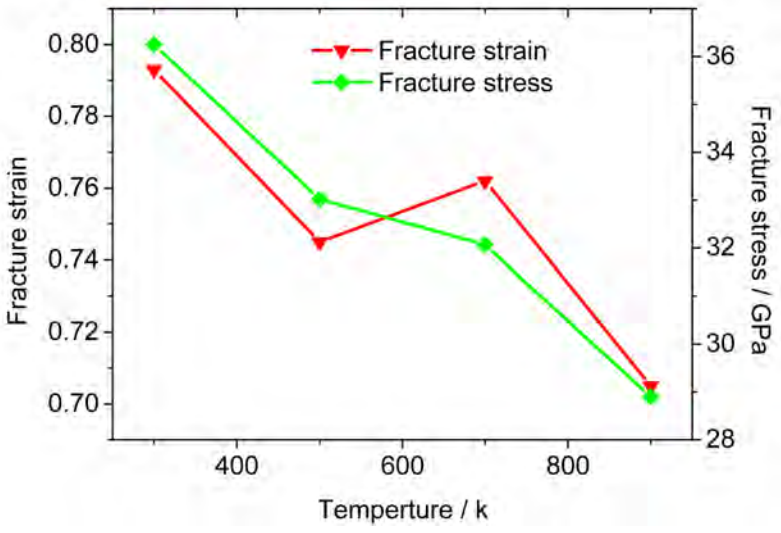

Figure 5. The fracture stress and fracture strain for α-SiO_2 at different temperatures.

which shows a straight downward trend. Although the fracture strain rebound in the process of decreasing with the increasing of temperature, the overall state is also in decline. Therefore, it can be concluded that the higher the temperature is, the lower the fracture stress and fracture strain are, and it is the more easily fracture for α-SiO_2 crystal under high temperature uniaxial loading.

3.3. The Mechanical Properties of Crack Propagation in α-SiO_2 Crystal

In order to discuss the influence of crack on mechanical properties of α-SiO_2 crystal, we construct a crack model by deleting some atoms in α-SiO_2 crystal as shown in Figure 6, and the initial crack length is 2.98 nm. This crack model is then uniaxial stretched for studying the effect of crack on mechanical properties. Figure 7 shows the stress-strain curve of α-SiO_2 crack model at different temperatures. The results present that the yield stress and yield strain decrease with the temperature increasing as shown in Figure 7, the reason is that the crack propagation rate increase with the temperature increasing so that the internal structure is seriously damage at high temperature. Compared to the perfect crystal of α-SiO_2, as the temperature increase from 300 K to 700 K, the crack leads to decreasing of yield stress and yield strain. But the crack model has relatively larger yield stress and yield strain at 900 K, which indicate that the high temperature cause the structure softening so that the crack appear collapse and inhibit the crack rapid propagation.

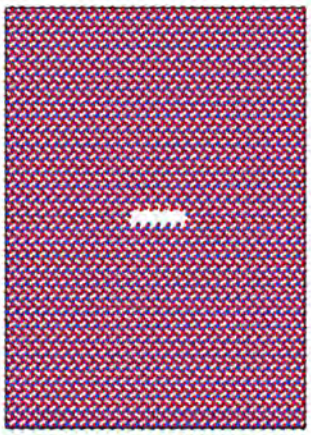

Figure 6. The crack model of α-SiO_2.

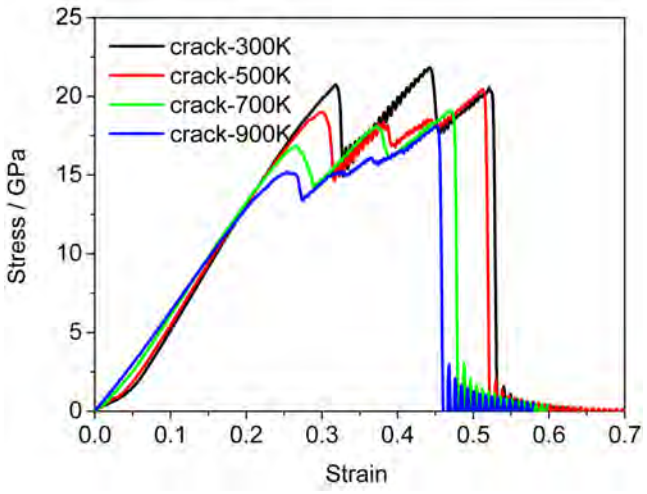

Figure 7. The tensile stress-strain curve of α-SiO_2 crack model at different temperatures.

Table 2. Mechanical parameters of crack model of α-SiO_2 at different temperatures.

α-SiO_2	ε_{yield} (GPa)	σ_{yield} (GPa)	E (GPa)
300 K	0.31	20.7	66.77
500 K	0.30	18.9	62.33
700 K	0.26	16.8	64.61
900 K	0.26	15.1	58.07

And the elastic modulus is obtained by fitting the stress-strain curve of the α-SiO_2 crack model. The calculated values show in Table 2, which present that the elastic modulus of α-SiO_2 crack model vary from 66 GPa to 58 GPa as the temperature arising. Compared to the perfect crystal of α-SiO_2, the elastic modulus of crack model is decreasing at each temperature. So the crack causes the mechanical properties to drop.

4. Conclusion

The tensile mechanical properties of α-SiO_2 crystal are simulated by means of molecular dynamics and with Tersoff potential function. The results show that the α-SiO_2 crystal goes through elastic deformation, plastic deformation and fracture deformation in the process of uniaxial loading at room temperature, and the yield strength is 22.6 GPa, the fracture strength is 36 GPa. The α-SiO_2 is from crystal phase transformation to amorphous phase transition in plastic deformation. And also by studying the influence of temperature on the tensile mechanical properties of α-SiO_2, it finds that the yield strength and elastic modulus of α-SiO_2 decrease gradually as the temperature increases. Moreover, the higher the temperature, the lower the fracture stress and fracture strain; the α-SiO_2 crystal is easy to be broke under high temperature uniaxial loading. The yield stress and yield strain decrease with the temperature increases. For the crack model of α-SiO_2, the yield stress and yield strain decrease with the temperature increases comparing to the perfect crystal of α-SiO_2, and the crack causes the mechanical properties to drop.

Acknowledgements

This work is supported by Hunan natural science foundation (No. 2016JJ5002) and the Doctor Start project of Hunan University of Arts and Science (No. 16BSQD05).

Conflicts of Interest

The authors declare no conflicts of interest regarding the publication of this paper.

References

[1] Wang, D.J. (2010) A Study on the Structure Transition of α-Quartz under High

Temperature and High Present. *Journal of Changchun University*, **20**, 14-16.

[2] Palmer, D.C., Hemley, R.J. and Prewitt, C.T. (1994) Raman Spectroscopic Study of High-Pressure Phase Transitions in Cristobalite. *Physics and Chemistry of Minerals*, **21**, 481-488. https://doi.org/10.1007/BF00203922

[3] Zhang, G.Q., Xe, D.P., Wang, D.O., *et al.* (2008) Structural Transition of Nanometer SiO2 Powders under High Pressure and High Temperature. *Journal of Jilin University*, **46**, 311-313.

[4] Dubrovinsky, L.S., Dubrovinskaia, N.A., Saxena, S.K., *et al.* (2001) Pressure-Induced Transitions of Cristobalite. *Chemical Physics Letter*, **333**, 264-270. https://doi.org/10.1016/S0009-2614(00)01147-7

[5] Wang, K., Xiao, S.F., Deng, H.Q., *et al.* (2014) An Atomic Study on the Shock-Induced Plasticity and Phase Transition for Iron-Based Single Crystals. *International Journal of Plasticity*, **59**, 180-198. https://doi.org/10.1016/j.ijplas.2014.03.007

[6] Ma, L., Xiao, S.F., Deng, H.Q. and Hu, W.Y. (2014) Molecular Dynamics Simulation of Fatigue Crack Propagation in Bcc Iron under Cyclic Loading. *International Journal of Fatigue*, **68**, 253. https://doi.org/10.1016/j.ijfatigue.2014.04.010

[7] Ma, L., Xiao, S.F., Deng, H.Q. and Hu, W.Y. (2015) Atomic Simulation of Fatigue Crack Propagation in Ni3Al. *Applied Physics A*, **118**, 1399-1406. https://doi.org/10.1007/s00339-014-8895-0

[8] Ma, L., Xiao, S.F., Deng, H.Q. and Hu, W.Y. (2016) Tensile Mechanical Properties of Ni-Based Superalloy of Nanophases Using Molecular Dynamic Simulation. *Physica Status Solid*, **253**, 716-732. https://doi.org/10.1002/pssb.201552149

[9] Ma, L., Zhong, Y. and Wen, X.X. (2011) Process in Nanocrystalline Metal under Tensile Stress. *Materials Review*, **25**, 10-13.

[10] Pan, H.B. (200) A New Phase Transition of Quartz-α SiO2 by Molecular by Dynamics Simulation. *Acta Mineralogica Sinica*, **21**, 511-514.

[11] Teodoro Laino, M., *et al.* (2007) Interatomic Potential for Si-O Systems Using Tersoff Parameterization. *Computational Materials Science*, **39**, 334-339. https://doi.org/10.1016/j.commatsci.2006.06.010

[12] http://lammps.sandia.gov

Journal of Modern Physics, 2019, 10, 585-600
http://www.scirp.org/journal/jmp
ISSN Online: 2153-120X
ISSN Print: 2153-1196

Interval Based Analysis of Bell's Theorem

F. P. Eblen[1], A. F. Barghouty[2]

[1]Advanced Communications and Navigation Technology Division, Space Communications and Navigation (SCaN) Program, Human Exploration and Operations Mission Directorate, NASA Headquarters, Washington DC, USA
[2]Astrophysics Division, Science Mission Directorate, NASA Headquarters, Washington DC, USA
Email: pat.eblen@nasa.gov

How to cite this paper: Eblen, F.P. and Barghouty, A.F. (2019) Interval Based Analysis of Bell's Theorem. *Journal of Modern Physics*, **10**, 585-600.
https://doi.org/10.4236/jmp.2019.106041

Received: March 28, 2019
Accepted: May 5, 2019
Published: May 8, 2019

Abstract

This paper introduces the concept and motivates the use of finite-interval based measures for physically realizable and measurable quantities, which we call $\mathcal{D}$-measures. We demonstrate the utility and power of $\mathcal{D}$-measures by illustrating their use in an interval-based analysis of a prototypical Bell's inequality in the measurement of the polarization states of an entangled pair of photons. We show that the use of finite intervals in place of real-numbered values in the Bell inequality leads to reduced violations. We demonstrate that, under some conditions, an interval-based but otherwise classically calculated probability measure can be made to arbitrarily closely approximate its quantal counterpart. More generally, we claim by heuristic arguments and by formal analogy with finite-state machines that $\mathcal{D}$-measures can provide a more accurate model of both classical and quantal physical property values than point-like, real numbers—as originally proposed by Tuero Sunaga in 1958.

Keywords

Measurement Theory, Bell's Theorem, Bell's Inequality, Interval-Based Analysis, Interval-Based Physical Measures

1. Introduction

We present first two heuristic arguments, followed by theoretical and numerical demonstrations, to support motivation of a concept to replace point-like real-numbered physical property values with intervals of value we call $\mathcal{D}$-measures, which may be weighted by some function. The exact nature of the weighting is not crucial, however, to the interval-based representation. In Sect. 1.1, we show how these arguments suggest that the conventionally assumed assignment of real numbers to represent physical property values may not be tenable (see, e.g., [1]), and instead $\mathcal{D}$-measures can provide more accurate models

of manifest physical reality. In Sect. 1.2, we introduce the concept of finite intervals as defined and practiced in computing theory. In Sect. 2, we apply the $\mathcal{D}$-measure concept to a new analysis of Bell's theorem using well established interval-analysis theorems to show that violations of the classically derived Bell's inequality may thereby be reduced to expectations arbitrarily approaching their quantum prediction counterparts that are consistent with results of Bell tests. In Sect. 3, we offer concluding, general remarks highlighting how the use of finite intervals to represent physically measurable quantities may have significant impact on analysis of physical systems, both classical and quantal, and how, in particular, the new results derived from interval-based analysis may also impact technologies based on them.

1.1. $\mathcal{D}$-Measure Description of a Physically Measurable Quantity

Measurement of any physical property value and generic manifestation of any physical property value are equivalent processes at some fundamental level. This equivalence is foundational to environmental decoherence theory since certain manifestations of value are physically realized[1] via "implicit measurement" of objects by the environment in which they exist [2]. This is precisely the essence of the equivalence claim, that object properties become physically manifest by unavoidable implicit measurement resulting from any and every interaction. This means that certain attributes of any process to measure physical values are common attributes of any generic process of manifestation of physical values. For example, all physically realizable measurements are performed using resolution-limited devices and processes, so generic manifestation of physical values are equally resolution-limited. Therefore, no physically realizable measurement and no physically realizable manifestation of any physical property value are expected to be represented by a single, point-like, real number. Such an assignment would require realization of infinite (physical) resolution. Infinite resolution is clearly untenable, and hence, a non-physical abstraction. This suggests that any assignment that relies on a finite resolution can only be manifest as finite intervals of values, *i.e.*, "$\mathcal{D}$-measures".

From a communication theoretic point of view, suppose a communication signal could have a producible and detectable parameter represented by a real number. Since real numbers are infinitely precise and can be represented mathematically [1] only by an infinite number of digits, such a signal would contain an infinite amount of information. Conveyance of this signal from one point to another would constitute an infinite change of entropy, or an exchange of infinite information [3], in a finite time through a finite spectral width channel, which is not physically possible, even if the channel were noise-free. Therefore

[1]We use the term "physically realized", while admittedly not rigidly definable, because it offers a working definition of the notion of a physically realized entity as one that can exist in and have influence on physical reality, while having physical properties that are, in principle, measurable by a physical device. It is to be contrasted with an abstracted physical property, which may be formally useful but may not be measurable by a physical device.

the signal parameter cannot be validly represented by a single real number. A $\mathcal{D}$-measured parameter, on the other hand, has finite precision and finite information content, requiring a finite spectral width and finite time to convey. Further, the physics principle known as the Bekenstein bound [4] dictates that infinite entropy, or information, cannot exist in a finite region of space with finite energy, which can be interpreted as precluding both production and detection of any signal with a real-numbered parameter. It is interesting to note that $\mathcal{D}$-measures are "naturally" endowed with interval entropy and related information content [5].

Using these and other similar arguments, we assert that realizable and measurable property values are more accurately modeled by $\mathcal{D}$-measures than by point-like real-numbered values of zero measure. We further assert that $\mathcal{D}$-measures apply to both classical and quantal physically realizable values. At some level, the interval ($\mathcal{D}$-measure) model is in conflict with the convention of classical physics to assume measurable property values are mathematically represented by real numbers; this conventional representation may be too restrictive.

The conflict is perhaps less pronounced for quantal measurement outcomes due to the intrinsic uncertainties and ambiguities in a quantal description, but there is a critical difference in $\mathcal{D}$-measured quantal superposition and conventional quantal superposition: $\mathcal{D}$-measured outcome values, even when weighted by some appropriate function, are not envisaged to be associated with a probability metric across eigenvalues. Because $\mathcal{D}$-measure intervals apply to each single measurement, or manifestation of value, the eigenvalues within an interval are assumed associated with a non-statistical ontic metric. While the exact definition and meaning of this ontic metric is not yet clear (and the subject of a follow-on paper), the assertion that it is non-statistical means that single measurement outcomes have distributed value, *i.e.*, they are $\mathcal{D}$-measures. This interval-based representation suggests that all realizable quantum states that result from measurement are comprised of simultaneously physically existing eigenstates. Every physically realizable quantum state is a superposition of multiple states in every realizable basis, *i.e.*, a basis with physically measurable eigenvalues. A $\mathcal{D}$-measured state cannot be represented by a single, real-numbered direction in an abstract space of realizable eigenvalues.

$\mathcal{D}$-measured quantum state definitions open the opportunity to form an entropy metric calculated just like Shannon information entropy [2] is calculated from a symbol alphabet probability density function, *i.e.*, $-\int \mathrm{d}x f(x)\log f(x)$, where $f(x)$ is defined as the modulus squared of a state vector as a function of x eigenvalues. A critical difference in a $\mathcal{D}$-measured entropy, however, is that the function value is an ontic, or physical, metric as opposed to an epistemic, or informational/probability, metric. This is because the eigenstates of a $\mathcal{D}$-measured state are treated as simultaneously physically existing eigenstates in superposition, yet the entropy of the state can never be zero [4] in any realizable basis

since this would require a single real-numbered eigenvalue, a non-realizable entity in the $\mathcal{D}$-measure concept (see, e.g. [6]).

Application of $\mathcal{D}$-measures to physical values is analogous to the application of intervals to the values typical of finite-state machines, which are incapable of specifying or processing real-numbered values. The application of interval analysis herein to all physically realizable property values is likewise suggested for fundamentally similar reasons. Physical objects, systems of objects, and processes, such as classical and quantum measurement, are limited in their ability to manifest real-numbered property values by parameters such as spectral limits, process and time limits, and various other constraints. Both classical and quantal physically realizable objects and systems thus can be viewed in some sense as finite-state machines.

1.2. $\mathcal{D}$-Measures Represented by Finite Intervals

The mathematical formalism of interval analysis was developed and has seen its primary application in computing theory for numerical analysis and mathematical modeling. It is a relatively recent cross-disciplinary field pioneered by M. Warmus [7], T. Sunaga [8], R. Moore [9], and U. Kulisch [10]. (For these and other early contributions, see [11]). According to [11], it was Sunaga [8] who first foresaw the fundamental connection between the mathematical concept of an interval and its applications to real systems and applied analysis. Applications to the physical sciences have thus far been extremely limited, however, to studies of formal systems through the "intervalization" of their representative differential or algebraic equations [12] [13].

The need for the concept of an interval was spawned by the need in the above numerical applications to enclose a real number when it can be specified only with limited accuracy, *i.e.*, it cannot be exactly represented on any finite-precision machine. In physical systems, inaccuracy in measurement coupled with known or unknown uncertainty and variability in physical parameters, initial and boundary conditions, etc., formally inhibit the manifestation of measurable quantities as real numbers, to be treated via the machineries of real numbers' arithmetic and algebra. Special axioms and special interval arithmetic and algebra were clearly needed to endow the new field with rigorous mathematical foundations.

In numerical analysis, finite intervals of one or more dimensions are seen as extensions of real (or complex) numbers. As mathematical objects, intervals in themselves do not form proper vector spaces [14] [15]. Interval arithmetic and interval algebra have nonetheless been developed by abstracting their real-numbered counterparts, based primarily on set theory and algebraic geometry [16]. However, compared to real-number objects, intervals have "extended" properties. As we demonstrate below, these properties provide for a powerful analytical tool in the description and/or analysis of *real* physical systems when property values are represented by $\mathcal{D}$-measures.

2. Application to Bell's Theorem

In Sect. 2.1, we demonstrate how, under some conditions, an intervalized but otherwise classically calculated correlation function can be made to arbitrarily come close to its quantal counterpart. The demonstration is essentially a re-casting using intervals and interval analysis of a limiting case derived by Bell [17]. Using proxies of the interval-valued correlation functions, and using two basic theorems of interval analysis suggest that, under some conditions, the two can be made to come arbitrarily close to each other. In Sect. 2.2, we test this assertion by applying it to a prototypical measurement of the polarization states of an entangled pair of photons.

2.1. Theoretical Illustration

We demonstrate in this section the validity of the following assertion: Expressed as interval-valued functionals, as opposed to real number-valued functions, the distance between a classically calculated correlation function, of two measured interval quantities, and its quantal counterpart can be shown (under some conditions) to arbitrarily approach zero.[2]

Let the two measured interval-variables be $X=\left[X_{\min},X_{\max}\right]$ and $Y=\left[Y_{\min},Y_{\max}\right]$, where we assume that both are one-dimensional intervals (generalization to higher dimensions may not be trivial, see, e.g., [18]). We denote their real-numbered values, *i.e.*, their degenerate values, as x and y, and the unit vectors along their directions by $\hat{x}$ and $\hat{y}$. By definition, a classically calculated correlation function of X and Y, $C_{X,Y}^{cl}\left(\hat{x},\hat{y};\lambda\right)$, will always involve a weighted sum over the parameter λ of their inner product. For the sake of this demonstration we do not distinguish between a Riemann and a Lebesque integration; we only assume the existence of an integrable real-valued function or functional. Its quantal counterpart, assuming an entangled single state, is a dot product (in the same metric space), which can be expressed as $-\hat{x}\cdot\hat{y}$. For real-valued inner and dot products, it has been shown [17], Equation (18), that

$$\left|C_{x,y}^{cl}\left(\hat{x},\hat{y};\lambda\right)+\left(\hat{x}\cdot\hat{y}\right)\right|\le\epsilon, \tag{1}$$

where ϵ is a small number but which cannot be made arbitrarily small, *i.e.*, will always be bounded from below due to the finite precision of any physical measurement. Our demonstration of the assertion made above is essentially a recast of Equation (1) in its interval analog for intervals X and Y, but in which the analog of ϵ is shown that it can be made arbitrarily small. The conditions pertain to our assumed low dimensionality of the intervals and of the unit vectors, in addition to the assumed forms of the inner and dot products, our proxy correlation functions.

In lieu of the inner product, we will have an interval-valued integral function, or a functional, and in lieu of the dot product for unit vectors, an assumed interval-valued functional related to the range of the first. The interval analog of

[2]By "demonstration" we mean here that what follows is neither a rigorous nor a general validation of the above assertion.

the inner product can be written as

$$C_{X,Y}^{cl}\left(\hat{x},\hat{y};\lambda\right)=\left[\int_{[Z],lower}\partial C_{X,Y}^{cl},\int_{[Z],upper}\partial C_{X,Y}^{cl}\right], \tag{2}$$

where *lower* and *upper* refer to the lower and upper Darboux integrals [13]. It is important to note that

$$\int_{[Z]}\partial C_{x,y}^{cl}\in\int_{[Z]}\partial C_{X,Y}^{cl} \tag{3}$$

over the same interval "$[Z]$", which follows from our assumed interval-extension of $C_{x,y}^{cl}$. Although generalization to an extended λ is straightforward and could present interesting cases for further analysis, for purposes of this demonstration, we take the parameter λ to be the same in both the real-numbered valued and interval-valued cases. Since the interval $[Z]=[X][Y]$ has a range $[-1,+1]$, $C_{X,Y}^{cl}$ can be written as:

$$C_{X,Y}^{cl}=Z\times F\left([Z]\right), \tag{4}$$

where $F\left([Z]\right)$ is a functional of Z. Note that the above form for $C_{X,Y}^{cl}$ is not unique; as uniqueness is not required for this demonstration. Also, the exact form of the interval-valued function F is not required, but that it is analytic and convergent over an interval Z^0 that includes Z, and over which interval the derivative of F exists and does not contain zero. These general properties [13] follow since F is assumed to be an "extension" of the real-valued function f, *i.e.*, the integral function that gives $C_{x,y}^{cl}$; since,

$$\left|f(x)-f(y)\right|\le \text{const}\left|x-y\right| \text{ for } x,y\in Z^0, \tag{5}$$

we have for F,

$$d\left(F\left([Z]\right)\right)\le \text{const}\, d(Z) \text{ for } Z\subseteq Z^0, \tag{6}$$

where $d(\cdot)$ denotes the diameter (or width) of its interval argument.

A fundamental property of any extended function, F, of an interval is its "enclosure" property, *i.e.*,

$$\mathcal{R}\left(F;[Z]\right)\subseteq F\left([Z]\right), \tag{7}$$

where $\mathcal{R}\left(F;[Z]\right)$ is the range of the function F over the interval $[Z]$, $F\left([Z]\right)$ is now a "functional" of the interval $[Z]$, and "$\subseteq$" denotes "a subset of". Almost all derived properties of intervals, including their mapping, differentiation and integration, differential (or integral) equations-based applications are based on the enclosure property [12] [13]. We will use this property below.

The extended functional $F\left([Z]\right)$ is further assumed divisible into smaller subintervals, where it can be regarded as the union of these subintervals,

$$F\left([Z];k\right)=\bigcup_{\ell=1}^{k}F\left([Z]^{\ell}\right), \tag{8}$$

and where *smaller* refers to the diameter of each sub-interval Z^{ℓ} being reduced by the factor $\ell=1,2,\cdots,k$.

For the interval-valued dot product of the unit vectors, being a projection of

one unit vector onto the other, and since the range is also $[-1,+1]$, we make the ansatz and connect this with the functional F via its range,

$$(\hat{x}\cdot\hat{y}) = \text{const}\,\mathcal{R}(F;[Z]), \tag{9}$$

or with any linear function of $\mathcal{R}(F;[Z])$, where $\mathcal{R}(F;[Z])$ is the range of F over the interval Z. Again, this relation is not unique for $\hat{x}\cdot\hat{y}$.

Next, we take advantage of two basic theorems of interval analysis [9] [12]. The first concerns the distance between two intervals, also referred to as the Hausdorff distance [12], $\mathcal{Q}$. For our demonstration, the distance between $\mathcal{R}(F;[Z])$ and $F([Z])$ is given by:

$$\mathcal{Q}(\mathcal{R}(F;[Z]),F([Z])) \le \text{const}\,\|d([Z])\|_\infty, \tag{10}$$

where $d(F([Z])) \le \text{const}\,\|[Z]\|_\infty$, and the constants ≥ 0. $\|\cdot\|_\infty$ denotes the maximum norm. Applied to the subdivided $F([Z];k)$, the Hausdorff distance becomes

$$\mathcal{Q}(\mathcal{R}(F;[Z]),F([Z];k)) \le \text{const}\,\|d([Z^0])\|_\infty^2 / k^2. \tag{11}$$

What the above theorem suggests is that $\mathcal{R}(F;[Z])$, our proxy for the intervalized dot product, can be arbitrarily close to $F([Z];k)$, our proxy for the intervalized inner product, if the subdivision of $F([Z])$ is made sufficiently fine. Clearly, this is only true under the conditions (*i.e.*, low dimensionality of the intervals and the unit vectors) and assumptions made (*i.e.*, the assumed specific forms of the inner and dot products). Applications to different forms and/or any generalization are clearly beyond the scope of the assertion.

2.2. Numerical Illustration

Our first application of the $\mathcal{D}$-measure concept is to an interval-based analysis of a prototypical [19] [20] form of Bell's inequality [17] [21]. The quantum-mechanical probability for a measurement of the polarization states of an entangled pair of photons can be shown to be proportional to the cosine (or sine) squared of the measured polarization angles [21]. (See **Appendix** for an illustrated structure of a prototypical Bell test using the entangled spin states case, which is, in essence, the same as the polarization states but easier to illustrate.) If θ_1 is the measured polarization angle detected by detector 1 of photon 1, and similarly for θ_2, the probability of detecting a photon along the 2-dimensional axes, $x-y$, of each detector is

$$p_{xy} \propto \sin^2(\theta_1-\theta_2) \text{ or } \propto \cos^2(\theta_1-\theta_2) \tag{12}$$

for each of the four possible combinations that add up to unity. When a third detector is introduced, a Bell's inequality can constrain the degree of polarization correlation among the angular separations in such a way that

$$\sin^2(\theta_2-\theta_1)+\sin^2(\theta_3-\theta_2) \ge \sin^2(\theta_3-\theta_1). \tag{13}$$

To intervalize Equation (13), we re-express the measured angles, θ_1, θ_2, and

θ_3 as angle intervals, $\Theta_1 = [\theta_1 - \delta\theta_1, \theta_1 + \delta\theta_1]$, $\Theta_2 = [\theta_2 - \delta\theta_2, \theta_2 + \delta\theta_2]$ and $\Theta_3 = [\theta_3 - \delta\theta_3, \theta_3 + \delta\theta_3]$, where $\delta\theta_i$ is the total uncertainty in measuring θ_i, *i.e.*, including all system and random errors in the set-up and the measuring devices. Note that in the limit of $\delta\theta_i \to 0$, $\Theta_1 = [\theta_i, \theta_i]$, *i.e.*, it is a degenerate interval. Being a statement about probability measures and their correlations, the form of Equation (2) is retained when expressed as

$$\sin^2(\Theta_3 - \Theta_1) \subseteq \sin^2(\Theta_2 - \Theta_1) + \sin^2(\Theta_3 - \Theta_2). \tag{14}$$

Intervalized, Equation (14) suggests that the interval $\sin^2(\Theta_2 - \Theta_1) + \sin^2(\Theta_3 - \Theta_2)$ will always include the interval $\sin^2(\Theta_3 - \Theta_1)$. Note that the sine of an interval is also an interval since the sine function will map every point in the interval argument to a point in the interval image of the function.

The enclosure property, Equation (7), can be used, as an example, to show that

$$\sin^2(\Theta_3 - \Theta_1) \subseteq \sin(\Theta_3 - \Theta_1) \times \sin(\Theta_3 - \Theta_1). \tag{15}$$

Another intriguing property of interval functionals is their dependence on the algebraic form or structure of the enclosing function *f*, or its extended pair *F*. This dependence stems from the set-theoretic attributes of intervals. For example, another form of Equation (14) that is equivalent for degenerate intervals, *i.e.*, real numbers, but is not for finite intervals is

$$\begin{aligned} &\sin^2(\Theta_3 - \Theta_1) - \sin^2(\Theta_2 - \Theta_1) \\ &\neq \left(\sin(\Theta_3 - \Theta_1) + \sin(\Theta_2 - \Theta_1)\right)\left(\sin(\Theta_3 - \Theta_1) - \sin(\Theta_2 - \Theta_1)\right). \end{aligned} \tag{16}$$

"Inequality violation" of Equation (14) is when the left hand side of the equation minus the right hand side becomes negative. This is indeed seen for the quantum-mechanically calculated probabilities at various angles and over extended domains of none-zero measures (see **Figure 1**). For our demonstration, however, all we need is to choose carefully a small set of angles (or even a single set of angles) at which Equation (13) is violated by an amount much larger than a typical experimental value of the order of the error in angular measurement $\delta\theta$, typically ~0.1 deg. For clarity of illustration we choose θ_1 to be identically zero, and $\theta_2 = 36$ deg and $\theta_3 = 72$ deg, since the surface dips appreciably, ~0.1, below the zero plane for this choice. The expected standard deviation in Equation (13), given non zero $\delta\theta_2$ and $\delta\theta_3$, can easily be calculated given $\delta\theta$ to be only ~10^{-4}.

For $\delta\theta \in [0.01, 0.25]$, we calculate the probability (at $\theta_2 = 36$ deg and $\theta_3 = 72$ deg) of no violation for each $\delta\theta$. This is when that difference in the two parts of Equation (14) crosses the zero plane. We assume that both the intervalized difference and the difference that is calculated using error propagation are centered Gaussians. To arrive at the probability of no violation, we simply integrate from the center of the interval to the zero point, after normalizing to unity and subtracting 1/2. Since, for purposes of this demonstration, we do not

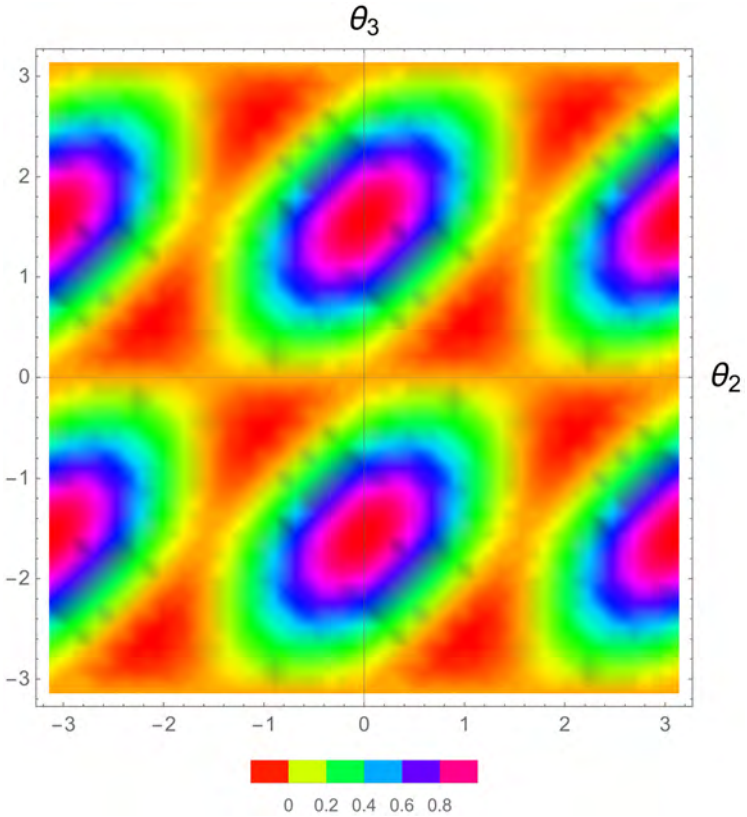

Figure 1. Density plot of Equation (13) evaluated at $\theta_1 = 0$ for $\theta_2, \theta_3 \in [-\pi, \pi]$. The surface is seen to dip below zero for some angles.

ascribe any weighting function to the intervalized angles, the calculated probabilities are more representative of upper limits rather than most likely values.

Figure 2 shows the calculated probability of no violation as a function of the size of the error in the angle measurement, $\delta\theta$. From Figure 2 we see that intervalizing measured polarization angles, *i.e.*, using their $\mathcal{D}$-measures, and using interval arithmetic to calculate probabilities and correlations can lead to re-interpreting violations as non-violations with the probabilities as estimated above. The calculated probabilities of no-violation themselves show a strong, nonlinear geometric relation to the assumed uncertainty in the measured angles. This is due both to the structure of Equation (14) and the size of the error in the measured angles, *i.e.*, not just the presence of the error itself. For this particular photon polarization-angle example, Figure 2 suggests that uncertainties in the measured angles need to be less than 0.05 deg to differentiate clear violation from no violation.

As mentioned above, the calculated no-violation probabilities using interval-based quantities appear to depend on the algebraic structure of the inequality itself. A critical parameter in the interval estimation for the probabilities is the Hausdorff distance, Equation (11). In Figure 3, we show the dependence of this distance on the number of subdivisions needed for the proxy classical correlation interval to enclose the proxy quantal correlation interval. The distance is

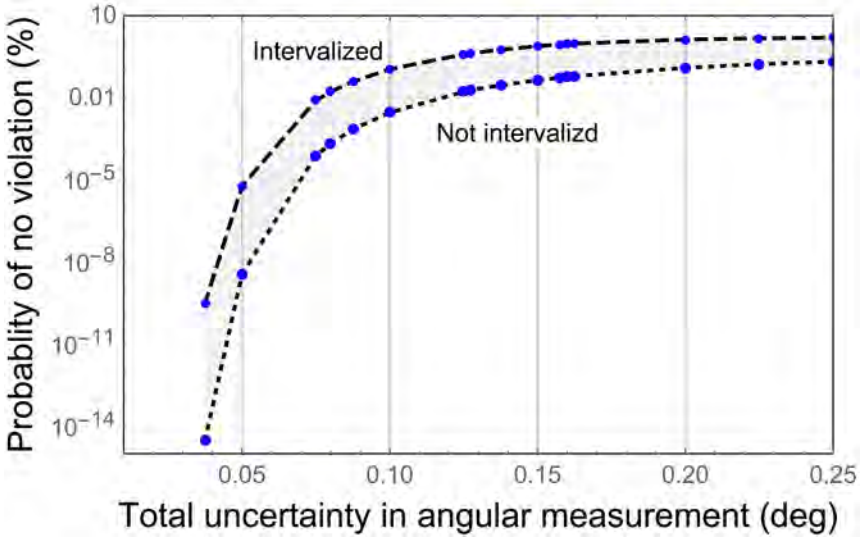

Figure 2. Probability of no violation of Bell's inequality versus the total uncertainty in the measurements of θ_2 and θ_3. The top set of points is from Equation (14), the intervalized inequality, while the bottom set is from the not intervalized inequality, Equation (13).

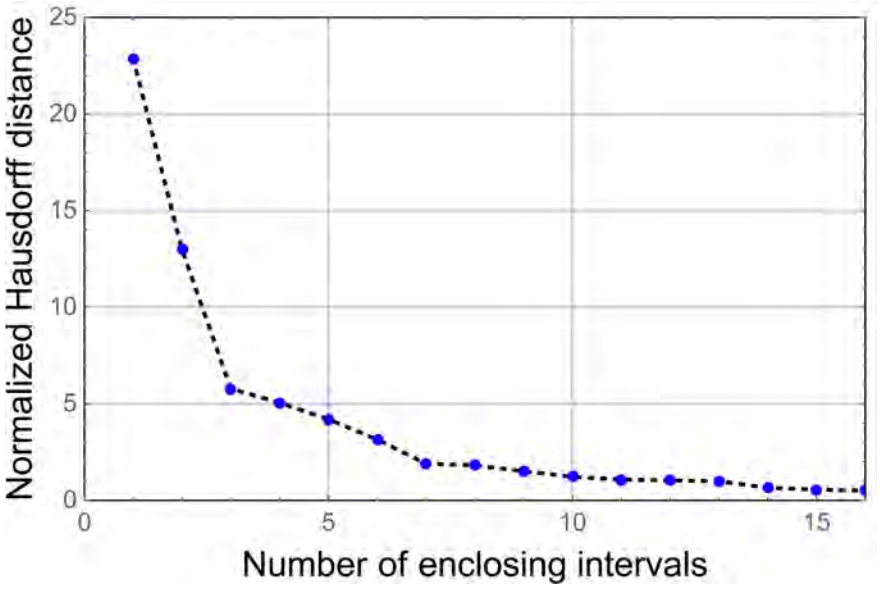

Figure 3. The Hausdorff distance, Equation (11), normalized to the interval diameter as a function of k, *i.e.*, the number of enclosing intervals.

normalized to the diameter of the interval at each k, such that a distance of unity is the smallest possible distance. Here, $k=16$ seems to give a rapid (but not necessarily too rapid) of a convergence, almost in an exponential rather than a geometric fashion. This feature may be important in designing Bell tests optimized for error constraints and the algebraic form or structure of the inequality. Rapid convergence (the "right" form of the inequality) can compensate for the size of the measurement error. In this particular illustration, however, given the exponential convergence, the form of the inequality, Equation (14), seems less of

a consequence to the calculated no-violation probabilities than the size of the measurement error.

3. Discussion

We have introduced and motivated the use of finite intervals to represent physically measurable quantities, we call $\mathcal{D}$-measures, in place of the real-numbered representation, which we consider untenable. We demonstrate the utility of $\mathcal{D}$-measures using theoretical and numerical illustrations. Our theoretical demonstration, an interval-based recasting of Bell's inequality using proxy correlation functionals, shows that, under some conditions, two measured interval quantities—a classically calculated correlation function and its quantal counterpart—can come arbitrarily close to each other. This is in stark contrast to the Bell theorem claim, which assumes classical property values are real-numbered, that no hidden variable theory [21] [22] [23] [24] can produce this arbitrary closeness.

In our numerical demonstration, we apply interval analysis to a measurement of the polarization states of an entangled pair of photons. We calculate the probabilities of no violation and demonstrate that quantal violation of the Bell inequality is likely less severe under the assumption of $\mathcal{D}$-measured values. This means that Bell tests should be considered less compelling as proof of quantum correlations and non-locality [25] [26] [27] [28].

These demonstrations, along with our heuristic arguments, motivate the need for and use of $\mathcal{D}$-measures to more accurately model physical property values than the traditionally assumed real-numbered representation. We assert that the interval-based $\mathcal{D}$-measured representation applies to both classical and quantal physical values, and that their desirability and need for broader application to physical theories in general seems apparent. The development of interval analysis for computing theory and its application to finite-state computing machines was predicated by the need to represent numerical values and quantities that are only approximate by necessity in a real world computing machine. It may be at first counterintuitive to think, for example, any microscopic or macroscopic object can have two or more simultaneous values for any one of its physical properties. Upon analysis, however, it becomes evident that distributed values as provided by $\mathcal{D}$-measures are more tenable than real-numbered values, just like in finite-state machines. Thus we suggest that the application of $\mathcal{D}$-measures and interval analysis should see rapid and pervasive growth in applications to many physical and other theories.

More than 60 years ago, mathematician Tuero Sunaga, working in the field of communication theory at the University of Tokyo wrote [8]: "The interval concept is on the borderline linking pure mathematics with reality and pure analysis with applied analysis." Since that time, however, the application of interval analysis has been almost entirely restricted to the theory of computing machines. It is past time that Sunaga's vision and seminal contributions regarding interval analysis are realized in broader applications as they may have dramatic and far

reaching impacts.

More specifically to NASA, the need for advancements in communication and computing theories and related technologies make broader applications of $\mathcal{D}$-measures to physical systems even more compelling. Our own future work on this effort will include more rigorous interval-based mathematical modeling of Bell-like tests, re-formulation of some well known models of physical systems using interval-based analysis, and a better appreciation of the benefits and limitations of the new analysis when applied to physical theory, with the goal of supporting the advancement of quantum-based analysis, modeling and technologies.

Conflicts of Interest

The authors declare no conflicts of interest regarding the publication of this paper.

References

[1] Gisin, N. (2018) Why Bohmian Mechanics? One- and Two-Time Position Measurements, Bell Inequalities, Philosophy, and Physics. *Entropy*, **20**, 105. https://doi.org/10.3390/e20020105

[2] Schlosshauer, M. (2014) The Quantum-to-Classical Transition and Decoherence. https://arxiv.org/abs/1404.2635v1

[3] Shannon, C.E. (1948) A Mathematical Theory of Communication. *The Bell System Technical Journal*, **27**, 379-423. https://doi.org/10.1002/j.1538-7305.1948.tb01338.x

[4] Bekenstein, J.D. (1981) A Universal Upper Bound on the Entropy to Energy Ratio for Bounded Systems. *Physical Review D*, **23**, 287. https://doi.org/10.1103/PhysRevD.23.287

[5] Sunoj, S.M., Sankara, P.G. and Maya, S.S. (2009) Characterization of Life Distributions Using Conditional Expectations of Doubly (Interval) Truncated Random Variables. *Communications in Statistics—Theory and Methods*, **38**, 1441-1452. https://doi.org/10.1080/03610920802455001

[6] Misagh, F. and Yari, G. (2012) Interval Entropy and Informative Distance. *Entropy*, **14**, 480-490. https://doi.org/10.3390/e14030480

[7] Warmus, M. (1956) Calculus of Approximations. *Bulletin de l'Academie Polonaise de Sciences*, **4**, 253-257.

[8] Sunaga, T. (2009, Original Publication 1958) Theory of an Interval Algebra and Its Application to Numerical Analysis. *Japan Journal of Industrial and Applied Mathematics*, **26**, 125-143.

[9] Moore, R.E. (1966) Interval Analysis. Prentice-Hall, Englewood-Cliffs.

[10] Kulisch, U. (1969) Grundzüge der Intervallrechnung. in Jahrbuch Überblicke Mathematik 2. Bibliographisches Institute, Mannheim.

[11] Markov, S. and Okumura, K. (1999) The Contribution of T. Sunaga to Interval Analysis and Reliable Computing. In: Csendes, T., Ed., *Developments in Reliable Computing*, Springer Science & Business Media, Berlin, 163. https://doi.org/10.1007/978-94-017-1247-7_14

[12] Alefeld, G. and Mayer, G. (2000) Interval Analysis: Theory and Applications. *Journal of Computational and Applied Mathematics*, **121**, 421-464.

https://doi.org/10.1016/S0377-0427(00)00342-3

[13] Moore, R.E., Kearfoot, R.B. and Cloud, M.J. (2009) Introduction to Interval Analysis. Society for Industrial and Applied Mathematics, Philadelphia. https://doi.org/10.1137/1.9780898717716

[14] Markov, S. (2016) On the Algebra of Intervals. *Reliable Computing*, **21**, 80-108.

[15] Koshelva, O. and Kreinovich, V. (2016) Towards an Algebraic Description of Set Arithmetic. Technical Report UTEP-CS-16-90, University of Texas, El Paso.

[16] Kaucher, E. (1980) Interval Analysis in the Extended Interval Space IR. In: Alefeld, G. and Grigorieff, R.D., Eds., *Fundamentals of Numerical Computation* (*Computer-Oriented Numerical Analysis*), Computing Supplementum Vol. 2, Springer, Berlin, 33. https://doi.org/10.1007/978-3-7091-8577-3_3

[17] Bell, J.S. (1964) On the Einstein Podolsky Rosen Paradox. *Physics*, **1**, 195-200. https://doi.org/10.1103/PhysicsPhysiqueFizika.1.195

[18] Piaget, A. and Landowski, M. (2012) Is the Coventional Interval Arithmetic Correct? *Journal of Theoretical and Applied Computer Science*, **6**, 27-44.

[19] Clauser, J., Horne, M., Shimony, A. and Holt, R. (1969) Proposed Experiment to Test Local Hidden-Variable Theories. *Physical Review Letters*, **23**, 880-884. https://doi.org/10.1103/PhysRevLett.23.880

[20] Aspect, A., Grangier, G. and Roger, G. (1982) Experimental Realization of Einstein-Podolsky-Rosen-Bohm Gedankenexperiment: A New Violation of Bell's Inequalities. *Physical Review Letters*, **49**, 91-94. https://doi.org/10.1103/PhysRevLett.49.91

[21] Bell, J.S. (1966) On the Problem of Hidden Variables in Quantum Mechanics. *Reviews of Modern Physics*, **38**, 447-452. https://doi.org/10.1103/RevModPhys.38.447

[22] Bohm, D. (1952) A Suggested Interpretation of the Quantum Theory in Terms of "Hidden Variables" Parts I and II. *Physical Review*, **85**, 166-193. https://doi.org/10.1103/PhysRev.85.180

[23] Mermin, N.D. (1993) Hidden Variables and the Two Theories of John Bell. *Reviews of Modern Physics*, **65**, 803-815. https://doi.org/10.1103/RevModPhys.65.803

[24] Einstein, A., Podolsky, B. and Rosen, N. (1935) Can Quantum Mechanical Description of Physical Reality Be Considered Complete? *Physical Review*, **47**, 77-80. https://doi.org/10.1103/PhysRev.47.777

[25] Mattuck, R.D. (1981) Non-Locality in Bohm-Bub's Hidden Variable Theory of the Einstein-Podolsky-Rosen Paradox. *Physics Letters A*, **81**, 331-332. https://doi.org/10.1016/0375-9601(81)90081-5

[26] de Muynck, W.M. (1986) The Bell Inequalities and Their Irrelevance to the Problem of Locality in Quantum Mechanics. *Physics Letters A*, **114**, 65-67. https://doi.org/10.1016/0375-9601(86)90480-9

[27] Zukowski, M. and Brukner, C. (2014) Quantum Non-Locality. *Journal of Physics A*, **47**, Article ID: 424009. https://doi.org/10.1088/1751-8113/47/42/424009

[28] Aharonov, Y., Botero, A. and Scully, M. (2014) Locality or Non-Locality in Quantum Mechanics: Hidden Variables without "Spooky Action-at-a-Distance". *Zeitschrift für Naturforschung A*, **56**, 5-15. https://doi.org/10.1515/zna-2001-0103

[29] Dehlinger, D. and Mitchell, M.W. (2002) Entangled Photons, Nonlocality, and Bell Inequalities in the Undergraduate Laboratory. *American Journal of Physics*, **70**, 903-910. https://doi.org/10.1119/1.1498860

[30] Maccone, L. (2013) A Simple Proof of Bell's Inequality. *American Journal of Physics*, **81**, 854-859. https://doi.org/10.1119/1.4823600

Appendix: The Structure of a Bell Test

In 1964, Irish physicist John S. Bell proposed a revolutionary theorem that could possibly prove the existence of quantal correlations of entangled objects. His theorem showed that violations of a classical probability inequality could be tested so as to prove classical correlations of detected particles cannot be made arbitrarily close to quantal correlations (see, e.g., [29] [30], and references therein). We illustrate the Bell theorem and tests with an example Bell test structure with these key elements (see **Figure 4**): 1) A source of twin photons, P1 and P2, entangled with the same quantum spin state. 2) A set of two detectors, D1 and D2, one for each of the entangled pair. 3) An adjustable relative angle, θ, between the two detectors, along with relationships for the classical correlation function to the relative detector angle and for the quantal correlation function (**Figure 5**).

If quantal correlations are as predicted by the theory, Bell test data show a cosine squared-relationship of correlation with respect to the relative detector angle (the red curve in **Figure 5**). If classical correlations are correct, on the other hand, the relationship will be linear (the blue curve in **Figure 5**). **Figure 6** and **Figure 7** illustrate the justifications for the linear and the cosine-squared relationships, respectively.

The classical and quantum correlations are most easily illustrated using photons with the same spin, though twin polarization photons are essentially the same. The angle of Detector 1, designated D1, is used as a reference angle of 0-deg. The angle of D2 relative to D1 is θ. For the classical case, the green arc in **Figure 6** shows where these detectors will agree, *i.e.*, be correlated, while the red arc shows where they will disagree. Clearly, as θ increases linearly, the green arc will diminish linearly and the red arc will increase linearly. This shows the relationship of correlation to relative detector angle to be linear for the classical case. Linearity can also be appreciated to stem from the assumed uniform distribution of a random θ.

The quantal case is very different, as illustrated by **Figure 7**. Quantum theory dictates that when D1 detects P1 spin, for example, spin up, the quantum spin state of P2 must assume the same spin angle, *i.e.*, spin up. So P2 must strike D2 with the D1 detected angle of P1. But since D2 is at a relative angle of θ with D1, the P2 quantum spin state must be projected onto D2, *i.e.*, multiplied by the

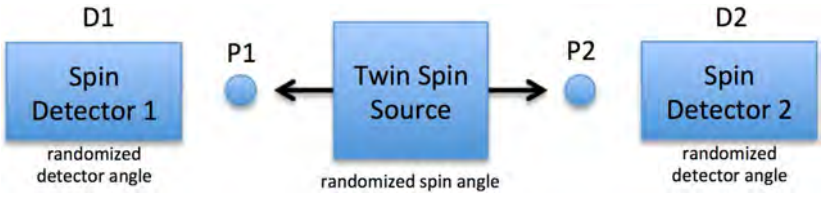

Figure 4. A notional Bell test setup. Key elements are 1) a source of twin photons, P1 and P2, entangled with the same quantum spin state, 2) a set of two detectors, D1 and D2, one for each of the entangled pair, and 3) an adjustable relative angle, θ, between the two detectors.

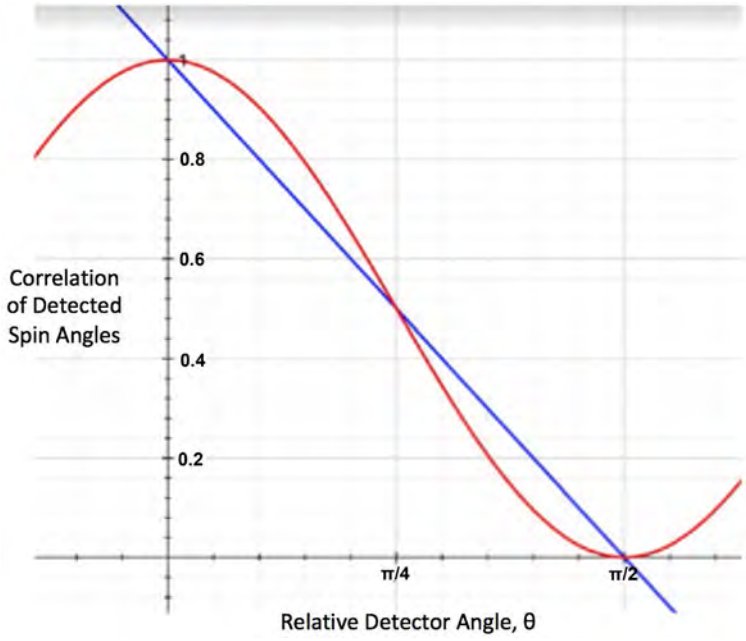

Figure 5. Prototypical classical correlation (in blue) and quantum correlation (in red) as functions of the relative detector angle θ.

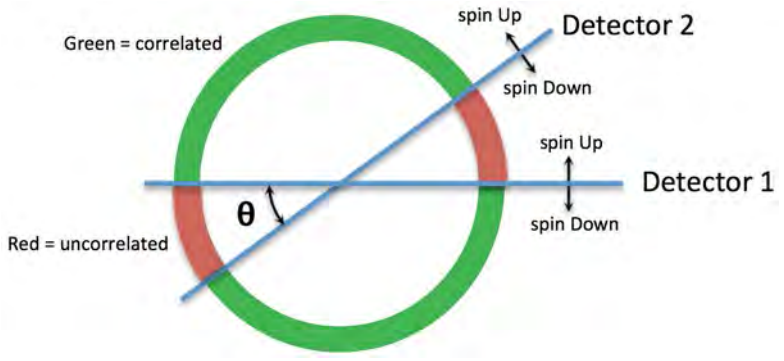

Figure 6. Classical correlation as a linear function of θ; linear increases in θ cause correspondingly linear changes in the green and red arc lengths.

$\cos\theta$. Since quantum probability is the square of the state amplitude, the multiplier becomes $\cos^2\theta$. This means the probability of a D1 detection being the same as a D2 detection, *i.e.*, the probability of agreement, or correlation, is a function of $\cos^2\theta$.

So, if quantum predictions are correct, Bell test data will reproduce the red curve in **Figure 5** for many measurements of random spin and random detector angles. If classical predictions are correct, the blue curve will be reproduced. Many actual Bell tests consistently have reproduced the quantum prediction. However, there is a critical built-in assumption for the classical case and the Bell inequality: that property values, such as spin or polarization, are real-numbered values.

But, as we have argued in this paper, if one replaces real-numbered values with "quasi classical" interval values, or $\mathcal{D}$-measures, the differences between

the two results may not be as pronounced or as differentiated, at least under some conditions (see Figure 8). One obvious result of this finding is that the validity of using conventional Bell tests to demonstrate quantum correlations may be less compelling when using $\mathcal{D}$-measures than a real-number representation.

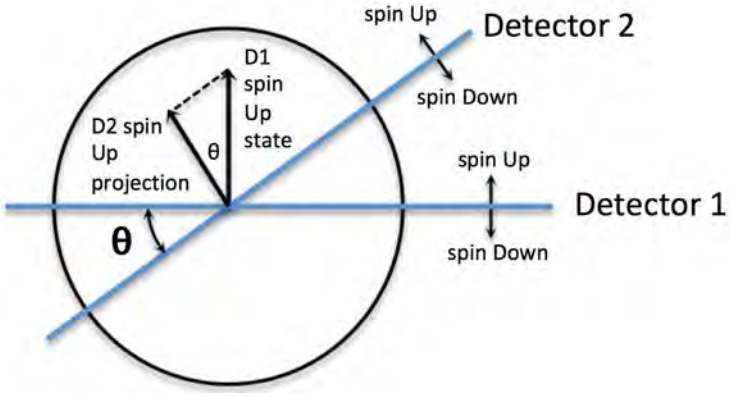

Figure 7. Quantum correlation as a function of $\cos^2\theta$. P2 assumes the direction of the P1 state detected by D1, e.g., spin up. This state is then projected onto the D2 up direction. The projected amplitude is squared so as to get the absolute probability.

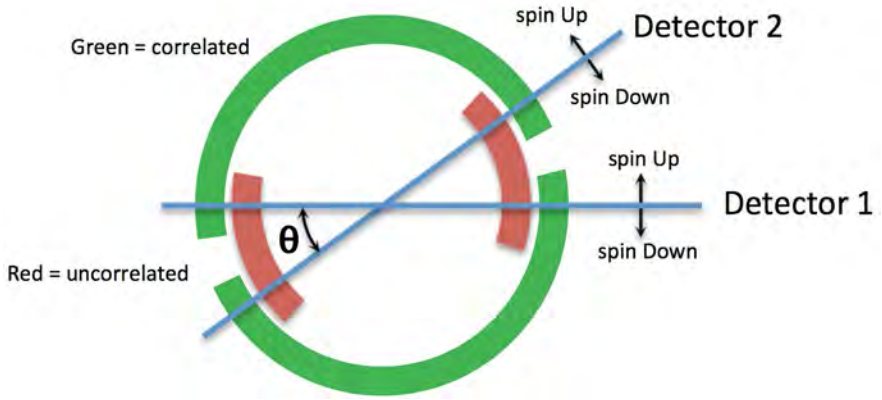

Figure 8. For $\mathcal{D}$-measured (intervalized) spin angles, correlated and uncorrelated regions can overlap.

Scientific Research Publishing

Journal of Modern Physics, 2019, 10, 601-612
http://www.scirp.org/journal/jmp
ISSN Online: 2153-120X
ISSN Print: 2153-1196

How Good Is the Debye Model for Nanocrystals?

Enrique N. Miranda[1,2*], Geraudys Mora-Barzaga[1]

[1]CONICET and Facultad de Ciencias Exactas y Naturales, Universidad Nacional de Cuyo, Mendoza, Argentina
[2]IANIGLA, CONICET, Mendoza, Argentina
Email: *emiranda@mendoza-conicet.gov.ar

How to cite this paper: Miranda, E.N. and Mora-Barzaga, G. (2019) How Good Is the Debye Model for Nanocrystals? *Journal of Modern Physics*, **10**, 601-612.
https://doi.org/10.4236/jmp.2019.106042

Received: March 5, 2019
Accepted: May 6, 2019
Published: May 9, 2019

Abstract

The question here is whether the Debye model is suited to evaluate the specific heat of nanocrystals. For this, the simplest possible nanocrystal is considered: a basic cubic structure made of atoms that interact through a harmonic potential. This simple model can be solved exactly. This allows the dispersion relation of the mechanical waves to be determined, so that calculating the exact specific heat turns out to be quite straightforward. Then, the same problem is solved using the Debye approximation. Our findings show that the specific heat of a nanocrystal evaluated exactly is higher than the value found in the thermodynamic limit, that is to say, the specific heat decreases as the nanocrystal size increases. In addition, it becomes clear that the Debye model is a poor approximation for calculating the specific heat of a nanocrystal. Naturally, the Einstein model yields an even worse result. The cause of the discrepancy is found in the role of the nanocrystal surface.

Keywords

Nanocrystals, Few-Particle Systems, Debye Model, Lattice Vibrations

1. Introduction

The boom of physics at a nanoscopic scale justifies questioning the validity of some of the usual claims when working with systems made up of a few hundred or a few thousand particles. Previous papers [1] [2] dealt with studies on how the thermodynamic properties change when evaluated following the different ensembles of statistical mechanics. These demonstrated that, for systems with very few thousand particles, the different thermodynamic magnitudes reach the same values independently of the ensemble considered. In this sense, a claim of conventional wisdom was confirmed. However, for systems with tens of particles, it was also shown that some fundamental statements ceased to be valid; for example, the specific heat depends on the context in which it is measured [2].

In addition, the question arises whether the usual models for solids are applicable at the nanoscale. A recent article [3] introduced "The Einstein nanocrystal", which is the simplest model for a nanoparticle. The atoms are assumed to be configured in a simple cubic lattice, where each can oscillate in three different directions and with the same frequency in all cases. Such a straightforward model served to reveal the importance of the surface for the specific heat of the nanocrystal. The present article takes the next step and introduces a similar nanocrystal consisting of a simple cubic lattice where the atoms interact through a harmonic potential ("springs"), and there are normal modes with certain distribution of frequencies. The objective here is to test the validity of the approximations made using the very well-known Debye solid [4] [5] to study systems with a few hundred or a few thousand atoms.

The body of this article is structured in three main sections. Section 2 presents the model of a nanocrystal formed by N_A atoms and shows its exact solution. Section 3 introduces the approximations made to obtain the specific heat of the Debye solid and, for comparison purposes, the Einstein model is also included. By comparing both models with the exact results, it will become clear that they are not suited for systems with thousands of atoms. Finally, Section 4 summarizes the conclusions.

2. The Simplest Nanocrystal Model

Figure 1 shows the proposed nanocrystal model. It is a simple cubic structure with a lattice constant of a_0. There are a total of N_A atoms, which means that the side of the nanocrystal has $n_L = N_A^{1/3}$ atoms and the total volume is given by $V = (n_L - 1)^3 a_0^3$. The atoms with mass M are connected to each other through springs characterized by a constant K.

It should be noticed that we deal with a toy model since there are no simple cubic crystals in nature. We use this crystal structure because our concern is to check the validity of the Debye model at the nanoscale and do not pretend to reproduce any actual experimental result.

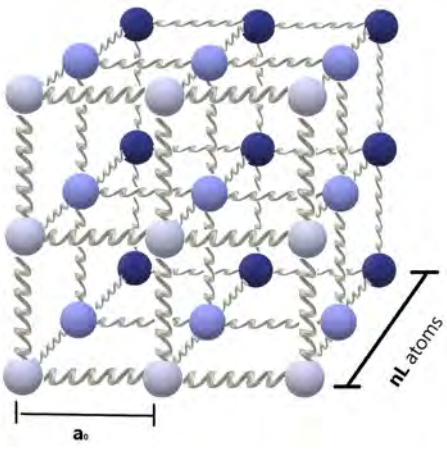

Figure 1. The nanocrystal model studied. A simple cubic structure with n_L atoms per side and a lattice constant of a_0.

In terms of classical mechanics, the behavior of this system is well-known: the system has $3n_L^3$ different oscillation modes whose frequencies can be calculated easily. The case of a one-dimensional lattice with pinned boundary conditions is dealt with in textbooks [5]. Each oscillation mode is characterized by a wave vector $\boldsymbol{k}$, whose module is $k = m\pi/(n_L a_0)$, where $m = 0,1,2,\cdots,n_L - 1$ and the frequency ω is given by:

$$\omega^2(\boldsymbol{k}) = \left(\frac{4K}{M}\right)\sin^2\left(\frac{ka_0}{2}\right) \tag{1}$$

Generalizing to the three-dimensional case [6] leads to the following relation between the wave vector $\boldsymbol{k}$ and the frequency ω:

$$\boldsymbol{k} = \frac{\pi}{n_L a_0}\left(m_x, m_y, m_z\right) \tag{2}$$

$$\omega^2 = \frac{4K}{M}\left(\sin^2\left[\frac{\pi}{2n_L}m_x\right] + \sin^2\left[\frac{\pi}{2n_L}m_y\right] + \sin^2\left[\frac{\pi}{2n_L}m_z\right]\right) \tag{3}$$

where $m_x, m_y, m_z = 0,1,2,\cdots,n_L - 1$. The characteristic frequency of the system is:

$$\omega_0 = 2\sqrt{K/M}\ . \tag{4}$$

It is necessary to consider all possible combinations of m_x, m_y and m_z, except (0, 0, 0) that obviously corresponds to the body at rest.

So far for the classical treatment, in quantum terms, these results are interpreted as the system having phonons that are characterized by a wave vector $\boldsymbol{k}$ and a frequency $\omega(\boldsymbol{k})$, and that obey Bose-Einstein's statistics. It is a usual exercise in any statistical mechanics course [5] to show that the energy of such a system is given by:

$$U = \sum_{\boldsymbol{k}}\left(\frac{1}{2}\hbar\omega(\boldsymbol{k}) + \frac{\hbar\omega(\boldsymbol{k})}{e^{\frac{\hbar\omega(\boldsymbol{k})}{k_B T}} - 1}\right) \tag{5}$$

It follows immediately that the heat capacity $C = \mathrm{d}U/\mathrm{d}T$ is:

$$C = \sum_{\boldsymbol{k}}\left(\frac{\hbar^2\omega^2(\boldsymbol{k})e^{\frac{\hbar\omega(\boldsymbol{k})}{k_B T}}}{k_B T^2\left(e^{\frac{\hbar\omega(\boldsymbol{k})}{k_B T}} - 1\right)^2}\right) \tag{6}$$

The sum of all the $\boldsymbol{k}$ vectors can be broken down into a triple sum: $\sum_{\boldsymbol{k}}(\,) \to \sum_{k_x}\sum_{k_y}\sum_{k_z}(\,)$, and one should remember that there are three possible polarization states (two transverse and one longitudinal) of each phonon.

Also, some abbreviations are included to simplify the notation. We make use of an auxiliary function defined as follows:

$$R\left(m_x, m_y, m_z\right) = \left(\sin^2\left[\frac{\pi}{2n_L}m_x\right] + \sin^2\left[\frac{\pi}{2n_L}m_y\right] + \sin^2\left[\frac{\pi}{2n_L}m_z\right]\right)^{1/2} \tag{7}$$

The characteristic frequency of the system is $\omega_0 = 2(K/M)^{1/2}$. The temperature can be expressed in terms of a dimensionless variable t as $T = tT_c$ with $T_c = \hbar\omega_0/k_B$. Keeping in mind all these definitions and remembering that there are n_L^3 atoms, the specific heat per atom c is written:

$$c_{ex} = \frac{3k_B}{n_L^3}\sum_{m_x=0}^{n_L-1}\sum_{m_y=0}^{n_L-1}\sum_{m_z=0}^{n_L-1}\frac{R^2(m_x,m_y,m_z)e^{R/t}}{t^2\left(e^{R/t}-1\right)^2};\ m_x+m_y+m_z\neq 0 \quad (8)$$

In the rest of this article, the specific heat is expressed in terms of units of k_B. In this way, c becomes an adimensional variable as well as the temperature t.

This is expression (8) is exact, noted by subscript "*ex*", and it gives the specific heat per atom for a nanocrystal with a simple cubic structure and n_L atoms per side. The first question that arises is how this parameter changes according to the size of the system. And the answer is that it changes very slowly, as seen in Figure 2.

In the next section, the specific heat will be calculated again but introducing step-by-step the approximations of the Debye model.

3. The Debye Approximation

Actually, several approximations are made in the Debye model for solids [4] [5]. First, the relation between the frequency and the wave vector is linearized. Then, a frequency continuum is assumed and a maximum cutoff frequency is introduced.

Linearizing the dispersion relation of the phonons implies approximating the sine that appears in (1) by its argument. In one dimension:

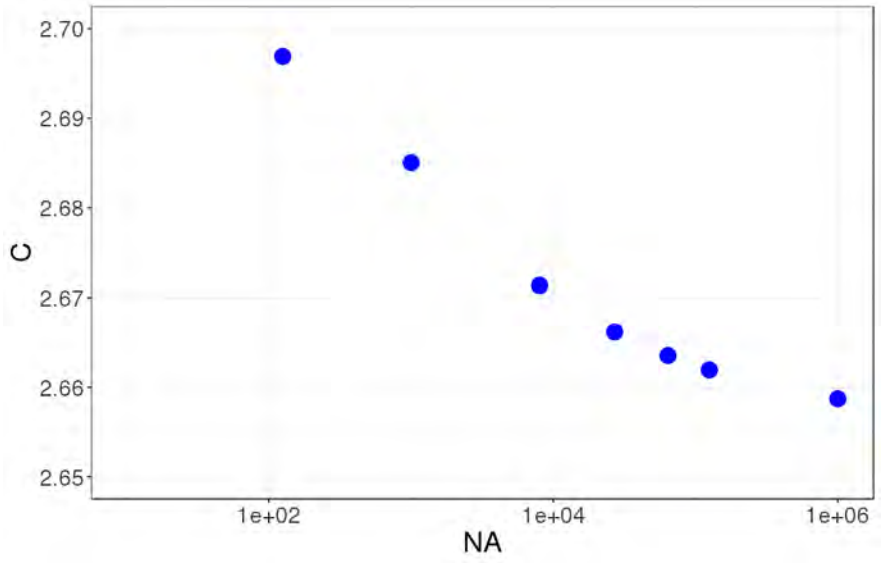

Figure 2. Specific heat per atom c evaluated exactly for $t = 1$ in relation to the number of atoms N_A. It is clear that the specific heat for a small nanocrystal is higher than the value in the thermodynamic limit and that it converges slowly towards that value. The specific heat is in units of k_B.

$$\omega(k) = 2\left(\frac{K}{m}\right)^{1/2}\left|\sin\left(\frac{ka_0}{2}\right)\right| \cong \omega_0 \frac{ka_0}{2} = \omega_0 \frac{\pi m}{2n_L} \tag{9}$$

with $m = 0,1,2,\cdots,n_L - 1$.

In three dimensions, the auxiliary function $R(m_x, m_y, m_z)$ defined previously needs to be modified as follows:

$$R'(m_x, m_y, m_z) = \left(\left(\frac{\pi}{2n_L}m_x\right)^2 + \left(\frac{\pi}{2n_L}m_y\right)^2 + \left(\frac{\pi}{2n_L}m_z\right)^2\right)^{\frac{1}{2}} \tag{10}$$

To calculate the specific heat, the same expression (8) is used, but with function R' given by (10).

Then, the frequencies are assumed to be continuous and the sum in (6) is replaced by an integral that includes the density of states for phonons. And finally, a maximum frequency, known as the Debye frequency, is introduced. Physically, the existence of a maximum frequency is determined by the existence of a minimum wavelength associated with the interatomic distances. In the case of a finite sample, there will also be a minimum frequency because there is a maximum wavelength associated with the linear size of the sample.

The minimum frequency $\omega_{\min}$ is obtained taking the wavelength along the edge of the cube as maximum half-wavelength:

$$\frac{\lambda_{\max}}{2} = (n_L - 1)a_0 = V^{1/3} \tag{11a}$$

$$\omega_{\min} = \frac{\pi c}{V^{1/3}} \tag{11b}$$

where c is the speed of sound in the lattice, given by [5]: $c = a_0(K/M)^{1/2}$. The same speed is presumed for the transverse and longitudinal waves. It should be remarked that this is a strong assumption of our toy model made in order to keep the calculations as simple as possible.

To establish the maximum frequency, or Debye frequency ω_D, the procedure is similar to the usual treatment: the integral for the density of states between $\omega_{\min}$ and ω_D has to be equal to the number of degrees of freedom for the system. Here, attention should be paid to the atoms in the surface that, consequently, have fewer degrees of freedom than those inside the cube. A careful count [3] shows that the number of oscillators (the "springs" portrayed in **Figure 1**) is: $3\left(n_L^3 - n_L^2\right) = 3\left(N_A - N_A^{2/3}\right)$. Finally, having in mind the expression for the density of states $D(\omega)$ for phonons [5], we can write:

$$\int_{\omega_{\min}}^{\omega_D} D(\omega)\mathrm{d}\omega = \int_{\omega_{\min}}^{\omega_D} \frac{3V}{2\pi^2 c^3}\omega^2 \mathrm{d}\omega = 3\left(N_A - N_A^{2/3}\right) \tag{12}$$

This gives:

$$\omega_D^3 = \frac{6c^3 N_A \pi^2}{V} + \frac{c^3\pi^3}{V} - \frac{6c^3 N_A^{2/3}\pi^2}{V} \tag{13}$$

It is interesting to analyze each term in the previous expression. The first term is the one usually present in the treatment of the Debye solid. The second is as-

sociated with the existence of a minimum frequency due to the size of the sample. And the third accounts for the existence of a surface. It becomes clear that the effect caused by the finite size of the sample is negligible in the presence of the other two terms that explicitly depend on N_A. Now, the problem is reduced to calculating the specific heat of this nanoparticle keeping in mind the linearized dispersion relation and the existence of a minimum and a maximum frequency.

Taking into account the density of states for phonons $D(\omega)$ and expression (6), the heat capacity in the Debye approximation is:

$$C_{\text{Debye}} = \frac{9N_A\hbar^2}{\omega_D^3 k_B T^2}\int_{\omega_{\min}}^{\omega_D} \frac{\omega^4 e^{\frac{\hbar\omega}{k_B T}}}{\left(e^{\frac{\hbar\omega}{k_B T}}-1\right)^2} d\omega \tag{14}$$

To enable comparisons with the previous results, it is convenient to rewrite the previous expression in terms of the dimensionless temperature t defined earlier, and to divide by the number of atoms. The specific heat per atom c_{Debye} in the Debye approximation is obtained as follows:

$$c_{\text{Debye}} = \frac{9k_B}{u_D^3 t^2}\int_{u_{\min}}^{u_D} \frac{u^4 e^{u/t}}{\left(e^{u/t}+1\right)^2} du \tag{15}$$

The integration limits are $u_{\min} = \omega_{\min}/\omega_0$ y $u_D = \omega_D/\omega_0$. It is useful to write these magnitudes in terms of our model parameters, as seen in **Figure 1**. Thus, we find that:

$$u_D = \left(\frac{3n_L^3\pi^2}{4(n_L-1)} - \frac{3n_L^2\pi^2}{4(n_L-1)} + \frac{\pi^3}{8(n_L-1)}\right)^{1/3} \tag{16a}$$

and:

$$u_{\min} = \frac{\pi}{2(n_L-1)} \tag{16b}$$

It is clear that expression (15) depends only on the number of atoms n_L and the reduced temperature t.

In **Figure 3**, the specific heat obtained with the Debye approximation is compared with that obtained exactly for a cubic nanocrystal.

The most readily visible conclusion is that the Debye approximation is unsuited for systems with tens of particles **Figure 3(a)**, as well as for systems with a few thousand atoms **Figure 3(b)** or even for a million atoms **Figure 3(c)**.

It is useful to compare the exact specific heat of a nanocrystal with the usual value of the Debye solid in the thermodynamic limit [4] [5] because, as it is known, the Debye model is a reasonable approximation for the bulk specific heat. The result is plotted in **Figure 4**. It is clear that, the specific heat of a nanocrystal is higher than the bulk value, as observed in most experiments [7] [8] [9] [10]. That is to say, our simple model explains a characteristic observed repeatedly in nanocrystals and nanoclusters.

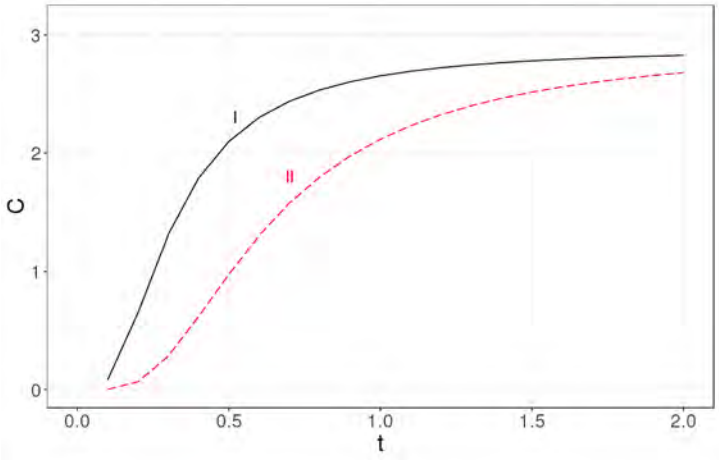

(a)

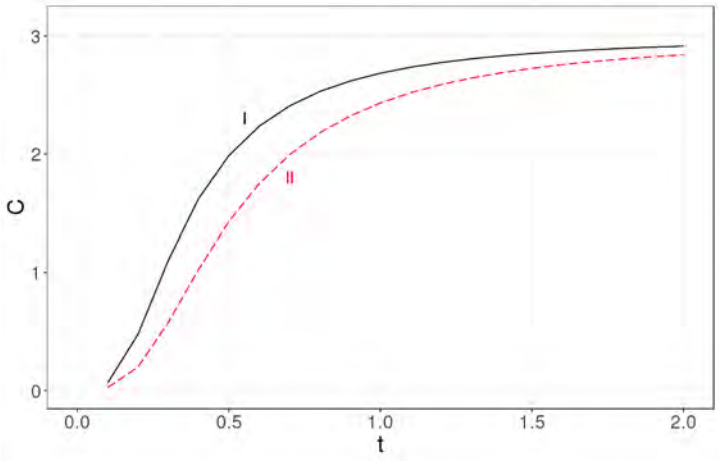

(b)

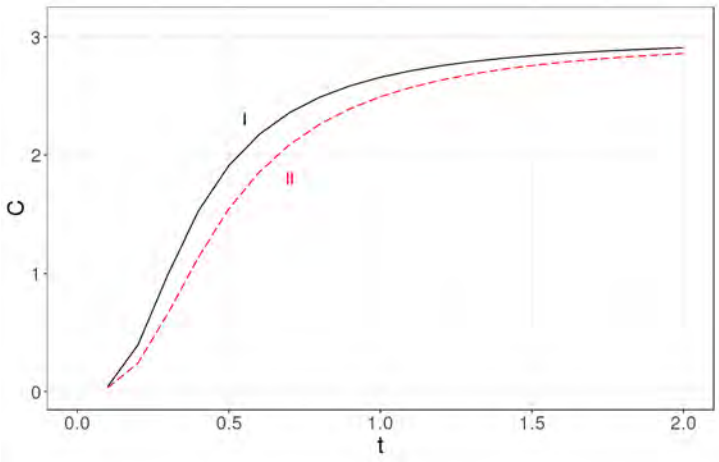

(c)

Figure 3. The specific heat calculated exactly (solid line labeled as I) is compared with the specific heat obtained using the Debye approximation (dashed line labeled as II) for three nanocrystal sizes: (a) 3^3, (b) 10^3 and (c) 100^3. It becomes clear that the Debye approximation is unsuited for a system with tens of atoms. Neither is it a good approximation for a nanocrystal with 10^3 or 10^6 atoms. The specific heat is in units of k_B and the temperature is a dimensionless variable as explained in the text.

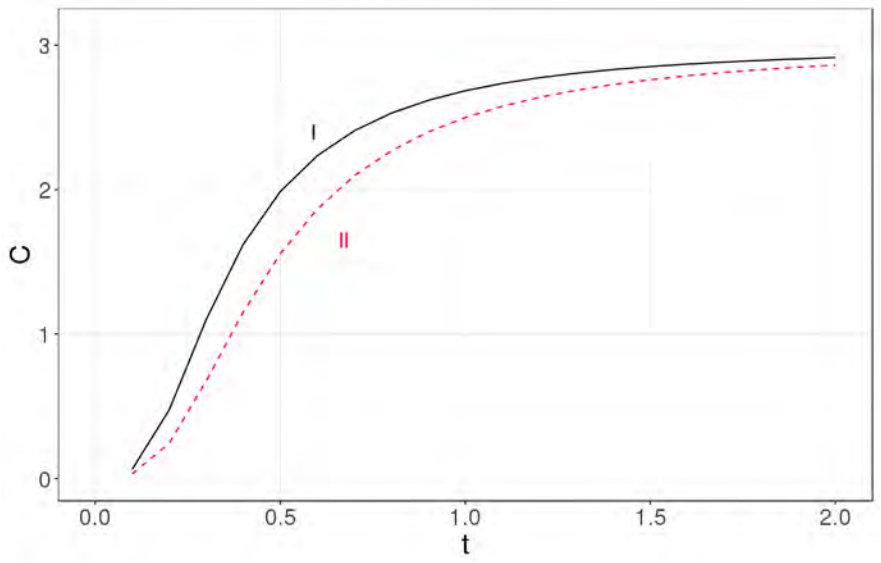

Figure 4. The specific heat calculated exactly (solid line labeled as I) for a nanocrystal with 10^3 atoms is compared with the usual value predicted by the Debye model (dashed line labeled as II) in the thermodynamic limit. Clearly, our model predicts that the specific heat of a nanocrystal is higher than the bulk value, as seen in most experiments.

And how do these results compare with the Einstein solid? In this case, all the phonons have the same frequency ω_0 or, more precisely, the density of states is delta function center in that frequency: $D(\omega)=\delta(\omega-\omega_0)$. Therefore, expression (6) is reduced to [3]:

$$C_{\text{Einstein}}=3\left(N_A-N_A^{2/3}\right)\frac{\hbar^2\omega_0^2 e^{\frac{\hbar\omega_0}{k_BT}}}{k_BT^2\left(e^{\frac{\hbar\omega_0}{k_BT}}-1\right)^2} \tag{17}$$

Naturally, it is convenient to divide by the total number of atoms $N_A=n_L^3$ and to introduce the dimensionless temperature *t*. It is necessary to keep in mind that the characteristic frequency was defined as $(K/M)^{1/2}$ in [3], but in this article it has been defined as twice that value—see Equation (4). As a result, when expressing Equation (17) in terms of the dimensionless temperature, an additional factor 2 appears. Thus, the specific heat per atom in the Einstein approximation is expressed in k_B units as:

$$c_{\text{Einstein}}=3\left(1-\frac{1}{n_L}\right)\frac{4e^{2/t}}{t^2\left(e^{2/t}-1\right)^2} \tag{18}$$

Figure 5 shows c_{ex}, in the Debye approximation c_{Debye} and in the Einstein approximation c_{Einstein}.

Figure 5 is very revealing: the usual models for solids *are not applicable to nanocrystals with hundreds or thousands of atoms.*

It is reasonable to wonder why the Debye approximation is unsuited for systems with hundreds or thousands of atoms. A first conjecture is related to the finite

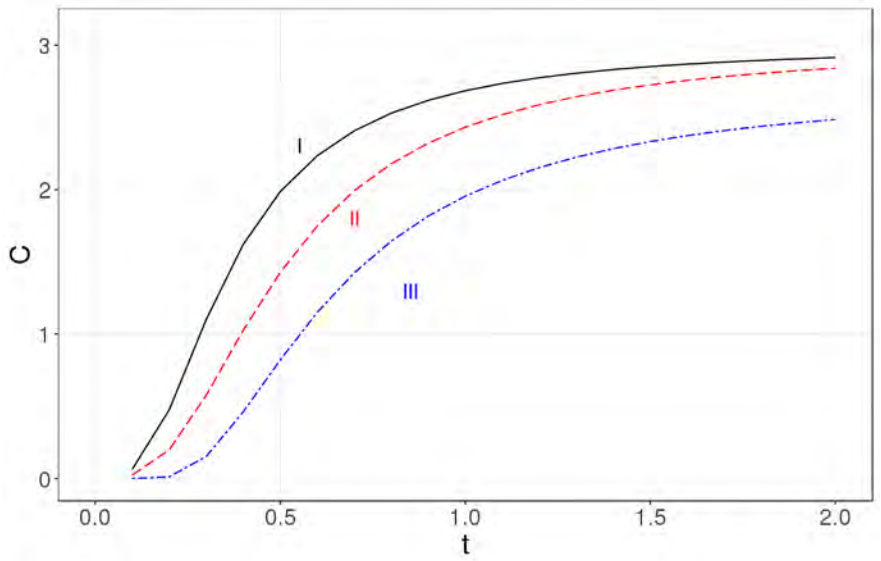

Figure 5. The specific heat for a cubic lattice with 10^3 atoms is evaluated exactly (solid line labeled as I), using the Debye approximation (dashed line labeled as II) and using the Einstein model (dot-dashed line labeled as III).

size of the sample, which is reflected in the existence of a lower limit different from zero in the integral; however, this is not the case. The existence of a lower limit in the frequency has a negligible contribution. For example, when in the integral in (15) the lower limit is replaced by 0, the specific heat changes from 1.4325 to 1.4324 for $n_L = 10$ and $t = 1$. So, clearly, the existence of a lower integration limit different from zero is not relevant.

Another possible cause is the linearization of the dispersion relation. **Figure 6** shows the specific heat evaluated using the correct dispersion relation incorporated to expression (8), and using the linearized version as it appears in expression (10). Clearly the linearization is partially responsible for the discrepancy but other causes should be also considered.

The cause of the discrepancy seems to be twofold. On the one hand, the assumption of a continuous frequency distribution for the phonons is appropriate in the thermodynamic limit, but it is a very strong hypothesis when the number of phonons is in the order of n_L^3. And on the other hand, the existence of a surface seems to have a crucial effect, as already demonstrated in the case of the Einstein nanocrystal [3]. In this paper we have worked with pinned boundary conditions and this implies that surface phonons are neglected. The main difference between a macroscopic piece of material and a nanocrystal is the appearance of surface vibrational modes and a simple, straightforward application of the Debye model does not take into account such modes.

Finally, it should be noted that this model predicts that, for nanocrystals, the specific heat goes exponentially to zero, as inferred from expression (8). And this behavior is different from that observed in macroscopic crystals. There are no experimental data of the nanocrystal specific heat behavior for very low temperatures to confirm or rebut this prediction.

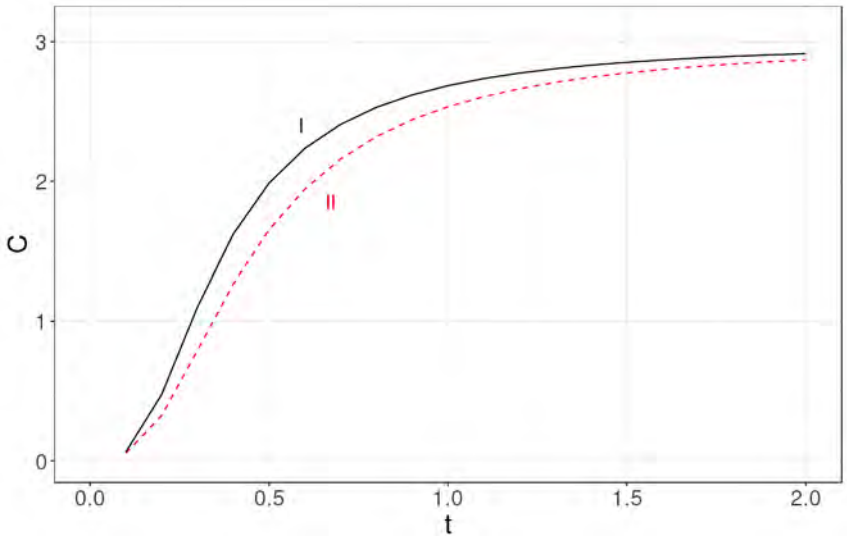

Figure 6. The specific heat of a nanocrystal of 10^3 atoms evaluated using expression (8) that includes the exact dispersion relation (solid line label as I) and using the linear dispersion relation (dashed line labeled as II). The linearization of the dispersion relation seems to be partially responsible of the discrepancy between the exact value and the Debye approximation for the specific heat.

4. Conclusions

In this article, we have explored the validity of the Debye model at the nanoscale. For this, we have considered a very straightforward nanocrystal model: a simple cubic structure whose atoms are assumed to interact through a harmonic potential, as portrayed in Figure 1. This system is simple enough to allow for an exact solution, which gives the dispersion relation for the mechanical waves of the lattice—Equation (3). Thus, by thinking of the system on quantum terms, the exact dispersion relation of the phonons becomes known, and the exact specific heat can be calculated—Equation (8). The form of this specific heat coincides with that expected for a group of oscillators, though its value is higher than that found in the thermodynamic limit. Figure 2 shows the specific heat evaluated at a fixed temperature in relation to the number of atoms in the nanocrystal; it is clear how, as the size increases, the specific heat decreases. This means that our model predicts that the specific heat is higher for nanocrystals than for crystals of macroscopic size, which is what is observed experimentally.

Once the exact specific heat is calculated for our nanocrystal, we apply the Debye approximation to allow for comparisons. To do this, the usual steps are followed, but keeping in mind that the nanocrystal has a finite size and, therefore, there is a maximum wavelength, or rather a minimum frequency. So we obtain an analytical expression for the Debye frequency—Equation (13)—where three terms are easily identified: the usual term and the corrections on account of the finite size and the surface. The first correction has proven to be irrelevant, but not the second. This agrees with our findings for the Einstein model in a previous paper [3]. The result of the current article is summarized in Figure 5, which shows the specific heat calculated exactly, as well as after Debye and after

Einstein. The plot makes it clear that the usual models approximate poorly the exact specific heat. Even for a nanocrystal with 10^6 atoms, the exact value and that obtained with the Debye approximation differ considerably. The surface vibrational modes might be responsible for this disagreement. The message is then: do not forget the surface when dealing with nanocrystals. A naïve application of bulk results to a nanoparticle would lead to wrong conclusions for two reasons: 1) the surface introduces a non negligible effect (the surface phonons in the case of specific heat); 2) as the size of the particle is decreased, the approximation of using a smoothed density of states becomes less and less accurate.

The final conclusion of this article is that the standard Debye model is not very suited to model the specific heat of nanocrystals. But we also think there is a path for doing this better. Although nanocrystals with a simple cubic structure do not exist in nature, the steps outlined here could be replicated for a realistic crystal structure. It would simply be a matter of finding the frequencies of the normal modes for that realistic structure assuming that the atoms interact through a harmonic potential ("springs"). And once the formula linking the wave vector with the frequency is known, evaluating the exact specific heat becomes an exercise of statistical mechanics.

Conflicts of Interest

The authors declare no conflicts of interest regarding the publication of this paper.

References

[1] Miranda, E.N. and Bertoldi, D.S. (2013) Thermostatistic of Small Systems: Exact Results in the Microcanonical Formalism. *European Journal of Physics*, **34**, 1075-1087. https://doi.org/10.1088/0143-0807/34/4/1075

[2] Miranda, E.N. (2017) Statistical Mechanics of Few-Particle Systems: Exact Results for Two Useful Models. *European Journal of Physics*, **38**, Article ID: 065101. https://doi.org/10.1088/1361-6404/aa82fa

[3] Bertoldi, D.S., Fernandez Guillermet, A. and Miranda, E.N. (2016) The Einstein Nanocrystal. *Revista Mexicana de Fisicad E*, **62**, 60-65.

[4] Kittel, Ch. (2004) Introduction to Solid State Physics. Wiley, New York.

[5] Swendsen, R.H. (2012) An Introduction to Statistical Mechanics and Thermodynamics. Oxford University Press, Oxford. https://doi.org/10.1093/acprof:oso/9780199646944.001.0001

[6] Kothari, L.S. and Singal, C.M. (1968) Lattice Dynamics of Microcrystallites. *Physical Review*, **168**, 952. https://doi.org/10.1103/PhysRev.168.952

[7] Rupp, J. and Birringer, R. (1987) Enhanced Specific Heat Capacity Measurements (150-300 K) of Nanometer-Sized Crystalline Materials. *Physical Review B*, **36**, 7888-7890. https://doi.org/10.1103/PhysRevB.36.7888

[8] Hellstern, E., Fecht, H.J., Fu, Z. and Johnson, W.L. (1989) Structural and Thermodynamic Properties of Heavily Mechanically Deformed Ru and AlRu. *Journal of Applied Physics*, **65**, 305-310. https://doi.org/10.1063/1.342541

[9] Zhu, Y.F., Lian, J.S. and Jiang, Q. (2009) Modeling of the Melting Point, Debye

Temperature, Thermal Expansion Coefficient, and the Specific Heat of Nanostructured Materials. *The Journal of Physical Chemistry C*, **113**, 16896-16900. https://doi.org/10.1021/jp902097f

[10] Yu, X. and Zhan, Z. (2014) The Effects of the Size of Nanocrystalline Materials on Their Thermodynamic and Mechanical Properties. *Nanoscale Research Letters*, **9**, 516. https://doi.org/10.1186/1556-276X-9-516

Journal of Modern Physics, 2019, 10, 613-623
http://www.scirp.org/journal/jmp
ISSN Online: 2153-120X
ISSN Print: 2153-1196

Dielectric and Ferroelectric Properties of PZN-4.5PT Nanoparticles Thin Films on Nanostructured Silicon Substrate for Ferrophotovoltaic and Energy Storage Application

Rémi Ndioukane[1], Moussa Touré[1], Diouma Kobor[1], Laurence Motte[2], Jeanne Solard[3], Laurent Lebrun[4]

[1]Laboratoire de Chimie et de Physique des Matériaux (LCPM), University Assane Seck of Ziguinchor, Ziguinchor, Sénégal
[2]Laboratory for Vascular Translational Science (LVTS), University Paris 13, Paris, France
[3]Centrale de Proximité en Nanotechnologies de Paris Nord, Paris, France
[4]Laboratoire Génie Electrique et Ferroélectricité, Institut National des Sciences Appliquées de Lyon, Villeurbanne, France
Email: r.ndioukane1532@zig.univ.sn

How to cite this paper: Ndioukane, R., Touré, M., Kobor, D., Motte, L., Solard, J. and Lebrun, L. (2019) Dielectric and Ferroelectric Properties of PZN-4.5PT Nanoparticles Thin Films on Nanostructured Silicon Substrate for Ferrophotovoltaic and Energy Storage Application. *Journal of Modern Physics*, **10**, 613-623.
https://doi.org/10.4236/jmp.2019.106043

Received: November 10, 2018
Accepted: May 13, 2019
Published: May 16, 2019

Abstract

The integration of ferroelectric materials as thin films has attracted considerable attention these last years thanks to their outstanding performances that allow considering new features for the realization of photovoltaic devices. Our study focuses on investigating structural, dielectric and ferroelectric properties of undoped and Mn doped PZN-4.5PT nanoparticles thin films on Silicon substrate. We fabricate very stable PZN-4.5PT nanoparticles thin films deposited on nanostructured silicon substrate with giant relative dielectric permittivity of 2.76×10^4 and 17.7×10^4 for respectively the undoped and Mn doped thin films. These values are very large compared to those found in single crystals and might be explained by the influence of the gel in which nanoparticles were dispersed. The SEM images show the crystallization of new hexagonal phases on the film surface probably coming from interaction between Si and the gel. The hysteresis loops permitted to determine the spontaneous polarization (P_s), remnant polarization (P_r) and coercive field E_c which are equal to 11.73 μC/cm^2, 10.20 μC/cm^2 and 20 V/cm, respectively for the undoped nanoparticles thin film and 22.22 μC/cm^2, 19.32 μC/cm^2 and 20 V/cm respectively for the Mn doped one. These values are high and correspond to the best ones found in literature compared to typical ferroelectric thin films.

Keywords

PZN-PT, Thin Film, Ferroelectric, Perovskite, Nanoparticles, Gel

1. Introduction

For semiconductor photovoltaic materials, photons with energy higher than the band gap are absorbed to produce electron-hole pairs which are separated by the internalfield in the p-n junction and collected by the electrodes. Consequently, the photo-induced voltage is limited by the energy barrier height at the interface region and usually smaller than the semiconductor band-gap [1]. Therefore, the ferroelectric photovoltaic effect has been attracted a great deal of attention due to its efficient polarization-governed mechanism of charge separation and ability to generate (open circuit voltage) above band-gap voltages [2].

Recently, the discovery of perovskite ferroelectric nanomaterials opened up a great possibility of application for ferroelectric devices. There have been various nanostructures such as nanoparticles, nanorods, and nano-patterned structures using PZT, $BaTiO_3$, and $SrTiO_3$ [3] [4] [5]. Those ferroelectric nanomaterials exhibit very different characteristics in its domain dynamics, coercive field and spontaneous polarization response [6] [7] [8] [9]. Ferroelectric lead compounds having a perovskite structure, such as $Pb(Zn_{1/3}Nb_{2/3})O_3$ (PZN) [10], $Pb(Mg_{1/3}Nb_{2/3})O_3$ (PMN) [11], and their solid solutions with $PbTiO_3$ (PT), have been investigated for high performance ultrasonic transducer applications [12] [13] [14] [15] [16]. These solid solutions have excellent piezoelectric and ferroelectric properties in single crystal form compared to the above ferroelectrics. In addition, its high relative dielectric permittivity value could permit to gain a very high open circuit voltage in photovoltaic cells thanks to the charge accumulation process. Then PZN-PT could be one of the promising new materials for such ferrophotovoltaic devices. Indeed, these last years, high levels of papers have been published about PMN-PT and PZN-PT single crystals [17] [18] [19] [20], showing at least ferroelectric, ferroelastic and piezoelectric properties 10 times higher than those of PZT. However, there is no publication on PZN-PT as thin films for ferrophotovoltaic effect. We know that the greatest difficulty to use such single crystals on electronic devices is to achieve them in thin layers form because of their incongruent melting property. If we fabricate the nanoparticles thin film of such materials without losing ferroelectricity or photovoltaic properties, we can expand the ferroelectric device to various substrates, structures, and nano-scale applications.

In this paper, to integrate them into silicon nanostructures, we realized PZN-4.5PT nanoparticles deposition, already synthesized by the so-called solution flux method [19], as thin film on p-type <100> oriented nanoporous silicon substrate. Surface morphology, dielectric and ferroelectric properties of as deposited thin films were investigated.

2. Experimental Procedure

2.1. PZN-PT Nanoparticles Thin Film Fabrication and Surface Characterization

Undoped and 1% Mn doped PZN-4.5PT grounded powders were dispersed in gel fabricated in the laboratory LCPM in Assane Seck University of Ziguinchor. To obtain a homogeneous film, spinning process was carried out at room temperature using a spin coater Midas 1200 D at 3500 rpm with an initial acceleration time of 5 seconds and an operating time of 10 min. After 10 min bake in oven at 100˚C, thermal annealing in a K114 type muffle furnace was performed. The heating rate of the furnace is chosen between 10 and 20˚C/min. A 30 - 60 min plateau was carried out at 900˚C for the gel diffusion through the p-type silicon (<100> oriented Boron doped monocrystalline silicon with resistivity 5 - 10 Ω.cm and thickness of 600 - 650 μm) nanowires substrate. Cooling at ambient temperature was done naturally. Different samples were fabricated using the two nanopowders and were characterized. Surface morphology of thin films samples were observed using an electron beam lithography system Pioneer Raith model in C(PN)2 (Paris 13 University).

2.2. Dielectric and Ferroelectric Characterization

For dielectric properties characterization, the sample with the deposit thin film was metallized on the both sides with silver paste using the screen-printing method. In order to have good adhesion between the silver and the thin layer, the metallized sample was annealed at 450˚C for 30 min in a thermo scientific model FB1310M-33 oven. For dielectric losses measurements and to calculate the relative dielectric constant (ε_r), the capacity measurements as function of the temperature and the frequency were performed using a LCR meter model LCR-819 from GWINSTEK. The relative dielectric constant was determined using the following formula

$$\varepsilon_r = \frac{Ce}{S\varepsilon_0} \tag{1}$$

where C is the measured capacity, e the thickness, S the metallized surface and ε_0 the vacuum permittivity ($8.85.10^{-12}$ F/m). A modified Sawyer-Tower circuit at room temperature was used to measure the polarization versus the DC field. From polarization-E_{field} curves, E_c, P_r and P_s were determined.

3. Results and Discussion

3.1. Surface Characterization

Figure 1 shows the SEM images of the different thin layers revealing that the nanoparticles gel is diffused inside the nanowires and covered totally the whole surface. The images of Figure 1(a)-(c) (increasing magnetization) show the complex nature of the undoped nanoparticles thin films randomly distributed. One can find the presence of black zones (Pb is highly reactive with Si at 600˚C

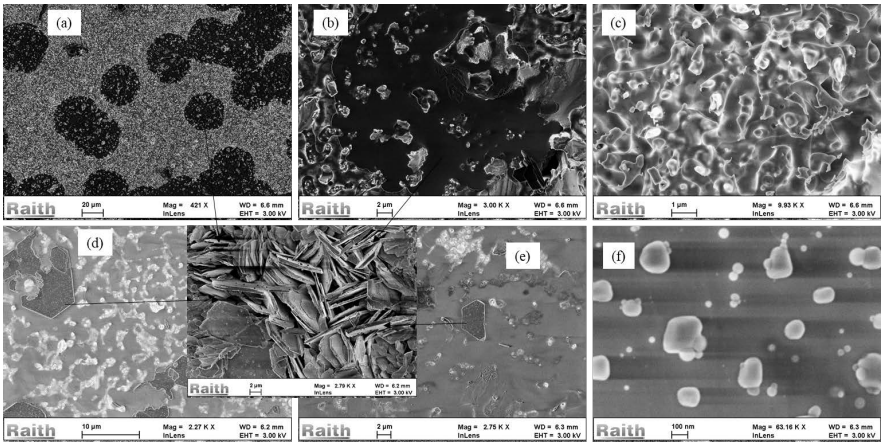

Figure 1. SEM images of (a) normal, (b) zooming on black circle and (c) zooming on gray zone for undoped; (d) normal zone 1, (e) normal zone 2 and (f) zooming on zone for 1% Mn doped PZN-4.5PT nanoparticles thin layers on <100> oriented silicon substrate.

to give a hexagonal nano-crystals; on the other hand it is possible that there is a reaction between Pb and the gel giving these nano-crystals), which could be explained by the formation of a new phase and due to the presence of new atoms from the gel containing nanoparticles such as Pb and P that may form new hexagonal complexes with Si thanks to annealing. In **Figure 1(c)** top terminals of silicon nanowires could be seen. **Figure 1(d)** to **Figure 1(f)** show homogeneous distribution of 1% Mn doped PZN-PT nanoparticles. However, it is interesting to notice that the local black circles are composed by hexagonal shapes nanocrystals (**Figure 1(d)**, **Figure 1(e)** and the zooming image). **Figure 1(f)** shows the distribution of the doped nanoparticles on the surface with sizes varying from less than 10 nm to around 200 nm.

3.2. Dielectric and Ferroelectric Characterization

Figure 2 shows the relative dielectric permittivity and dielectric losses as function of temperature. These curves reveal the presence of two transition temperatures (ferro-ferro and ferro-para). The first transition (T_{RT} = 130˚C) is assigned to a ferroelectric to ferroelectric phase transition which could be from a Rhombohedral and hexagonal mixte ferroelectric phase (perovskite nanoparticles and hexagonal nanocrystals) to another ferroelectric phase such as tetragonal or total hexagonal one. Doping did not affect this transition value and the value is closer to the bulk PZN-4.5PT crystals (130˚C [19]). The second peak (around 310˚C) corresponds to the transition from ferroelectric to paraelectric (T_c). According to **Figure 2(a)** and **Figure 2(b)**, showing permittivity and dielectric losses temperature dependence, for undoped and Mn doped PZN-4.5PT nanoparticles thin layers, Tc increased from 180˚C [19] to 310˚C respectively for bulk and for nanoparticles thin layers due to, probably, the gel effect. Relative dielectric permittivity (**Table 1**) values are very high at ambient temperature and 1 kHz (10^4 to 10^6 for undoped and 10^4 to 10^5 for doped nanoparticles) compared to the bulk one with 10^3 to 6×10^3. This remarkable increase in the dielectric permittivity

Table 1. Dielectric and transitions parameters of the undoped and Mn doped nanoparticles thin layers.

Thin films	ε_r (1 kHz) ambient T	$\tan\delta_e$ (%) ambient T	T_{RT} (˚C)	T_c (˚C)	ε_{rmax} (at Tc)	P_s (μC/cm²)	P_r (μC/cm²)	E_c (V/cm)
NW-PZN-4.5PT	$2.76 \times 10^4 \pm 100$	6.45 ± 1	130 ± 1	310 ± 1	$2.60 \times 10^7 \pm 100$	11.73 ± 0.1	10.20 ± 0.1	20 ± 1
PZN-4.5PT + 1% Mn	$17.7 \times 10^4 \pm 100$	5.00 ± 1	130 ± 1	305 ± 1	$3.00 \times 10^7 \pm 100$	22.22 ± 0.1	19.32 ± 0.1	20 ± 1

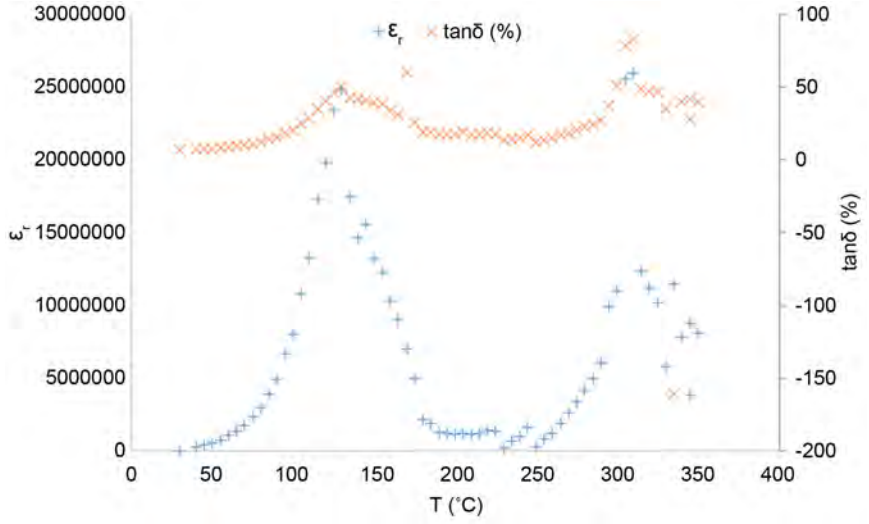

(a)

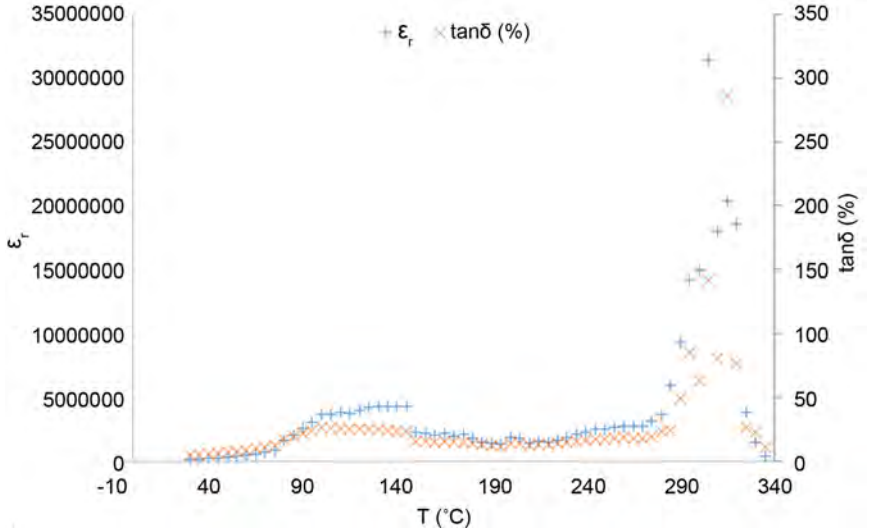

(b)

Figure 2. Relative dielectric permittivity and dielectric losses versus temperature for (a) undoped and (b) 1% Mn doped PZN-4.5PT nanoparticles thin films deposited on <100> oriented silicon nanowires substrate.

could be explained by the new phase from combination of Si-perovskite-gel overgrowth on the silicon surface. The dielectric losses are low compared to other high K materials; their values are equal to 6.45% and 5% respectively for the undoped and Mn doped PZN-4.5PT thin films. These values show that the mechanical factor would be very interesting and high. The results from dielectric

measurements show the potential application of such materials in micro and nanoelectronic devices as a colossal relative dielectric permittivity material.

Figure 3 represents the dielectric permittivity and dielectric losses dependence with applied electric field for undoped and Mn doped PZN-4.5PT thin films. From these curves it is clear that the dielectric permittivity value is very colossal in applied electric field conditions. It increases linearly between 15 ($\varepsilon_r \approx 1 \times 10^9$) to 25 V/cm reaching to its maximum value (5×10^9) at E ≈ 50 V/cm for undoped film and from 2×10^9 to 9×10^9 for the doped one (Figure 3(a)). Over 60 V/cm, the dielectric permittivity dropped down to its lowest values ($\varepsilon_r \approx 2 \times 10^9$ and 7×10^7 respectively for the undoped and Mn doped nanoparticles films). Physically, we supposed that increasing the voltage would permit some defaults and impurities to give enough energy for conduction band. So the increase of the material conductivity would certainly decrease permittivity property.

These results show that this new material could support very large electric field change (40 - 60 V/cm) compared to the other thin films dielectric. However,

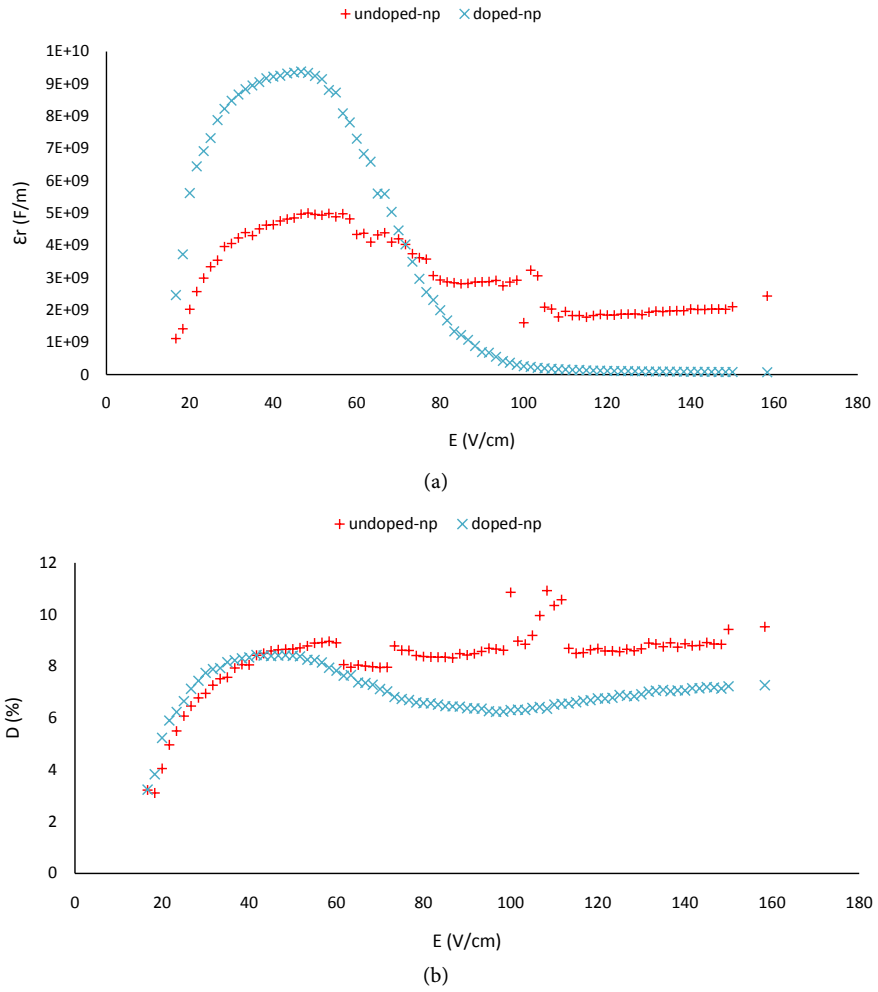

Figure 3. (a) Relative dielectric permittivity and (b) losses for undoped and 1% Mn doped PZN-4.5PT nanoparticles thin films deposited on <100> oriented silicon nanowires versus applied electric field.

over a certain value its performances would decrease. It exists a critical electric field value (around 60 V/cm) corresponding to the maximum dielectric permittivity for these materials polarization. The Mn doping did not greatly affect the thin films properties. However, it is clear that it stabilizes the electric field dependence (values are more stable compared to undoped). Indeed, one can see in **Figure 3(b)** that the losses are very stable for applied electric field over 60 V/cm with a value equal around 7% for the doped nanoparticles while it increases suddenly for the undoped one before being stable around 9%.

Figure 4 shows the dielectric permittivity and losses as function of frequency with bias on "off" (**Figure 4(a)** and **Figure 4(c)**) and with bias on "on" (**Figure 4(c)** and **Figure 4(d)**). We note that the bias is remaining at 0 V. The dielectric measurements are carried out as a function of frequency in the range of 100 Hz to 100 kHz to explore relaxation effects. The large dielectric constant for undoped thin film decreases continuously with an increase in frequency, which is a typical characteristic of any ferroelectric material. Whereas, for the Mn doped sample, the dielectric constant decreases slowly for the further increase in the frequency.

This kind of behavior usually comes from the space charges at low frequencies. Along with the improvement in the dielectric constant, an increase in the dielectric loss (**Figure 4(c)**) is also found for the doped nanoparticles thin film. The dielectric permittivity and losses behaviors in **Figure 4(a)** and **Figure 4(b)** (under 0V bias) are totally different to those from **Figure 4(a)** and **Figure 4(c)**. Indeed, in the latter we notice the presence of negative values (meaning negative capacity) over a certain apparent resonance frequency (around 10 kHz) for both materials. These negative values could come from charge injection and also charge accumulation due to the colossal dielectric permittivity. The relative dielectric permittivity values at high frequency are equal to 1.17×10^4 and 3.9×10^4 for respectively undoped and Mn doped thin films and with bias "off". These values are in the same range that those determined from dielectric permittivity-temperature curves at 1 kHz (**Table 1**). The permittivity values with bias on "on" at 0 V are negative and equal to -1.09×10^6 and -2.23×10^6 respectively for

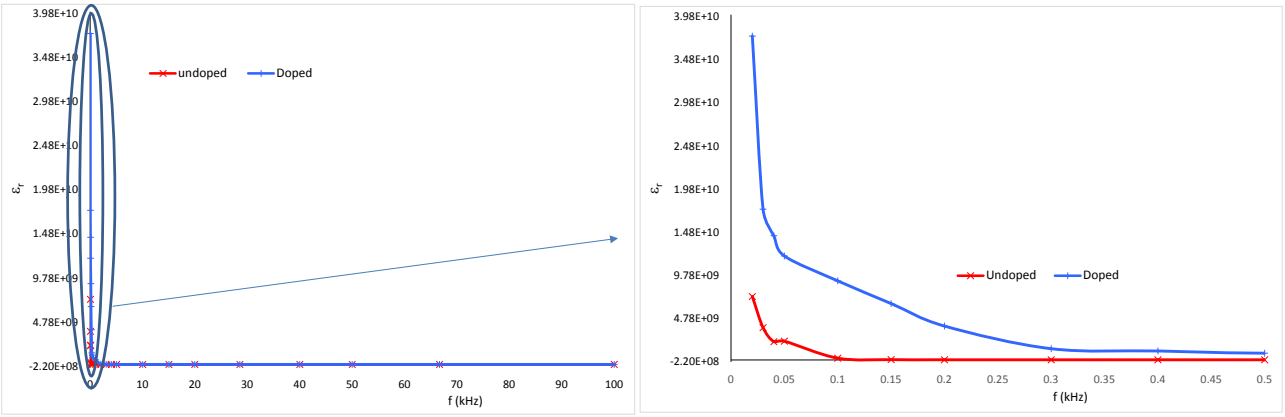

(a)

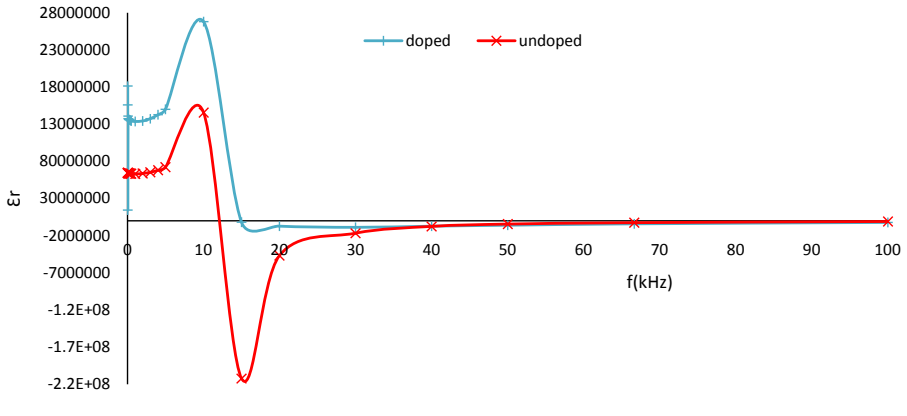

(b)

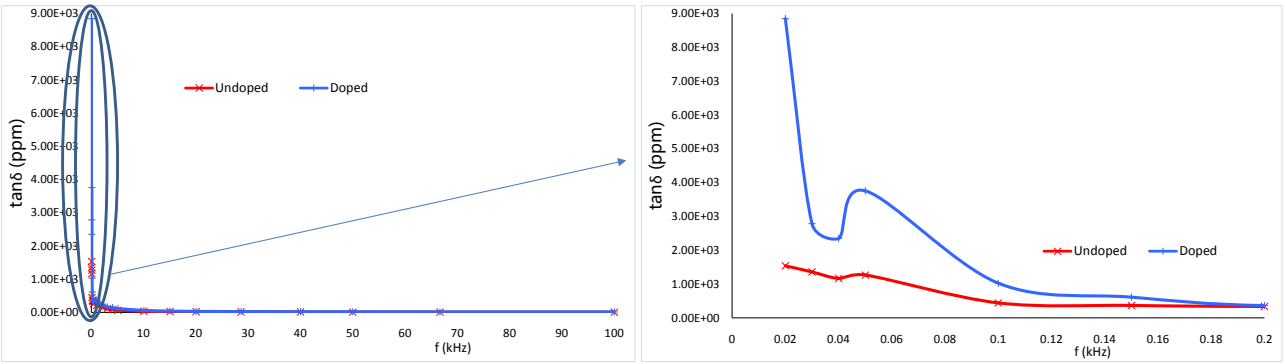

(c)

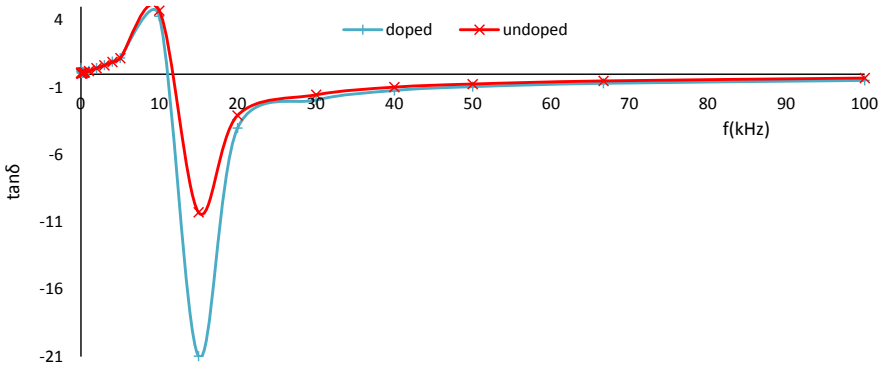

(d)

Figure 4. Dielectric permittivity versus frequency with (a) 0 V bias "on" and (b) bias "off"; dielectric losses (c) 0 V bias "on" and (d) bias "off" for undoped and Mn doped PZN-4.5PT nanoparticles thin films deposited on <100> oriented silicon nanowires.

undoped and Mn doped samples. The presence of bias since it is equal to 0 V increases highly the permittivity values and behavior both for the two films. As explained above, this could be due to charge injection and accumulation. These large relative dielectric values and low dielectric losses make these materials interesting candidates for ferrophotovoltaic and energy storage.

Figure 5 shows the room temperature dielectric constant and dielectric losses versus applied electric field of the Mn doped PZN-PT nanoparticles thin film. The curve is butterfly shaped, providing the evidence of weak ferroelectricity of

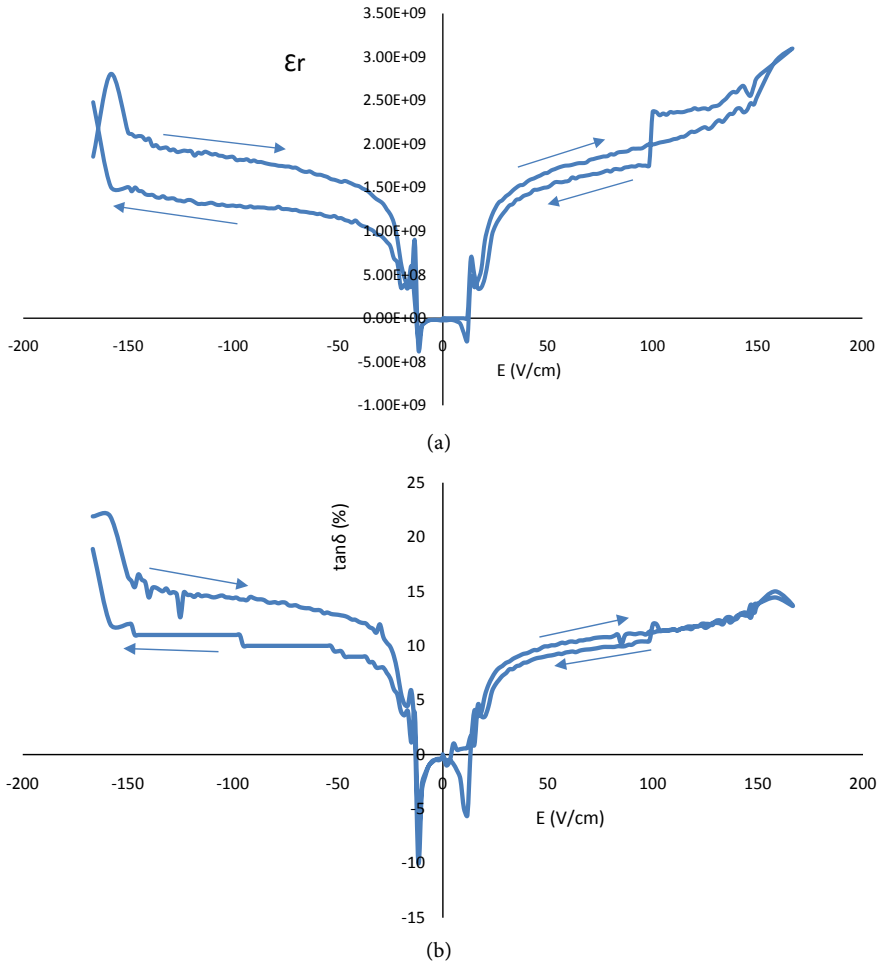

Figure 5. Completed cycles for (a) relative dielectric permittivity and (b) dielectric losses for 1% Mn doped PZN-4.5PT nanoparticles thin layers deposited on <100> oriented silicon nanowires substrate.

the PZN-PT thin films at room temperature. The tunability $((\varepsilon_{max} - \varepsilon_{min})/\varepsilon_{max})$ of the doped PZN-PT thin films is around 86%. This film showed very high tunability compared to those found in other ferroelectric materials such as the BNT-BT-ST thin films (29% and 35% [21]). This enhancement of dielectric constant was attributed to the relatively large hexagonal formed nanocrystals of the thin films due to the reaction between the gel and silicon substrate and also charge accumulation at the thin film and the electrode interface.

Figure 6(a) and **Figure 6(c)** show the stimulus and the response signals as a function of time. The stimulus triangle wave (X) and the voltage (sine wave) across the sense capacitor (Y) prompt the ferroelectric behavior of the thin films. The film capacitor is modulating the stimulus wave. The modulation by the ferroelectric capacitor is particularly apparent in **Figure 6(b)** and **Figure 6(d)**. This figure presents a ferroelectric hysteresis loop by using X:Y mode as explained in the experimental method described in [22]. The values of remnant polarization P_r, spontaneous polarization P_s and coercive field E_c are equal to 11.73 μC/cm^2, 10.20 μC/cm^2 and 20 V/cm, respectively for the undoped nanoparticles thin film

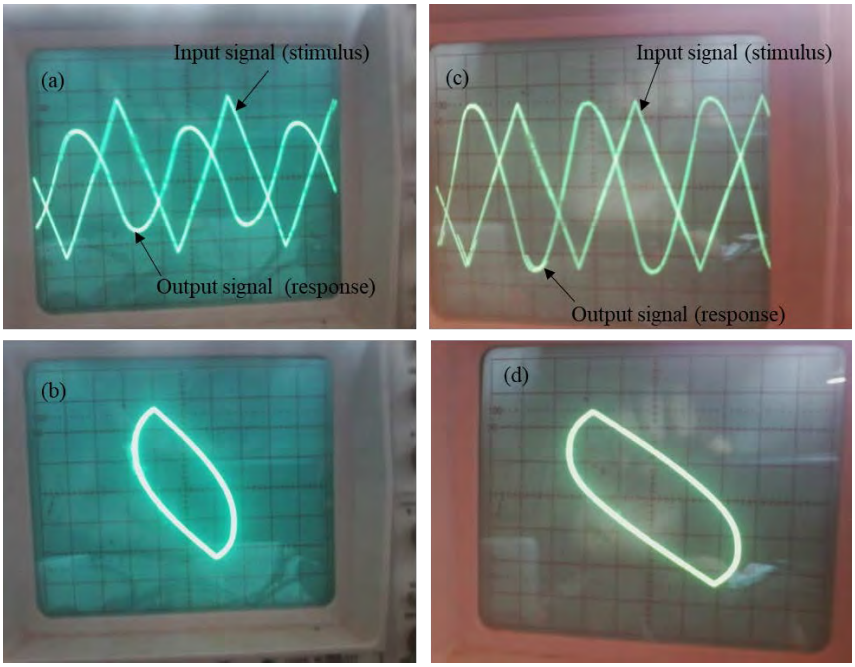

Figure 6. Modulation of the stimulus triangle wave and response (a) and (c) and their ferroelectric hysteresis loops (b) and (d) for respectively undoped and 1% Mn doped PZN-4.5PT nanoparticles thin layers on <100> oriented silicon nanowires.

and 22.22 μC/cm^2, 19.32 μC/cm^2 and 20 V/cm respectively for the Mn doped thin film. These values are large (high) and correspond to the best ones found in literature compared to typical ferroelectric thin films. One can see that Mn doping increases the polarization values. This is normal compared to the dielectric constant value in room temperature at 1 kHz increasing by doping (Table 1) facilitating charge accumulation and so polarization.

4. Conclusions

In this study, we fabricate with success PZN-4.5PT nanoparticles thin films. Their ferroelectric behavior has been demonstrated, measured and evaluated. We found colossal dielectric constant, which could be explained by the presence of new crystals components probably coming from the reaction between Si and the gel where nanoparticles were dispersed. These results make such thin films very potential candidates for energy storage and for ferrophotovoltaic application.

The determination of the composition of these hexagonal nanocrystals on the film surface and the origin of such colossal relative permittivity would be investigated.

Acknowledgements

This work is supported by Agence Universitaire de la Francophonie (AUF).

Conflicts of Interest

The authors declare no conflicts of interest regarding the publication of this paper.

References

[1] Qin, M., Yao, K. and Liang, Y.C. (2008) *Applied Physics Letters*, **93**, Article ID: 122904. https://doi.org/10.1063/1.2990754

[2] Fridkin, V.M. (2001) *Crystallography Reports*, **46**, 654-658. https://doi.org/10.1134/1.1387133

[3] Bernal, A., *et al.* (2012) *Advanced Materials*, **24**, 1160-1165. https://doi.org/10.1002/adma.201103993

[4] Yuriy, G., Olena, Z. and Anatoliy, G. (2012) Emerging Applications of Ferroelectric Nanoparticles in Materials Technologies, Biology and Medicine. In: Peláiz-Barranco, A., Ed., *Advances in Ferroelectrics*, IntechOpen, Rijeka Craotia, 475-497.

[5] Joshi, U.A. and Lee, J.S. (2005) *Small*, **1**, 1172-1176. https://doi.org/10.1002/smll.200500055

[6] Lang, X.Y. and Jiang, Q. (2007) *Journal of Nanoparticle Research*, **9**, 595-603. https://doi.org/10.1007/s11051-005-9066-1

[7] Varghese, J., Whatmore, R.W. and Holmes, J.D. (2013) *Journal of Materials Chemistry C*, **1**, 2618-2638. https://doi.org/10.1039/c3tc00597f

[8] Michael, T., Trimper, S. and Wesselinowa, J.M. (2006) *Physical Review B*, **74**, Article ID: 214113. https://doi.org/10.1103/PhysRevB.74.214113

[9] Basun, S.A., *et al.* (2011) *Physical Review B*, **84**, Article ID: 024105. https://doi.org/10.1103/PhysRevB.84.024105

[10] Bokov, V. A. and Myl'nikova, I.E. (1960) *Soviet Physics*, *Solid State*, **2**, 2428.

[11] Smolenskii, G.A., Isupov, V.A., Agranovskaya, A.I. and Popov, S.N. (1961) *Soviet Physics*, *Solid State*, **2**, 2584.

[12] Nomura, S., Takahashi, T. and Yokomizo, Y. (1969) *Journal of the Physical Society of Japan*, **27**, 262. https://doi.org/10.1143/JPSJ.27.262

[13] Kuwata, J., Uchino, K. and Nomura, S. (1981) *Ferroelectrics*, **37**, 579-582. https://doi.org/10.1080/00150198108223490

[14] Kuwata, J., Uchino, K. and Nomura, S. (1982) *Japanese Journal of Applied Physics*, **21**, 1298. https://doi.org/10.1143/JJAP.21.1298

[15] Shrout, T.R., Change, Z.P., Kim, N. and Markgraf, S. (1990) *Ferroelectrics Letters Section*, **12**, 63-69. https://doi.org/10.1080/07315179008201118

[16] Mulvihill, M.L., Park, S.E., Risch, G., Li, Z., Uchino, K. and Shrout, T.R. (1996) *Japanese Journal of Applied Physics*, **35**, 3984. https://doi.org/10.1143/JJAP.35.3984

[17] Lebrun, L., Zhang, S., Randall, C.A., Shrout, T.R. and Guyomar, D. (2002) *Ceramic Transactions*, **136**, 117.

[18] Benayad, A., Kobor, D., Lebrun, L., Guiffard, B. and Guyomar, D. (2004) *Journal of Crystal Growth*, **270**, 137-144. https://doi.org/10.1016/j.jcrysgro.2004.06.017

[19] Kobor, D. (2005) Synthesis and Characterization of PZN-4.5PT Single Crystals by Flux Method. Thesis, INSA, Lyon.

[20] Prya, S. and Uchino, K. (2002) *Journal of Applied Physics*, **91**, 4515. https://doi.org/10.1063/1.1459101

[21] Li, W., *et al.* (2015) *Ceramics International*, **41**, S356-S360. https://doi.org/10.1016/j.ceramint.2015.03.178

[22] Kobor, D., *et al.* (2015) *Processing and Application of Ceramics*, **9**, 107-115. https://doi.org/10.2298/PAC1502107K

Journal of Modern Physics, 2019, 10, 624-634
http://www.scirp.org/journal/jmp
ISSN Online: 2153-120X
ISSN Print: 2153-1196

The Reciprocal Lattice in Hierarchic Quasicrystals

Antony J. Bourdillon

UHRL, San Jose, CA, USA
Email: bourdillona@sbcglobal.net

How to cite this paper: Bourdillon, A.J. (2019) The Reciprocal Lattice in Hierarchic Quasicrystals. *Journal of Modern Physics*, **10**, 624-634.
https://doi.org/10.4236/jmp.2019.106044

Received: April 5, 2019
Accepted: May 18, 2019
Published: May 21, 2019

Abstract

Initially, all that was known about diffraction in quasicrystals was its point group symmetry; nothing was known about the mechanism. The structure was more evident, and was called quasiperiodic. From mapping the *Mn* atoms by phase-contrast, optimum-defocus, electron microscopy, the progress towards identifying unit cell, cluster, supercluster and extensive hierarchic structure is evident. The structure is ordered and uniquely icosahedral. From the known structure, we could calculate structure factors. They were all zero. The quasi structure factor is an iterative procedure on the hierarchic structure that correctly calculates diffraction beam intensities in 3-dimensional space. By a creative device, the diffraction is demonstrated to occur off the Bragg condition; the quasi-Bragg condition implies a metric that enables definition and measurement of the lattice constant. The reciprocal lattice is the 3-dimensional diffraction pattern. Typically, it builds on Euclidean axes with coordinates in geometric series, but it also transforms to Cartesian coordinates.

Keywords

Quasicrystal, Icosahedral, Lattice Constant, Reciprocal Lattice, Diffraction, Structure, Metric, Geometric Series, Quasi-Bragg Law, Quasi Structure Factor

1. Introduction

Rapidly cooled Al_6Mn has a phase, supposedly with "Long range orientational order and no translational symmetry" [1]. In fact, it produces sharp icosahedral diffraction owing to hierarchic translational structure. Its five-fold rotation axes are forbidden in classical crystallography owing to space filling constraints, and its icosahedral structure lies outside the limitations of the fourteen Bravais lattices allowed in crystallography. The "long range order" has been long debated, but with minimal progress in understanding how a periodic incident beam,

whether of electrons or X-rays, diffracts coherently from the "quasiperiodic" lattice.

The foremost beginning lies in the formula: *Mn* has an atomic number that is almost double that of *Al*. Consequently imaging, in phase-contrast, optimum defocus, transmission, electron microscopy [2], maps the heavier element which has four times the scattering power of the lighter one. Knowledge of the magnifying power of the microscope then reveals that the intervening atoms are *Al* that forms about the central *Mn* in edge-sharing $Al_{12}Mn$ unit cells. The resulting stoichiometry is Al_6Mn, as in the melt before crystallization and as in elemental analysis. Being edge sharing the structure is not space filling. (By contrast, all crystals are both face sharing and space filling.) In icosahedral i-Al_6Mn, the relative atomic sizes are perfect for extremely dense packing in icosahedral coordination [3] [4] [5] [6][1]. The unit cells cluster into icosahedral structures in at least four tiers of icosahedral hierarchy, seen in the image. There are good reasons for projecting the hierarchy to extend infinitely.

The stereogram of the principal axes and of principal reflecting planes in the icosahedral structure is, in its simplest form, 3-dimensional; indexed in geometric series; and complete [7]. Axial diffraction patterns have been likewise indexed [3] [4]. Every component in every beam, in each diffraction plane normal to major axes, has been precisely indexed by additions of one or two members of the geometric series. With this description of the pattern, and knowing the structure, the diffraction is simulated by normal scientific method [8] [9][2], as outlined below.

Because Bragg diffraction is well understood in its wide application to *crystals*, it is a mildly useful foil for understanding diffraction in quasicrystals, but only if differences are emphasized. Bragg's law describes the linear series of diffraction orders, $n = 0, 1, 2, 3 \ldots$, that result from periodically spaced reflecting planes of atoms. For the simple case of high energy electron diffraction from a cubic crystal, we can write approximately:

$$n \approx \frac{d \cdot \Theta}{\lambda} = \frac{a \cdot \Theta_{hkl}}{\lambda\left(h^2 + k^2 + l^2\right)^{1/2}} \tag{1}$$

where the scattering angle, $\Theta \approx 2\sin(\theta)$ for the Bragg complement to the angle of incidence θ; while d is the periodic interplanar spacing; and $\lambda << d$ is the wavelength of the incident beam. For each indexed scattering angle Θ_{hkl} in a cubic crystal with lattice parameter a, there corresponds an interplanar spacing $d_{hkl} = a/(h^2 + k^2 + l^2)^{1/2}$, h, k, and l positive integral.

By contrast, the *quasicrystal* (QC) does not have regular, periodic, interplanar spacings, and the orders in the diffraction pattern are in geometric series τ^m. Moreover, the relations between scattering angle Θ', d' and λ were *a priori* un-

[1]All diatomic quasicrystals have diameter ratios for central atom/matrix atoms of $(1 + \tau)^{1/2} - 1$, *i.e.* equal to the diagonal/side ratio in the golden rectangle.

[2]By an application of Ockham's razor, "Dimensions should not be multiplied without necessity": because axioms are unquestioned in math, they are meaningless in physics—as are all other unfalsifiable hypotheses [8] [9].

known. Supposing modified relations, the following solution is consistent with the diffraction pattern:

$$\tau^m \approx \frac{d'\Theta'}{\lambda}, \; m \text{ positive or negative integral,} \tag{2}$$

with details to be determined by simulation and experimental consistency. Every atom scatters. We have to suppose that in any given QC orientation, either most atoms scatter randomly but that atoms in adjacent planes may filter coherent scattering for the appropriate d' spacing; or that all atoms in the geometric structure coherently scatter the incident periodic wave. The former supposition is falsified because known interplanar spacings do not match Equation (1); the following evaluation of quasi scattering factors is a numerical solution that describes the coherent sharp diffraction that follows Equation (2). Complete analysis is work in progress.

Meanwhile, consistency is required between structure, scattering, and measurement. In particular, and consequent on optimum defocus imaging, it is clear that the unit cell has dimensions $a(1 \times \tau)$, where a is the quasilattice parameter that requires measurement, and the bracket gives the dimensions of the golden rectangle [3] [10]. (All 30 edges in the icosahedron belong to 15 golden rectangles through its center.) Given the structure, the parameter must be close to the diameter of the *Al* atom. Neighboring cells have common edges, but not common faces.

In *crystals*, Equation (1) provides the principal condition required for diffraction, and it is harmonic in order *n*. However, the equation is not a sufficient condition. Many indexed beams that are allowed by the equation are in fact forbidden by symmetric details within the periodic unit cells [11]. Classically, the structure factor method is used to identify them. By contrast, the *quasicrystal* unit cell is not periodic, so a more complex calculation is needed to identify and simulate the many and varied, beam intensities that occur in the geometric series diffraction pattern. Knowing, from optimum defocus imaging, the detailed structure of i-Al_6Mn, we can proceed to compare diffracted beam intensities by simulations of Quasi Structure Factors. We need to simulate, not only the supposition of Equation (2), but also to measure the lattice parameter *a*, along with beam intensities and other features of the diffraction pattern. The fact that the known structure—at least when considered as ideal and defect free—is uniquely icosahedral, is confirmation of its correspondence with the point group symmetry of the diffraction pattern. The quasi structure factors are calculated from the known ideal structure.

2. Hierarchic Icosahedral Structure

Figure 1 shows a foil section of i-Al_6Mn imaged in phase-contrast, optimum-defocus, electron microscopy [3]. White dots map *Mn* because of its higher atomic number, *i.e.* in the thin foil, the principal contrast is due to the greater scattering power of *Mn* (atomic number 25) compared to *Al* (atomic number 13).

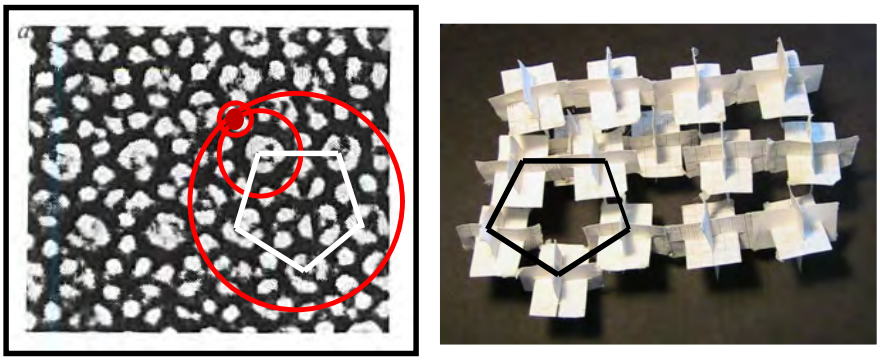

Figure 1. At left, phase-contrast, optimum defocus electron micrograph ([3] pp. 66-67) of *i-Al*$_6$*Mn* reveals icosahedrally coordinated *Mn* atoms as white dots and the filled red circle. *The red circles outline 4 tiers of ordered icosahedral clusters.* The large red circle outlines a supercluster section containing cluster centers at the corners of the white pentagon. At right, the black pentagon models the section by mirror image. Here, the triads of golden rectangles represent icosahedral clusters of twelve unit cells (two on each central axis), icosahedrally coordinated.

The *Mn* atom is the first of four tiers of icosahedral structure (red circles). When combined with all of the information given by the point group symmetry of the diffraction pattern [1]; and with the 3-dimensional stereogram of principal axes and diffraction planes [7]; while furthermore having patterns in geometric series completely indexed, the structure is evident. This series is intuitively consistent with the idea of hierarchic structure, and is proved to be so by calculations of quasi structure factors. While the model is an ideal representation for the rapidly quenched intermetallic alloy; the probability of deriving this image from any other structure that has been proposed (e.g. [12]) is absurdly small.

3. Quasi Structure Factors (QSF)

Whereas, in *crystals*, the Bragg condition (Equation (1)) determines harmonic factors n that relate λ to Θ; corresponding structure factors sum atomic scattering amplitudes that determine intensities and forbidden lines. Likewise in *quasi-crystals*, the dual importance of the quasi-Bragg condition and quasi-structure factors applies, but especially so because line intensities are many and varied. The general application of the formulae has been previously described [5], but we need to revisit the prerequisite of indexation. Begin with the atomic coordinates for the unit cell and cluster:

$$\begin{aligned}&\text{Unit cell}\left(r_u\right): Mn:\left(0,0,0\right)\\ &\qquad Al:1/2\left(\pm\tau,0,\pm;1\right),1/2\left(0,\pm1,\pm\tau\right),\ \text{and}\ 1/2\left(\pm1,\pm\tau,0\right)\\ &\text{Cell or Cluster centers}\left(r_{cc}\right):1/2\left(\pm\tau^2,0,\pm\tau\right),1/2\left(0,\pm\tau,\pm\tau^2\right),1/2\left(\pm\tau,\pm\tau^2,0\right).\end{aligned} \tag{3}$$

In *crystals* (that obey Equation (1)), the structure factor formula projects each atomic site at vector r_i in a unit cell onto a selected plane normal having integral indices *hkl* (Equation (1) with c_s = 1). By summing the projected cosines on non-equivalent atoms, an amplitude is obtained that corresponds to the intensity

of the (*hkl*) diffracted beam after a crystal is oriented to the Bragg condition. For example, the closest crystalline approximant to i-Al_6Mn is second phase, face centered cubic (fcc) Al_xMn, $x >> 6$ [7]. About the [110] axis diffracted beams have either all indices even or all odd; otherwise diffraction is forbidden by the symmetry of the unit cell [11]. The structure factors F_{hkl} have values equal to either 0 or 4. The atomic scattering factor is f_i and, in the crystal, the metric $c_s = 1$:

$$F_{hkl} = \sum_{i=1}^{N} f_i \cos\left(2\pi \cdot c_s \left(\overline{h_{hkl}} \cdot \overline{r_i}\right)\right) \tag{4}$$

By contrast, in icosahedral *quasicrystals* (that obey Equation (2)), quasi-structure factors (QSFs) are more complex and more varied: because it is not structurally periodic, the summation in Equation (4) is extended to clusters and superclusters indefinitely. Write the vector from the origin to each atom in a cluster $\overline{r_{cl}}$ as the sum of a unit cell vector $\overline{r_u}$ used previously, with a vector to the cell centers in the cluster $\overline{r_{cc}} : \overline{r_{cl}} = \overline{r_{cc}} + \overline{r_u}$. Then since

$$\sum_{i}^{N\text{cluster}} \exp\left(\overline{h_{hkl}} \cdot \overline{r_{cl}}\right) = \sum_{i}^{12} \exp\left(\overline{h_{hkl}} \cdot \overline{r_{cc}}\right) \times \sum_{i}^{13} \exp\left(\overline{h_{hkl}} \cdot \overline{r_u}\right) \tag{5}$$

with corresponding summations over cell centers and unit cell sites, $N_{\text{cluster}} = N_{cc} \cdot N_u$, the QSF for the cluster may be calculated:

$$F_{hkl}^{\text{cluster}} = \sum_{i=1}^{12} \cos\left(2\pi \cdot c_s \left(\overline{h_{hkl}} \cdot \overline{r_{cc}}\right)\right) \cdot F_{hkl}^{\text{cell}} \tag{6}$$

and the calculation iterates on superclusters orders 1, 2, 3 ... p, by inclusion of the stretching factor τ^{2P}:

$$F_{hkl}^{p} = \sum_{i=1}^{12} \cos\left(2\pi \cdot c_s \left(\overline{h_{hkl}} \cdot \tau^{2p} \overline{r_{cc}}\right)\right) \times F_{hkl}^{p-1} \tag{7}$$

F_{hkl}^{cluster} may also be written F_{hkl}^{0}. The iteration is important when the calculation is performed over large clusters, for then truncation errors due to the many additions tend to randomize answers. Though large clusters yield precise conclusions [3] [4] here we will be concerned rather with diffraction effects at the cell and cluster levels up to supercluster order 2. Notice, by contrast with (periodic) crystals, that a line that is forbidden, or partly forbidden at the cell level may be allowed by different greater dimensions at cluster and higher order levels. We therefore begin by supposing that the diffraction is in first Bragg order $n = 1$, and proceed to determine details in the quasi Bragg law (Equation (2)), including the calculated ratio dh/dc_s. The negative derivative that will be calculated is used to refine former results.

Figure 2 shows simulations for QSFs in the geometric series (100), (τ00), ($\tau^2$00), ($\tau^3$00) and ($\tau^4$00), all plotted against varying values for the metric c_s. Each plot contains a single peak centered at $c_s = 0.894$; no other significant structure is found between $1.2 > c_s > 0.8$. The plots confirm the geometric series diffraction that is observed in diffraction patterns, and that was discovered in the stereograms [7] and indexation [3]. Moreover, the plots confirm the explanation for the geometric series being due to the hierarchic structure. The series shown is

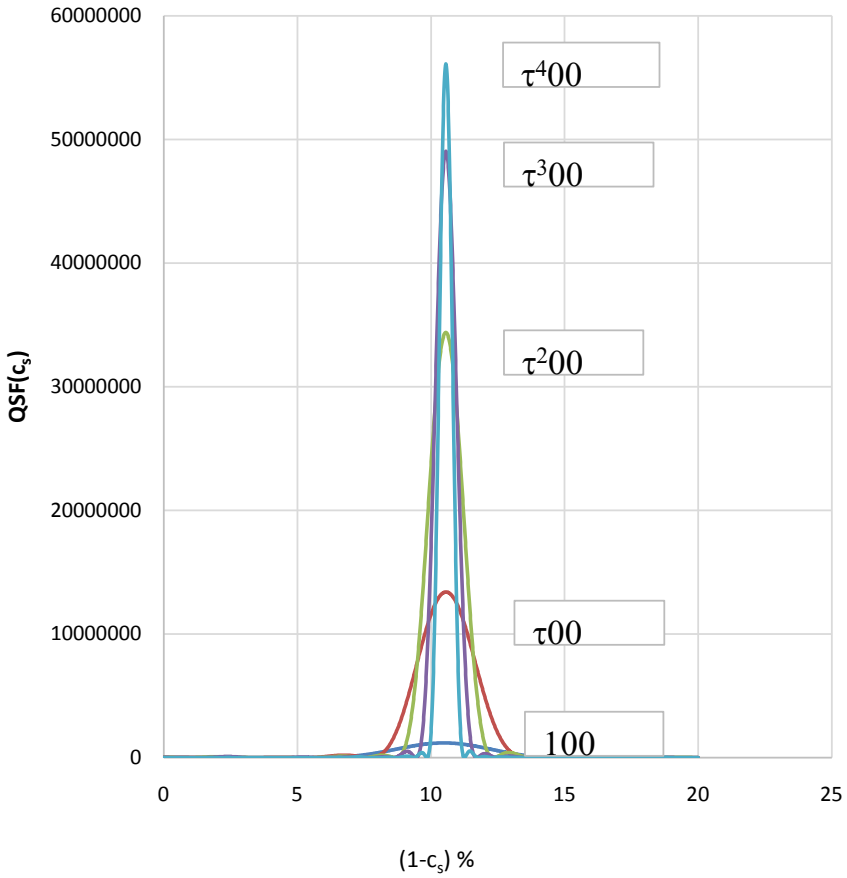

Figure 2. QSFs simulated for indexed lines as shown from an i-Al_6Mn supercluster order 2. The lines peak consistently when $c_s = 0.894$ with similar intensities (FWHM). By contrast corresponding QSFs for Bragg conditions ($c_s = 1$ and $n = 0, 1, 2, 3\ldots$, $m = 0$) are unregulated, with more or less random QSF structures, spread out and very weak, like noise.

illustrative: all simulated peaks from the quasicrystal occur with the same metric (*i.e.* the value of c_s when the QSF peaks). The plots also emphasize the critical and creative importance of the metric for the confirmation of Equation (2).

The significance of **Figure 2** is further illustrated by comparing equivalent scans calculated for crystals [4]. Owing to the condition expressed in Equation (1), all "QSFs" calculated for *crystals* peak only on the ordinate axis ($c_s = 1$). Moreover, in the simple case of fcc *Al* for example, the number of values calculated is limited, typically 4 or 2 or zero, there being only four non-equivalent atoms in the unit cell. By contrast, not only do quasicrystal QSFs peak only at a precise off-Bragg condition ($c_s = 0.894$; $\Theta' = \Theta/c_s$; $d' = d{\cdot}c_s$) in Equation (2) and **Table 1** below, but the intensities have a wide spectrum of values over various diffraction beams (*hkl*). This variety is due to the larger number of atoms that contribute to the diffraction from large clusters, *i.e.* much greater than the number in a single unit cell.

The peaks describe a new physical effect in quasicrystals. In *crystals*, Bragg's law (as in Equation (1)) supposed a simple model, with elementary mathematics and clear experimental evidence. By contrast, *quasicrystals* are described by

Table 1. Calculation for the lattice parameter a' in the quasicrystal from measurements made by assuming Bragg diffraction.

Bragg condition	Quasi-Bragg condition	Comment
$n\lambda \approx d\Theta$	$\tau^m\lambda \approx d'\Theta'$	Including metric, ('), n, m integral $m = -$infinity, −1, 0 1, 2, 3… or $h' = 0, \tau^{-1}, 1, \tau, \tau^{-1}, \tau^{-2}, \tau^{-3}$…
$d = a/h$	$d' = a'/h'$	r is fixed within known models
		Diffraction depends on harmonic r. h in SF for Equation (1) & QSF for (2)
$c_s = 1$	$c_s < 1$	In quasi Bragg h' $c_s < h$ $d'_{r00} = 0.205 \times c_s$ nm $d'_{100} = 0.205 \times c_s \times \tau = 0.296$ nm, $= a'$

equally simple mathematics (Equation (2), Equations (5)-(7)), and equally clear diffraction evidence, but require a more complex model. The equations and evidence imply that the sums on the cosines in Equation (7), when each is multiplied by planar densities taken from the structure, result in specular reflection from imaginary planes that are 10% shifted from the corresponding Bragg condition. This is the most remarkable feature of the hierarchic scattering that is observed in geometric series (Equation (2)). The shift is $1 - c_s$ at the peak.

Notice that in the experimental high energy electron diffraction pattern, the intensities of the higher orders are further and normally reduced by the deviation parameter, that result from larger scattering angles [12]. The "third bright ring" is exceptional and is described further below where it is used to define the quasi lattice parameter.

All atom sites in Equation (7) were summed for the supercluster order 2, but with four adjustments: edge cell atoms that were counted twice were entered by halving the atomic scattering factor f_{Al}; *secondly*, those that were counted thrice, at intersections of three cells, were entered with one third f_{Al}. *Thirdly*, mobile sites, where one atom shares two sites were counted as for edge sharing; and *fourthly*, *s*ome details were ignored because of their small effects and uncertainty. For example, Pauling's observation [13] that though icosahedral structures are known in crystals having large unit cells, the structures contain holes at their centers. These holes contain less than 2% of the volume of icosahedral structures. In principle the holes can be filled with octahedral structures (the octahedron is a subgroup of the icosahedral group and so should not display obvious effects in diffraction). However, we have chosen to ignore hole fillings because various fillings are possible.

Given the method of indexation described, the scattering is thus seen to be coherent when the metric $c_s = 0.894$[3]. **Figure 2** is an example of the general re-

[3]When the calculations were undertaken earlier under the assumption of second Bragg order, $n = 2$, a different value was found with a value for $1 - c_s$ about 5% instead of 10% as in **Figure 1**. On reflection, this will be seen to be consistent; and the assumption depended on the symmetry of the unit cell. However, since it is now obvious from Equations (5)-(7) that structure factors depend on both the unit cell and the on the clusters, the earlier hypothesis that $n = 2$ is corrected and is replaced by indexation based on $n = 1$.

sult that is calculated in quasicrystal diffraction. We now need to consider how to apply the calculated metric for the hierarchic structure.

Figure 3 illustrates five simulations using four imagined pseudo-indices having h = 1.5, 1.6, 1.7 and 1.8, and also the midway index at h = 1.618034…, the (τ, 0, 0), *i.e.* consistent with quasi-Bragg diffraction in Equation (2), with m = 1. The pseudo-indices are anharmonic and unreal because the corresponding m is fractional. The central peak in Figure 3 is the second peak in Figure 2. The peak intensities are constant. By plotting, separately, the index against the peak positions, the linear slope dh/dc_s is found to be −0.186, *i.e.* negative. A similar relationship between indexation with interplanar spacing applies to quasicrystals as to crystals (namely $d_{hkl} = a/(h^2 + k^2 + l^2)$) so the derivative dd_{hkl}/dc_s must be positive. This fact is used to derive the true quasicrystal lattice parameter a' in Table 1. This parameter is the corrected value that, previously, was supposedly measured by incorrectly by assuming second order (n = 2) Bragg diffraction in the quasicrystal. The calculated slope demonstrates the fact that the lattice parameter that was previously measured by assuming Bragg diffraction, was overestimated (Table 1).

4. Quasi Lattice Parameter and Reciprocal Lattice

The parameter is at first sight ambiguous because the unit cells are edge sharing. Fixed are the stretching factor τ^2; the icosahedron cell length $\tau{\cdot}a'$, and its side length $1{\cdot}a'$; but the two most obvious subordinate cells are overlapping cubes side $\tau{\cdot}a'$, or floating cubes side a' with severe underfilling. The measured lattice parameter is reported to be a = 0.205 nm [12] [14], *i.e.* measured from the "third bright ring" [1] [15], following the methods of classical Bragg diffraction. In the crystallography of cubic materials, an interplanar spacing d and scttering vector Θ depend on h^{-1} and h respectively, in a (h00) line. However in the quasicrystal,

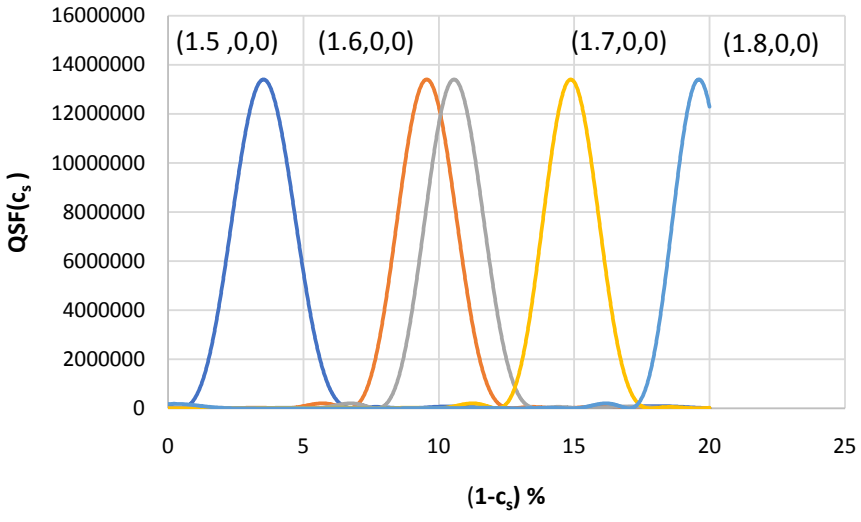

Figure 3. Simulations for QSFs plotted against various trials of metric c_s, where the index is also varied by imaginative construction. The relationship is almost linear dh/dc_s = −1.86.

the off-Bragg condition requires correction for c_s. Then the cell side length measures as $0.205 \times c_s \times \tau = 0.296$ nm (Table 1), or 3% greater than the diameter of *Al* in the pure metal. The measurement of *a'* depends on correct conventions of indexation and definition. It is convenient to define the lattice parameter a' in i-Al_6Mn, as the normal diameter of *Al* in the unit cell of pure *Al*. We therefore define the quasi-lattice parameter as the width of the icosahedral unit cell. When we progress to the reciprocal lattice, it is convenient to express the parameter in simplified icosahedral units, $a' = 1$. This corresponds with the fact that in hierarchic quasicrystals, diffraction measurement occurs through the compromise multi-spacing effect, or metric, c_s.

Quasicrystal crystallographers sometimes ask about the reciprocal lattice in *quasicrystals* because the reciprocals provide important understanding in measurement from *crystals*.

This understanding extends to most of the solid state physics of crystals, including energy band structures, conductivity etc. In early researches, alternative bases were sometimes used to index the diffraction pattern, but the Euclidean axes of the O_h subgroup of the icosahedral point group are now standard.

Should we use coordinates that are Cartesian, or coordinates in geometric series? The former represent the unit cell parameter a' in linear order, and so are the more convenient choice for some purposes. More generally, the geometric series expansion of the hierarchic solid relates to the true structure.

Meanwhile, the reciprocal lattice in momentum space has the same point group symmetry as the solid structure and Euclidean axes are again the best choice. The 3-dimensional lattice may be calculated from QSFs using power values for *h*, *k* and *l* equal to τ^m, $m = -$infinity, −1, 0 1, 2, 3… A diffraction pattern is a projection of a reciprocal lattice onto two dimensions. The reciprocal lattice may be recorded by abscissae coordinates in either linear or geometric series. The latter series has been used to construct dispersion curves ([16] [17] p. 17), with energy space ordinates plotted against *k* vector abscissae. In geometric coordinates, the free electron dispersion is then a straight line with slope 2. Meanwhile, because the geometric series, base τ, is a particular Fibonacci sequence, quasi-Bragg reflected beams in the extended zone scheme have the slope −1. Zone boundaries are constructed on linear units *m* in the power series τ^m coordinates. By simple transformation, extended zones can be represented on alternative linear coordinates. Another example is for high energy electrons used in imaging. Dispersion is represented in momentum ordinates with scattering vector abscissae ([17] p. 51). This dispersion is useful for describing the dynamics of quasi-Bloch waves [5]. Each representation, geometric series or linear, has its merits, while results are mutually transformable.

Knowing the clear icosahedral structure, corresponding progress is also expected in defect structures (e.g. [7]) in rapidly quenched material. A further expectation is application of the quasi structure factor method to 2-dimensional quasi-crystalloid structures, *i.e.* with periodicity on the c-axis but having 10-fold, 6-fold or 8-fold rotational symmetries (e.g. [17] p. 68). We use math, but only

when it is falsifiable (*cf.* [4] p. 83); and not where it is falsified.

5. Conclusion

We do not ask "What is a quasicrystal?" [18]. "The short answer is no one is sure." With the mapping of *Mn*, and with the extension of the hierarchic structures from cell to cluster to superclusters of infinite order, the structure is known. With the stereographic projections of principal axes and diffraction planes indexed in three dimensions; with complete indexations based on summations of backbone geometric series in 3-dimensions; with the representation of all diffraction beams by quasi structure factors, the diffraction pattern is matched to the known structure. It is no wonder that the matching lattice constant and reciprocal lattice are consistently measured; the wonder is that periodic probes, whether of X-ray or electron beams, scatter coherently from the hierarchic, quasiperiodic structure. This coherence is firmly demonstrated by numerical methods applied on an off-Bragg condition, as this paper emphasizes. Though the quasicrystal lattice is geometric, the reciprocal lattice is easily transformed to linear coordinates.

Conflicts of Interest

The author declares no conflicts of interest regarding the publication of this paper.

References

[1] Shechtman, D., Blech, I., Gratias, D. and Cahn, J.W. (1984) *Physical Review Letters*, **53**, 1951-1953. https://doi.org/10.1103/PhysRevLett.53.1951

[2] Bursill, L.A. and Peng, J.L. (1985) *Nature*, **316**, 50-51. https://doi.org/10.1038/316050a0

[3] Bourdillon, A.J. (2009) Quasicrystals and Quasi Drivers. UHRL, San Jose.

[4] Bourdillon, A.J. (2012) Metric, Myth and Quasicrystals. UHRL, San Jose.

[5] Bourdillon, A.J. (2016) *Journal of Modern Physics*, **7** 43-50. https://doi.org/10.4236/jmp.2016.71005

[6] Bourdillon, A.J. (2011) Logarithmically Periodic Solids. Nova Science, New York.

[7] Bourdillon, A.J. (2013) *Micron*, **51**, 21-25. https://doi.org/10.1016/j.micron.2013.06.004

[8] Popper, K.R. (1959) The Logic of Scientific Discovery. Hutchinson, London. https://doi.org/10.1063/1.3060577

[9] Popper, K.R. (1982) Quantum Theory and the Schism in Physics. Hutchinson, London.

[10] Huntley, H.E. (1970) The Divine Proportion. Dover, New York.

[11] Cullity, B.D. (1978) Elements of X-Ray Diffraction. Addison-Wesley, Addison.

[12] Tsai, A.P. (2008) *Science and Technology of Advanced Materials*, **9**, 1-20.

[13] Hirsch, P., Howie, A., Nicholson, R.B., Pashley, D.W. and Whelan, M.J. (1977) Electron Microscopy of Thin Crystals. Krieger, New York.

[14] Bourdillon, A.J. (1987) *Philosophical Magazine Letters*, **55**, 21-26.

[15] Pauling, L. (1985) *Letters to Nature*, **317**, 512-514. https://doi.org/10.1038/317512a0

[16] Bourdillon, A.J. (2009) *Solid State Communications*, **149**, 1221-1225.

[17] Bourdillon, A.J. (2010) Quasicrystal's 2D Tile in 3D Superclusters. UHRL, San Jose.

[18] Senechal, M. (2006) *Notices to the American Mathematical Society*, **3**, 886-887.

Journal of Modern Physics, 2019, 10, 635-640
http://www.scirp.org/journal/jmp
ISSN Online: 2153-120X
ISSN Print: 2153-1196

Dark Energy and Dark Matter as Relative Energy between Quarks in Nucleon

F. C. Hoh

Retired, Uppsala, Sweden
Email: hoh@telia.com

How to cite this paper: Hoh, F.C. (2019) Dark Energy and Dark Matter as Relative Energy between Quarks in Nucleon. *Journal of Modern Physics*, **10**, 635-640.
https://doi.org/10.4236/jmp.2019.106045

Received: April 24, 2019
Accepted: May 20, 2019
Published: May 23, 2019

Abstract

Dark energy and dark matter in the universe are assigned to the positive and negative, respectively, "hidden" relative energies between the diquark and quark in nucleon in the scalar strong interaction hadron theory, SSI. The origin of the "darkness" is that quarks cannot be observed individually.

Keywords

Relative Energy among Quarks, Scalar Strong Interaction Hadron Theory, Dark Energy, Dark Matter

1. Introduction

The mass-energy density of the dominant cosmic constituents averaged over the entire universe is [1]

$$\textit{Dark energy: Dark matter: Ordinary matter} \approx 68.3\%:26.8\%:4.9\% \quad (1.1)$$

For the dark energy, there are various models: cosmological constant, quintessence, interacting dark energy… [1] ([2] pp. 497-500). For the dark matter, there are baryonic models and the more popular non-baryonic models: axions, neutrino with finite mass, WIMPs… ([3] pp. 123-125). None of them has any connection with any theory supported by laboratory measurements. The general consensus is that we do not what these dark constituents are.

The scalar strong interaction hadron theory SSI [4] [5], hereafter denoted by [I, II] has been relatively successful in accounting for low energy hadronic data. However, it contains "hidden", unobservable relative energies between the quarks. The physical role of these energies has been in general unknown.

The purpose of this paper is to show that the dark constituents in the universe can be identified as such "hidden" relative energies between quarks that condense into nucleons in the early universe.

2. Starting Wave Equations

The starting point is the SSI equations of motion for diquark-quark baryons ([6] (2.9)), [I, II (9.3.16)]. In these references, the quartet part in these equations has been separated off from their doublet or spin 1/2 part which reads [I, II (10.0.6)]:

$$\partial_I^{a\dot{b}}\partial_{II}^{f\dot{e}}\partial_I^{e\dot{f}}\chi_{0\dot{b}}\left(x_I,x_{II}\right)=-i2\left(M_b^3+\Phi_b\left(x_I,x_{II}\right)\right)\psi_0^a\left(x_I,x_{II}\right) \tag{2.1a}$$

$$\partial_{I\dot{b}c}\partial_{II\dot{e}h}\partial_{I\dot{h}e}\psi_0^c\left(x_I,x_{II}\right)=-i2\left(M_b^3+\Phi_b\left(x_I,x_{II}\right)\right)\chi_{0\dot{b}}\left(x_I,x_{II}\right) \tag{2.1b}$$

Here, x_I is the coordinate of the diquark, x_{II} that of the quark, $\partial_I=\partial/\partial x_I\cdots$, and χ_0 and ψ_0 the wave functions of the doublet baryons. The undotted and dotted spinor indices *a*, *b*, *e*… run from 1 to 2, $2M_b$ is the sum of the quark masses and Φ_b the strong diquark-quark interaction potential.

3. Laboratory and Relative Spaces

Since quarks cannot be observed, their coordinate spaces are converted into an observable laboratory space X^μ for the baryon and a relative space x between the diquark and the quark via the linear transformation given above ([7] (6.2)) or by ([6] (5.1)), [I, II (3.1.3a)]

$$x^\mu=x_{II}^\mu-x_I^\mu,\quad X^\mu=\left(1-a_m\right)x_I^\mu+a_m x_{II}^\mu \tag{3.1}$$

For observable particles, a_m is often determined by that X^μ is the center of mass of these particles. If these particles have equal mass, a_m = 1/2. Such kind of determination cannot be done here because quarks are not observable individually. a_m has been taken to be an arbitrary real constant and represents a new degree of freedom which underlies the present assignments of the dark constituents in §5-6 below.

The relative space $x=(x^0,\underline{x})$ is "hidden" [I, II (3.1.3)] and cannot be observed. If it were observable, then (3.1), with a given a_m, leads to that both the diquark at x_I and quark at x_{II} can be seen, contrary to experience. This can also be seen directly in the first of (3.1) in which the right side members cannot be measured; hence x^μ is also "hidden", independent of a_m. Nevertheless, the bulk of hadron physics in SSI lies in such "hidden" spaces.

The baryon wave functions in (2.1) are factorized into the form of [I, II (10.1.1)],

$$\begin{aligned}\chi_{0\dot{b}}\left(x_I,x_{II}\right)&=\chi_{0\dot{b}}\left(\underline{x}\right)\exp\left(-iK_\mu X^\mu+i\omega_K x^0\right)\\ \psi_0^a\left(x_I,x_{II}\right)&=\psi_0^a\left(\underline{x}\right)\exp\left(-iK_\mu X^\mu+i\omega_K x^0\right)\end{aligned} \tag{3.2}$$

$$K_\mu=\left(E_K,-\underline{K}\right)\quad\text{[I,II (3.1.6)]} \tag{3.3}$$

where E_K is the energy of the baryon and $\underline{K}$ its momentum. x^0 is the relative time and $-\omega_K$ the associated relative energy in the "hidden" relative space and cannot be observed within SSI.

In spherical coordinates, $\underline{x}=(r,\theta,\phi)$ [I, II (3.1.7b)], the doublet wave functions in (3.2) with total angular momentum j = 1/2 and orbital angular momentum l = 0 read [I, II (10.2.3)]

$$\psi_0^1(\underline{x}) = g_0(r)Y_{00}(\theta,\varphi) + if_0(r)\sqrt{\frac{1}{3}}Y_{10}(\theta,\varphi),\quad \psi_0^2(\underline{x}) = if_0(r)\sqrt{\frac{2}{3}}Y_{11}(\theta,\varphi) \quad (3.4)$$

where the Y's are the usual spherical harmonics. $\chi_{0\dot{a}}$ is found by changing the signs of $f_0(r)$ in (3.4).

4. Radial Wave Equations in Relative Space, Solutions and Results

Consider baryons at rest, $\underline{K} = 0$. $a_m = 1/2$ is set as in the meson case [I (3.5.7)], [II (5.7.2)]. Similarly, the "hidden" relative energy $-\omega_0 = 0$ is also set following the meson case [I (3.5.6)], [II (5.7.1)]. Insertion of (3.1-4) into (2.1) using [I, II (3.1.4)] leads to the radial wave equations ([6] (6.9)), [I, II (10.2.12)]

$$\left[\frac{E_{0d}^3}{8} + M_b^3 + \Phi_{bd}(r) + \frac{E_{0d}}{2}\Delta_0\right]g_0(r) + \left(\frac{E_{0d}^2}{4} + \Delta_0\right)\left(\frac{\partial}{\partial r} + \frac{2}{r}\right)f_0(r) = 0 \quad (4.1a)$$

$$\left[\frac{E_{0d}^3}{8} - M_b^3 - \Phi_{bd}(r) + \frac{E_{0d}}{2}\Delta_1\right]f_0(r) - \left(\frac{E_{0d}^2}{4} + \Delta_1\right)\frac{\partial}{\partial r}g_0(r) = 0 \quad (4.1b)$$

where the subscript d denotes doublet and [I, II (10.2.2a)] gives the diquark-quark strong interaction potential

$$\Phi_{bd}(r) = \frac{d_b}{r} + d_{b0} + d_{b1}r + d_{b2}r^2 + d_{b4}r^4 \quad (4.2)$$

Here, the nonlinear potential $\Phi_{cd}(\underline{x})$ [I, II (10.2.2)] vanishes for large normalization volume $\Omega_{cb} \to \infty$ in [I, II (10.3.14)]. The d_b's are unknown integration constants.

The two coupled third order equations (4.1) have been converted into six first order equations [I (10.7.5)], [II (10.4.5)] which have been treated numerically for the neutron in [I §11.1.1], [II §11.1.2]. Due to the large number of unknown d_b constants, (4.1-2) could not be solved as a conventional eigenvalue problem. A less ambitious approach has been adopted; the known mass of the neutron is used as input and the d_b's are adjusted such that $g_0(r)$ and $f_0(r)$ converge at large r. The so-obtained neutron wave functions are plotted in [I Figure 12.1], [II Figure 11.1b] and led to the nearly correct predictions of the neutron life and the electron asymmetry parameter A or the neutrino asymmetry parameter B [II Table 12.1] in its beta decay. These results support the basic correctness of SSI in the baryon sector.

5. "Hidden" Relative Energy, Dark Energy and Dark Matter

If $a_m = 1/2$ and $-\omega_0 = 0$ used in (4.1) were not assumed, (4.1) will be modified by

$$E_{0d} \to E_{0d} - 2E_{0d}\left[a_m - \frac{1}{2} - \frac{\omega_0}{E_{0d}}\right] \quad (5.1)$$

This relation leads to that E_{0d}, hence also (4.1), remain unchanged if the bracket in (5.1) vanishes or

$$a_m = \frac{1}{2} + \frac{\omega_0}{E_0} \tag{5.2}$$

which was first written down in 1993 in the basic SSI paper ([7] (6.6)) or [I, II (3.1.10a)] for mesons at rest, unaware of its present implication. This condition removes the dependence of the unknown relative energy $-\omega_0$ in the meson wave equations in the relative space [I, II (3.1.8)] as well as those in the baryon case mentioned beneath [I, II (10.1.1)].

The choice $a_m = 1/2$ and $-\omega_0 = 0$ in (4.1) is thus a special case of (5.2). Since a_m can be any real constant in (3.1), the relative energy $-\omega_0$ in (5.2) also can become any real constant energy, albeit "hidden" or not observable within the framework of SSI.

The rest frame baryon energy E_{0d} in (4.1) is the baryon mass, observable in SSI, and will behave as ordinary matter in external gravitational fields. The associated relative energy $-\omega_0$ appears next to, and is on the same footing with, E_{0d} in (5.1) is however "hidden", not observable in SSI, but will similarly interact with external gravitational fields and is interpreted as dark energy, which is obtained if $a_m < 1/2$ is chosen in (5.2). If the associated relative energy $-\omega_0$ is negative, obtainable if $a_m > 1/2$ and also not observable within SSI, it will analogously interact with external gravitational fields and is assigned to represent dark matter, since it is expected to attract positive energy-matter.

The origin of the "darkness" is that quarks cannot be observed which led to (3.1).

6. Cosmological Implications

6.1. Dark Energy, Dark Matter and Formation of Nucleons

In the standard big bang model, hot quark-gluon plasma with fully relativistic *u* and *d* quarks was present when the universe was about 10 μs old ([2] §12.10). In SSI, this situation will be modified due to the much greater quark masses [I, II Table 5.2], Further, this plasma contains quarks only; gluons are not needed and appear later in hadrons formed by these quarks which then acquire "colors" or internal degrees of freedom characterized by internal coordinates z_I, z_{II} and z_{III} [I, II §2.3.2], [II Sec. 14.2-3]. As the universe expands and the density of this plasma drops to a *freeze-out* density, hadrons are formed, eventually preceded by formation of diquarks.

Each of the rest frame hadrons can have $a_m \neq 1/2$ in (3.1) and a relative energy $-\omega_0$ is thereby created via (5.2) and becomes dark energy or represents dark matter depending upon whether this energy is >0 or <0.

In a pion, the mass of its quark and antiquark are nearly the same. If the pion coordinate X coincides with the quarks' center of mass, $a_m \approx 1/2$. If it coincides with the center of number of quarks, $a_m = 1/2$. In these cases, (5.2) produces little or no relative energy $-\omega_0$. However, $a_m \neq 1/2$ is allowed; then relative energy will be produced but will also vanish later when these pions decay into leptons or photons.

For a nucleon, the mass of its diquark is about twice that of its quark. Or, equivalently, the number of quarks in its diquark is twice that of its quark. This causes that the center of mass, or of number of quarks, if identified as the nucleon coordinate X, does not lie in the middle between the diquark and the quark but lies closer to the diquark than to the quark. This corresponds to a lower $a_m = 1/3$ which by (5.2) leads to a positive relative energy $-\omega_0 = E_{0d}/6$ which now persists because the proton does decay. Extrapolating this tendency, the dark energy assigned to this positive relative energy $-\omega_0 > 0$ should prevail over the dark matter with negative $-\omega_0 < 0$, in qualitative agreement with data (1.1). The dark energy and dark matter in (1.1) are as old as the nucleons in the universe.

If a nucleon with $a_m < 1/2$ (dark energy) and another nearby one with $a_m > 1/2$ (dark matter) were created simultaneously, the associated dark energy region will tend to expand outwards, leaving behind the associated dark matter region. This also agrees qualitatively with the observed dominance of dark energy in outer regions of the universe.

To reach the large ratios in (1.1), (5.2) yields $a_m \approx -13.4$ for nucleons contributing to the observed dark energy. Such nucleons lie $13.4 \times r$, where r is the diquark-quark distance, from the diquark. For nucleons contributing to the observed dark matter, $a_m \approx 6$. Such nucleons lie $5 \times r$ from the diquark. Both types of nucleons thus lie far away from the both constituents of the nucleon. It is presently unknown why a_m took such values.

By lowering the a_m values further to still larger negative values, greater dark energies can be created. This provides a mechanism for the self regenerating universe ([2] §11.14). By choosing $a_m \to -\infty$ for even a single nucleon created in the early universe, the dark energy of the entire universe can in principle be generated. If $a_m \to -\infty$ were chosen, an infinitely strong "hidden" energy sink can also in principle be created by this single nucleon. If this nucleon happens to be in a black hole, it can perhaps cancel out the infinite mass density in this black hole and make it to behave like an object with finite mass density gravitationally, as has been observed. Here, care is needed because there are different kinds of infinities, as is exemplified in [I, II §7.5.4].

6.2. Nucleons in Motion

In general, nucleons are in motion and $\underline{K} \neq 0$ in §4. The presence of a given direction renders that variable separations in (3.4) as well as the radial equations (4.1) are no longer possible. This problem has thus not been treated in SSI.

If the "hidden" relative energy $-\omega_K \neq 0$ here, it will couple to $\underline{K} \neq 0$. Inserting (3.1-3) together with (5.2), with the subscript 0 replaced by K, into (2.1), leads to a set of equations that replace (4.1). The factors $(K\omega_K)^n$, where $n = 0, 1, 2, 3$, appear in these equations and partially characterize such couplings. Thus, an aggregate of nucleons with different K values will produce a distribution of relative energies $-\omega_K$.

6.3. Relative Time and Energy in Mesons

The associated relative time x^0, also "hidden", can be integrated over to become a large constant $\int dx^0 = \tau_0 \to \infty$ which in the meson case enters [I, II (7.4.6b)] and generates the gauge boson mass M_W, rendering the Higgs boson superfluous.

Relative energies between quark and antiquark in mesons are usually very small. One relative energy between the d and $\bar{s}$ quarks in neutral kaon K^0 has been estimated to be ≈30 eV [II (13.4.6)] in connection with CP violation considerations of the $\bar{K}^0 - K^0$ system. CP violation is commonly considered to be the cause of matter-antimatter asymmetry in the universe ([2] §12.12); it has been exemplified by that in the neutral kaon system ([2] §11.18).

7. Conclusions

The assignment of the dark constituents in the universe to the "hidden" relative energies between the diquark and quark in nucleons puts them to be in contact with a first principles' hadron theory SSI supported by data.

A nucleon with the arbitrary transformation constant a_m in (3.1) chosen to be ≈1/2 behaves like ordinary matter, a nucleon with $a_m << 1/2$ behaves like dark energy and a nucleon with $a_m >> 1/2$ is interpreted to represent dark matter. Why a_m takes on these different values is not known. How these different manifestations of such nucleons are eventually distributed in the universe has also not been investigated presently.

Conflicts of Interest

The author declares no conflicts of interest regarding the publication of this paper.

References

[1] Wikipedia (2019) Dark Energy.

[2] Harwit, M. (2006) Astrophysical Concepts. 4th Edition, Springer, Berlin.

[3] Longair, M.S. (2011) High Energy Astrophysics. 3rd Edition, Cambridge University Press, Cambridge

[4] Hoh, F.C. (2011) Scalar Strong Interaction Hadron Theory. Nova Science Publishers, Hauppauge, Denoted by I.

[5] Hoh, F.C. (2019) Scalar Strong Interaction Hadron Theory. II Nova Science Publishers, Hauppauge, Denoted by II.

[6] Hoh, F.C. (1994) *International Journal of Theoretical Physics*, **33**, 2125. https://doi.org/10.1007/BF00673960

[7] Hoh, F.C. (1993) *International Journal of Theoretical Physics*, **32**, 1111. https://doi.org/10.1007/BF00671793

Journal of Modern Physics, 2019, 10, 641-662
http://www.scirp.org/journal/jmp
ISSN Online: 2153-120X
ISSN Print: 2153-1196

Calculation of the Universal Gravitational Constant, of the Hubble Constant, and of the Average CMB Temperature*

Claude Mercier

Independent Researcher, Baie-Comeau, Canada
Email: claude.mercier@gctda.com

How to cite this paper: Mercier, C. (2019) Calculation of the Universal Gravitational Constant, of the Hubble Constant, and of the Average CMB Temperature. *Journal of Modern Physics*, **10**, 641-662.
https://doi.org/10.4236/jmp.2019.106046

Received: April 30, 2019
Accepted: May 21, 2019
Published: May 24, 2019

Abstract

Dirac made the hypothesis that all large, dimensionless numbers that could be constructed from the important natural units of cosmology and atomic theory were connected [1] [2]. Although Dirac did not succeed in exactly matching all these numbers, he suspected that there was a way to unify all of them. Dirac's hypothesis leads to the N constant which unifies most of physics' parameters. It represents the maximum number of photons with a wavelength equal to the universe circumference. Using a new cosmological model, we found the β constant which represents the ratio between the expansion speed of matter in the universe and the speed of light. With these constants, we can now calculate accurately several physics parameters, including the universal gravitational constant G, the Hubble constant H_0, and the average temperature T of the cosmological microwave background (CMB). Our equations show that G, H_0 and T are not really constant over space and time.

$$G \approx 6.673229809(86)\times 10^{-11}\,\mathrm{m^3\cdot kg^{-1}\cdot s^{-2}},\quad T \approx 2.7367958(16)\,\mathrm{K}$$

$$H_0 \approx 72.09548580(32)\,\mathrm{km\cdot s^{-1}\cdot MParsec^{-1}},\quad N \approx 6.303419702(84)\times 10^{121}$$

Keywords

Gravitational Constant, Hubble, Dirac Large Numbers Hypothesis, CMB/CMBR

1. Introduction

The universal gravitational constant G, the Hubble constant H_0 and the average temperature T of the cosmological microwave background (CMB) of the un-

*Calculation of G, H_0, and T.

iverse suffer from higher uncertainties than most of other constants because, for the moment, they are only measured. The measurement of G is imprecise because of the low intensity of gravitational forces. Even with the best torsion scale, collected data are tainted by errors caused by the influence of masses that circulate in the vicinity (Sun, Moon, Earth, etc.). The H_0 constant is measured using observations of distant galaxies and the results vary according to the method used. With respect to the average temperature of the diffuse background of the T universe, it is difficult to make an accurate and reliable measurement of its value, especially near absolute zero (0 K).

The purpose of this paper is to provide to the modern metrology system new equations that could accurately determine G, H_0, T, and N from other well-defined constants. The value of N represents the maximum number of photons existing in the universe which have the lowest energy possible (with a wavelength equal to the circumference of the universe). These equations may help to discriminate different measurement results and identify the best methods to use. Several measurements are displayed as having incredibly low tolerances but do not overlap with other measurements that display similar tolerances.

We will begin by defining the parameters used in our article while giving their value using CODATA 2014 [3]. Subsequently, in order to find the desired equations, we will show our model of the universe that will, among other things, allow finding the β constant. The value of β represents the ratio between the expansion speed of the material universe and the expansion speed of the luminous universe (which is, for now, the speed of light in vacuum c). This constant is crucial in the subsequent calculations of several physics' constants. A modified version of Dirac's hypothesis on large numbers will be presented in order to establish a link with the fine-structure constant α. Using this link, we will find equations giving the exact values of H_0 and G while explaining why these parameters of the universe are not constant through space and time. What we will end up with is a modified version of the Weinberg equation that will provide a tool to "measure" the Hubble constant H_0 as a function of the universal gravitational constant G. Through this article, several links are made between the infinitely small and the infinitely large.

2. Development

2.1. Values of Physics Parameters

In general, we will use the concise form of notation to display tolerances. For example, typically, 2.736(17) K will mean 2.736 ± 0.017 K.

According to Salvatelli, Hubble constant is $H_0 \approx 72.1^{+3.2}_{-2.3}\ \mathrm{km \cdot s^{-1} \cdot MParsec^{-1}}$ [4]. This value will be used until we get a precise value of H_0 from Equation (44) and Equation (63). It should be noted that 1 MParsec $\approx 3.085677581 \times 10^{22}$ m.

The average temperature of the Cosmic Microwave Background (CMB) has been measured by the Cobra probe at $T \approx 2.736(17)$ K [5]. According to Fixsen, it is $T \approx 2.72548(57)$ K [6].

According to the CODATA 2014 [3], the physics parameters used are:

- Speed of light in vacuum $c \approx 299792458\ \mathrm{m}\cdot\mathrm{s}^{-1}$
- Electric constant in vacuum $\varepsilon_0 \approx 8.854187817\times10^{-12}\ \mathrm{F}\cdot\mathrm{m}^{-1}$
- Magnetic constant in vacuum $m_0 \approx 4\pi\times10^{8}\ \mathrm{N}\cdot\mathrm{A}^{-2}$
- Planck constant $h \approx 6.626070040(81)\times10^{-34}\ \mathrm{J}\cdot\mathrm{s}$
- Planck length $L_p \approx 1.616229(38)\times10^{-35}\ \mathrm{m}$
- Planck time $t_p \approx 5.39116(13)\times10^{-44}\ \mathrm{s}$
- Planck mass $m_p \approx 2.176470(51)\times10^{-8}\ \mathrm{kg}$
- Planck temperature $T_p \approx 1.416808(33)\times10^{35}\ \mathrm{K}$
- Universal gravitational constant $G \approx 6.67408(31)\times10^{-11}\ \mathrm{m}^3\cdot\mathrm{kg}^{-1}\cdot\mathrm{s}^{-2}$
- Electron charge $q_e \approx 1.6021766208(98)\times10^{-19}\ \mathrm{C}$
- Electron mass $m_e \approx 9.10938356(11)\times10^{-31}\ \mathrm{kg}$
- Classical electron radius $r_e \approx 2.8179403227(19)\times10^{-15}\ \mathrm{m}$
- Fine-structure constant $\alpha \approx 7.2973525664(17)\times10^{-3}$
- Boltzmann constant $k_b \approx 1.38064852(79)\times10^{-23}\ \mathrm{J}\cdot\mathrm{K}^{-1}$
- Stephen-Boltzmann constant $\sigma \approx 5.670367(13)\times10^{-8}\ \mathrm{W}\cdot\mathrm{m}^{-2}\cdot\mathrm{K}^{-4}$
- Rydberg constant $R_\infty \approx 10973731.568508(65)\ \mathrm{m}^{-1}$

2.2. Our Model of the Universe

In 1929, Hubble showed that the universe is expanding [7]. In 1931, Lemaître was the first to advance the idea that the universe began with a "primeval-atom" [8] which was later ironically nicknamed by Hoyle "Big Bang" in a BBC broadcast in 1949 [9]. According to our model, the material universe is embedded in a luminous universe, both being spherical and expanding with a speed proportional to their radius. The equations of relativity show that any mass must move at a speed lower than c, otherwise it would have infinite energy [10]. Therefore, the expansion of the material universe is slower than its luminous counterpart which is in expansion at the speed of light (which is c for now). With this model, we will calculate some parameters.

With special relativity, Einstein showed that a gravitational field generated by a mass m slows down light [11]. Erroneous by a factor of 2 compared to what happens in reality, his equation, which was coming from special relativity, is subsequently corrected by Schwarzschild using general relativity [12].

We want to show that the speed of light in vacuum may vary in a gravitational field. In their Appendix A, Equation (A.1), Binney and Merrifield cited an Equation (from Weinberg's 1972 book "Gravitation and Cosmology") which gives the proper time τ for a photon (the same time then if we were traveling on a photon) [13]. We consider this equation as being an excellent approximation (in a context of a weak gravitational field) deduced from general relativity.

$$\tau^2 = \left(c^2 + 2\Phi\right)\mathrm{d}t^2 - \left(1 - 2\Phi/c^2\right)\left(\mathrm{d}x^2 + \mathrm{d}y^2 + \mathrm{d}z^2\right) \quad \text{where } \Phi = \frac{-Gm}{r} \le 0 \qquad (1)$$

The Φ value represents the Newtonian gravitational potential. In a weak gravitational field condition, $|\Phi| \ll c^2$. The gravitational potential Φ is measured at a distance r from the center of mass m. Let dx, dy, dz be the change in

the spatial coordinates of a photon in the element of time dt. For an observer at rest, $\tau = 0$. Let us consider an arbitrary point A in space which has the spatial coordinate (x_1, y_1, z_1). Let us also consider that the center of mass for the mass m is the origin O. We are interested in the gravitational field effect on the refractive index of the vacuum between the point A and O. We want to calculate the speed of light $v_L(r)$ in vacuum for a distance $r = \overline{\mathbf{AO}}$ from the center of mass O. We always have the possibility to make translations and rotations such a way our coordinate system is centered on the point-mass m and that the x axis coincides on the $\overline{\mathbf{AO}}$ line segment. At that time, we can consider that there is no more interaction in other axis. So, dy = 0 and dz = 0. We then simplify Equation (1) to get Equation (2).

$$\left(c^2 + 2\Phi\right)\mathrm{d}t^2 - \left(1 - 2\Phi/c^2\right)\mathrm{d}x^2 = 0 \tag{2}$$

$$v_L\left(r\right) = \frac{\mathrm{d}x}{\mathrm{d}t} = \frac{c}{n_0} \quad \text{where } n_0 = \sqrt{\frac{\left(1 - 2\Phi/c^2\right)}{\left(1 + 2\Phi/c^2\right)}} \approx 1 - 2\Phi/c^2 \tag{3}$$

For a distance r from the center of mass m, the speed of light c is reduced by the refractive index n_0 caused by a gravitational field of potential Φ, which gives a modified speed of light $v_L(r)$. When the gravitational potential $|\Phi| \ll c$ in Equation (3), we can use an approximation for the refractive index n_0. However, we will not use this approximation in our further calculations.

Locally, in space and time, the speed of light seems constant and equal to c. If the universe is expanding and its density is decreasing, the refractive index would also be decreasing, which would imperceptibly accelerate light.

However, the value of c is already the result of another speed limit that we call k (which we do not yet know the value) affected by a local refractive index n. Let us use Equation (3) to build another equation with the same form. We are currently at an arbitrary distance r_u from the center of mass of the universe. Knowing that the apparent mass of the universe is m_u, the speed c is the result of Equation (4).

$$c = \frac{k}{n} \quad \text{where } n = \sqrt{\frac{1 - 2\Theta/k^2}{1 + 2\Theta/k^2}} \quad \text{and} \quad \Theta = \frac{-Gm_u}{r_u} \le 0 \tag{4}$$

The radius of the space [8] [14] (or the radius of the universe [14]), as described by Lemaître, corresponds to what we prefer to call the apparent radius of curvature of the luminous universe R_u. We call its value "apparent" because the equation giving R_u assumes a speed of light that is constant over time and equal to c, for a time equal to the apparent age of the universe $T_u = 1/H_0$. However, in our model, the speed of light is not constant over time. Its value is indeed c in the present moment. However, assuming that the universe is expanding according to Equation (4), its value was necessarily lower than this speed in the past. If we go back far enough in time (when the apparent radius of curvature of the universe was smaller), we even find a moment where the speed of light was zero.

According to Hubble, the constant H_0 represents the speed of movement of

galaxies (in km·s^{-1}·MParsec) [7]. In our opinion, it is equivalent to locally measuring the derivative of the velocity of matter v_m with respect to distance r. According to the equations of relativity, to avoid needing infinite energy, matter is obliged to travel slower than light since the speed of light is a speed limit. Matter moves locally at a rate β times slower than the speed of light c by moving away radially from the center of mass of the universe. Locally, at our location in the universe, the value of H_0 is evaluated at a distance $r = r_u$ (which represents a fraction β of the apparent radius of curvature of the luminous universe R_u).

$$H_0 = \left.\frac{\mathrm{d}v_m}{\mathrm{d}r}\right|_{r=r_u} = \frac{\beta c}{r_u} = \frac{\beta c}{\beta R_u} \Rightarrow R_u = \frac{c}{H_0} \tag{5}$$

We are at a distance r_u from the center of mass of the universe.

$$r_u = \beta R_u = \frac{\beta c}{H_0} \tag{6}$$

Let us find the apparent mass of the universe m_u. Let us also associate a mass m_{ph} with a photon. If we place this photon at the periphery of the luminous universe, at a distance R_u from the center of mass of the universe, it will have an E_g gravitational energy.

$$E_g = \frac{G m_u m_{ph}}{R_u} \tag{7}$$

According to the special relativity, the mass energy associated with this photon is E_m.

$$E_m = m_{ph} c^2 \tag{8}$$

By equating Equation (7) and Equation (8), replacing R_u with Equation (5), and isolating the apparent mass of the universe m_u, we obtain the same equation as that of Carvalho [15].

$$m_u = \frac{c^2}{G \cdot R_u} = \frac{c^3}{G \cdot H_0} \tag{9}$$

For a distance r_u, our local universe parcel travels at speed v_m.

$$v_m = \frac{\beta k}{n} \quad \text{where } n = \sqrt{\frac{1 - 2\Theta/k^2}{1 + 2\Theta/k^2}} \quad \text{and } \Theta = \frac{-G m_u}{r_u} \tag{10}$$

The measurement of H_0 is made by observing the global displacement of galaxies at our location r_u. Each galaxy has its own movement. Due to the expansion of the universe, the galaxies are moving away from each other. The value of the Hubble constant H_0 represents the derivative of the speed of the material universe v_m with respect to the element of distance dr, evaluated at a distance $r = r_u$ from the center of mass of the universe.

$$H_0 = \left.\frac{\mathrm{d}v_m}{\mathrm{d}r}\right|_{r=r_u} = \frac{k\beta y}{r_u}\left(\frac{1}{(1+y)\sqrt{1-y^2}}\right) \quad \text{where } y = \frac{2Gm_u}{k^2 r_u} \tag{11}$$

Solving Equations (4) to (6) and Equation (11) leads to Equations (12) to (16).

$$k = c\sqrt{2+\sqrt{5}} \approx 6.17\times10^{8}\ \mathrm{m/s} \tag{12}$$

$$\beta = 3-\sqrt{5} \approx 0.764 \tag{13}$$

$$R_u \approx 1.28\times10^{26}\ \mathrm{m} \tag{14}$$

$$r_u \approx 9.80\times10^{25}\ \mathrm{m} \tag{15}$$

$$m_u \approx 1.73\times10^{53}\ \mathrm{kg} \tag{16}$$

The k constant represents the asymptotic value for the speed of light in vacuum when the apparent radius of curvature of the universe tends towards infinity. The β constant is geometric and can be defined as the ratio between the speed of expansion of the material universe and the speed of expansion of the luminous universe (which is the speed of light). It can also represent the ratio of the apparent radius of curvature of the material universe r_u (evaluated at our location in the universe with respect to the center of mass of the universe) and the apparent radius R_u of curvature of the light universe. The value of m_u represents the apparent mass of the universe.

We draw the reader's attention to the fact that β constant is unique to our cosmological model, but it is essential for making multiple connections between physics' constants. It allows making several links between the infinitely large and the infinitely small in Dirac's large numbers hypothesis.

2.3. Dirac's Large Number Hypothesis

In this section, we show many equations. In order to condense the information, we ask the reader to refer to the section at the beginning of this article which defines the different parameters of the universe.

By calculating ratios of quantities having the same units, Dirac found that these appeared to result from a few large numbers. Without using all of Dirac's examples, here are some ratios that give the same unitless large number [2].

$$\frac{R_u}{L_p} = \frac{m_u}{m_p} = \frac{m_p}{m_{ph}} = \frac{1}{t_p H_0} \approx 7.94\times10^{60} \tag{17}$$

With similar findings, Dirac figured this was no coincidence. We will see that without β in Equation (13), it is impossible to make certain ratios equal to other large numbers.

Dirac could see that these large numbers were separated into a few distinct orders of magnitude without being able to calculate them precisely. All ratios that we found may, by adding certain factors, come from a single number N. The N value represents the maximum number of photons having the lowest energy (of $2\pi R_u$ wavelength) that may exist in the universe. Here, we assume that we convert the entire mass m_u of the universe in this specific wavelength of photon type. To obtain N, let us calculate the mass m_{ph} associated with the $2\pi R_u$ wavelength photon by making the corpuscular and wave energy of a photon equal in Equation (18).

$$m_{ph}c^2 = \frac{hc}{2\pi R_u} \quad \Rightarrow \quad m_{ph} = \frac{h}{2\pi R_u c} \approx 2.74\times10^{-69}\,\text{kg} \tag{18}$$

$$N = m_u / m_{ph} \approx 6.3\times10^{121} \tag{19}$$

The other "large" numbers are of type N exponent a fractional number, such as $N^{1/2}$, $N^{1/3}$, $N^{1/4}$, …, $N^{1/57}$ or $N^{2/3}$, $N^{3/4}$, etc. It is possible to find more than a hundred equations giving N itself. Here are a few examples (Equations (20) to (27)) which will be calculated from, among others, postulates #1 and #2 cited further. In the following equations, T_p represents the Planck temperature which is about $T_p \approx 1.42 \times 10^{32}$ K. This is the highest temperature that can be reached in the universe when we condensate the apparent mass of the universe m_u in a point-like sphere of radius equal to Planck length L_p. We also think this was the initial temperature of the universe at the Big Bang. The value of q_p is the Planck charge which is about $q_p \approx 1.88 \times 10^{-18}$ C.

$$N^{1/2} = \frac{m_p}{m_{ph}} = \frac{R_u}{L_p} = \frac{1}{t_p H_0} = \frac{2\pi T_p k_b}{hH_0} = \frac{-1}{q_e}\sqrt{\frac{4\pi m_u R_u \alpha}{\mu_0}} \approx 7.94\times10^{60} \tag{20}$$

$$N^{1/3} = \frac{m_u r_e \alpha}{m_e R_u \beta} = \frac{m_e\sqrt{\beta}}{m_{ph}\alpha} = \frac{R_u\sqrt{\beta}}{r_e} = \frac{q_e^2\alpha}{4\pi\varepsilon_0 G\beta m_e^2} \approx 3.98\times10^{40} \tag{21}$$

$$N^{2/3} = \frac{m_u\alpha}{m_e\beta^{1/2}} = \frac{R_u^2\beta}{r_e^2} = \frac{m_p^4\alpha^4}{m_e^4\beta^2} = \frac{m_e^2\beta}{m_{ph}^2\alpha^2} \approx 1.58\times10^{81} \tag{22}$$

$$N^{1/4} = \frac{T_p}{T}\left(\frac{15\beta^4\alpha^2}{\pi^3}\right)^{1/4} = \frac{k_b T}{m_{ph}c^2}\left(\frac{\pi^3}{15\beta^4\alpha^2}\right)^{1/4} \approx 2.82\times10^{30} \tag{23}$$

$$N^{1/6} = \frac{r_e}{L_p\sqrt{\beta}} = \frac{m_p\alpha}{m_e\sqrt{\beta}} = \frac{\alpha^3}{4\pi R_\infty L_p\sqrt{\beta}} = \frac{2\pi r_e k_b T_p}{hc\sqrt{\beta}} \approx 1.99\times10^{20} \tag{24}$$

$$N^{1/16} = \left(\frac{4\pi R_\infty c\sqrt{\beta}}{H_0}\right)^{57/256} = \left(\frac{T_p\beta}{T}\right)^{1/4}\left(\frac{15\alpha^2}{\pi^3}\right)^{1/16} \approx 4.10\times10^{7} \tag{25}$$

$$N^{1/19} = \frac{1}{4\pi R_\infty r_e} = \left(\frac{m_e^2\beta}{m_{ph}^2}\right)^{1/12} = 16\pi^2\beta L_p R_u R_\infty^2\sqrt{\alpha} \approx 2.57\times10^{6} \tag{26}$$

$$N^{1/57} = \frac{q_p^2}{q_e^2} = \left(\frac{m_p^2}{m_e^2\beta}\right)^{1/21} = \left(\frac{q_e^2\beta}{4\pi\varepsilon_0 G m_e^2}\right)^{1/20} = \frac{1}{\alpha} \approx 137 \tag{27}$$

Equation (27) which implies the fine-structure constant α will be used in Equation (48). For rational exponents of small values such as 1/57, we consider the term "large number" is no longer appropriate. Note that our constant β is required in several equations.

2.4. Variations of Physics "Constants" over Time

According to our model, light accelerates over time. In order for the principle of conservation of energy to be maintained, an electromagnetic wavelength equal to $2\pi R_u$ must increase its wavelength over time to allow light to accelerate during

the same period. As the universe is expanding, the mass associated with the photon decreases over time.

The universe expands and its angular velocity of rotation decreases like a skater who extends his arms. The radius R_u is limited by its tangential rotation speed which is that of light. As the universe is expanding, the refractive index of the vacuum decreases and allows a slow acceleration of light over time.

Photons may have different wavelengths. Therefore, they may have different energy and different associated masses. Let's suppose that we convert all the mass m_u of the universe into a huge number N of photons, all having the lowest energy possible. Due to the Plank Equation (see Equation (50) further in this article) used to convert wavelength to energy, these photons are at their lowest energy possible when they will all have the longest wavelength (when $\lambda = 2\pi R_u$, which corresponds to the circumference of the universe). It is impossible to have a dimension bigger than the circumference of the universe, thus confirming these photons cannot have any lower energy. Of course, the apparent radius R_u of the luminous universe is always increasing over time. Therefore, the mass m_{ph} associated to the energy of one of these photons is decreasing over time since the circumference of the universe will increase in the same time frame. However, in percentage, it will be the same for the mass m_u of the universe.

The maximum number N of lowest energy photons is forced to be constant over time since if the mass m_{ph} associated with the lowest energy photons as the denominator of Equation (19) decreases over time, it will be the same, in percentage, for m_u which includes the mass of these photons as the numerator. If N is constant, all other large numbers are also constant. In these unitless numbers, the variations in the numerators are compensated by the same percentage changes in the denominators. All "constants" with units though, must vary over time.

Attention, in metrology, it is very useful to consider constant the speed of light. This makes it possible to "freeze" several parameters of our universe and to determine them more precisely. We have every right to do this and to refer all units of measurement to the speed of light, which varies very little in the course of human life. By doing this, we force the fine-structure constant to look like varying over time (even if it is not the case).

If we are trying to make comparisons, it's like having the right to say that a rocket takes off from the ground or to say that the earth is moving under the rocket. We may feel that we have a choice. However, in fact, only one option represents the reality, otherwise, we face the "twin paradox" that was presented to Einstein by Paul Langevin at the Bologna Congress in 1911 (at that time, it was not yet clearly a paradox). Because of the massive mass of the earth and the principle of conservation of the momentum, we are obliged to say that the physical phenomena will be explained only if we consider that the rocket takes off from the ground (and not the opposite). It's the same with the speed of light. To explain physics phenomena, we are forced to admit that the speed of light increases over time. However, for physicists in metrology, it would be a disaster to

admit such an affirmation since nothing would be really constant anymore, apart from unitless ratios, the fine-structure constant, and the geometrical constants.

By imposing the constancy of c in metrology, certain phenomena become difficult to explain. The expansion of the universe observed by Hubble is incompatible with the "constancy" of c imposed in metrology. If light really accelerates over time and if we continue to say that the speed of the light is constant, that is to say, that the units of distance measure enlarge and that the objects shrink over time. Such considerations may lead some to conclude, erroneously, to the existence of a "Big Crunch". If it is really constant, it is the expansion of the universe that is no longer understandable. Schwarzschild's explanation, with the change in the index of refraction of the vacuum in presence of a mass, would no longer be transposable to the universe as we have done. It would then be necessary to question all calculations made on black holes and gravitational lenses. We cannot believe such an avenue.

Our choice is to see the speed of light accelerating slowly over time. Doing so, all "constants" that have units of measurement vary. Only the unitless constants, such as the fine-structure constant, the unitless ratios and the geometric constants are really constant.

Results will be diametrically opposed if it is taken for granted that the speed of light is constant for metrological purposes or that it changes over time. Both points of view are valid and have their advantages. In this article, it will be considered that the speed of light changes over time.

Einstein's general relativity explains the laws of gravitation by space-time deformations caused by the masses involved [16]. It is however possible to explain the phenomenon of gravitation by a pressure differential caused by a shield effect between different masses located in the vacuum of the universe which is filled with corpuscles transmitting their momentum as described by Fatio [17] and Le Sage [18]. Besides, the Jérôme brothers seem to have succeeded in unifying this concept with Einstein's general relativity [19] (unpublished document). In this scenario, masses would not be attracted, but they would rather be pushed towards one another by invisible corpuscles. According to Sidharth, these corpuscles consist of harmonic oscillators (photons) of different wavelengths [20]. The repeated impacts of photons traveling in all directions in the vacuum of the universe would create a "radiation pressure" (expression used by Mansuripur [21]) or a "thermodynamic radiation pressure" (to refer to the analogous "thermodynamic pressure" term used by Horowitz for gases [22]). Just like in gases where molecules are agitated, the word "thermodynamics" is used to refer to the random stirring of photons. Sidharth considers that the spectrum of these photons' wavelength varies between the Planck length L_p and the circumference of the universe ($2\pi R_u$). To be more precise, we rather think that these wavelengths vary between the circumference of Planck particle ($2\pi L_p$) and the apparent circumference the luminous universe ($2\pi R_u$).

The equations of Einstein's general relativity [16] and Newton's universal gravitation [23] assume that the universal gravitational constant G is constant through universe and through time. But, considering the gravitational force as the result of a radiation pressure, it is possible to conceive that G is constant only for a small parcel of the universe. It's like the water pressure around a fish in the bottom of a lake. The pressure is almost uniform around the fish, but it differs from the surface of the lake. The universe can never end in a "Big Crunch" since the external radiation pressure of it is zero. This pressure deficit generates an irremediable expansion of the universe.

2.5. First Calculation of a More Precise Hubble Constant

According to different sources, H_0 is between 67.8(9) km·s^{-1}·MParsec^{-1} [24] and $77.6^{+4.8}_{-4.3}$ km·s^{-1}·MParsec^{-1} [25]. Uncertainties from different measurement results do not always overlap. For a better precision in calculations that we will do further, we must find a method which will assure us a minimum of unequivocal precision.

As the CMB average temperature T of the universe can be precisely measured, an exploitable link may be made between this parameter and H_0.

According to Alpher, the universe has all properties of a black body [26]. The universe absorbs perfectly all electromagnetic energy, whatever wavelengths it receives. This absorption is converted into thermal agitation which causes the emission of a thermal radiation whose emission spectrum on the surface of the sphere of the luminous universe depends only on its average temperature. The Stefan-Boltzmann law allows us to determine the flux density M° (in W·m^{-2}) as a function of the surface temperature T (in K).

$$M^\circ(T) = \sigma T^4 \tag{28}$$

The Stefan-Boltzmann's constant is defined by σ in the following equation.

$$\sigma = \frac{2\pi^5 k_b^4}{15h^3c^2} \approx 5.67\times10^{-8}\,\mathrm{W\cdot m^{-2}\cdot K^{-4}} \tag{29}$$

The flux density on the surface of the sphere representing the luminous universe may be defined as the total power P_u dissipated in the universe over the total area A_u of the sphere. The dissipated power P_u corresponds to taking the total energy E_u and dividing it by the apparent age of the universe $T_u = 1/H_0$.

$$M^\circ = \frac{P_u}{A_u} = \frac{E_u}{A_u T_u} = \frac{E_u H_0}{A_u} \tag{30}$$

The total energy of a mass m in movement is given by E_t.

$$E_t = mc^2 \tag{31}$$

The apparent mass m_u of the universe described in Equation (9) already represents that of the expanding universe. So, in Equation (31), we replace m by the apparent mass of the universe m_u and the energy E_t by the total amount of energy E_u contained in the universe.

$$E_u = m_u c^2 = \frac{c^5}{GH_0} \tag{32}$$

Using Equations (28) to (30), and Equation (32), we get the value of T which should be the average temperature of the Cosmic Microwave Background (CMB).

$$T = \frac{1}{k_b}\left(\frac{15h^3c^7}{2\pi^5 A_u G}\right)^{1/4} \tag{33}$$

Ludwig Boltzmann expressed the statistical entropy S [27] as a function of the number Ω of microstates defining the equilibrium of a given macroscopic system.

$$S = k_b \ln(\Omega) \tag{34}$$

The expansion of the material universe is β times slower than that of the luminous universe. Entropy is a measure of disorder in the universe and increases with the expansion rhythm. Its measure at R_u would have the value S'.

$$S' = \frac{S}{\beta} = \frac{k_b \ln(\Omega)}{\beta} = k_b' \ln(\Omega) \quad \text{where } k_b' = \frac{k_b}{\beta} \tag{35}$$

The "Boltzmann constant" k_b is true locally in our universe, at our position r_u with respect to the center of mass of the universe. At the periphery of the luminous universe, at $R_u = r_u/\beta$, the "Boltzmann constant" becomes k_b' as given in Equation (35). At the periphery of the luminous universe, Equation (33) becomes Equation (36).

$$T = \frac{1}{k_b'}\left(\frac{15h^3c^7}{2\pi^5 A_u G}\right)^{1/4} = \frac{\beta}{k_b}\left(\frac{15h^3c^7}{2\pi^5 A_u G}\right)^{1/4} \tag{36}$$

Let's find the A_u area of the sphere of the luminous universe when the universe is static.

$$A_u = 4\pi R_u^2 \quad (\text{For static universe}) \tag{37}$$

Applying this assumption to Equation (36), $T \approx 31.9$ K. This is false because with the Cobra probe $T \approx 2.736(17)$ K [5]. It is like if the volume of the static universe were not big enough to dissipate the energy down to the desired value. However, according to Hawking [28] and Fennelly [29], the universe is rotating. Einstein showed that a rotating disk has a larger circumference than a static disk [30]. The circumference becomes "Cir.".

$$\text{Cir.} = 2\pi R_u' = \frac{2\pi R_u}{\sqrt{1-v^2/c^2}} \Rightarrow R_u' = \frac{R_u}{\sqrt{1-v^2/c^2}} \quad (\text{Universe in rotation}) \tag{38}$$

We think that the tangential speed of rotation of the universe is the same as the tangential speed of rotation of the electron on itself. As Llewellyn [31], let us suppose that the spin of the electron is caused by a rotation of the electron on itself.

As it will be shown in Equation (53) and Equation (56), the mass m_e and the charge q_e of the electron are contained within the classical radius r_e of the elec-

tron. The wave energy associated with the electron is, for its part, contained in the Compton radius r_c which is $1/\alpha \approx 137$ times larger than r_e. A wave can be seen in two different ways. From the side, it will look like a sinusoid. But seen from the front, it looks like a circle. As for an electromagnetic wave, the frequency of the wave associated with the electron is calculated by considering that the circumference of the wave circle is traveling at the speed of light.

There seems to be only one way to explain the fact that the mass of the electron is contained in the radius r_e and that its wave energy is contained in the Compton radius r_c. This is because the mass m_e of the electron turns at a relativistic speed such that its Lorentz factor is equal to the fine-structure constant α, which would explain why $r_c = r_e/\alpha$.

$$\alpha = r_e/r_c = \sqrt{1-v^2/c^2} \tag{39}$$

We make the hypothesis that the tangential velocity v of the luminous universe periphery is the same as that of the electron.

$$v = c\sqrt{(1-\alpha)(1+\alpha)} \approx 0.999973c \tag{40}$$

This speed is close to that of light. For an observer located at the center of rotation, the time that elapses in the periphery of the luminous universe is dilated and the distances are compressed by the Lorentz factor. Equation (38) becomes Equation (41).

$$R_u' = R_u/\alpha \quad (\text{Universe in rotation}) \tag{41}$$

The area of the outer surface of the sphere of our universe from Equation (37) becomes equal to Equation (42).

$$A_u = 4\pi R_u^2/\alpha^2 \quad (\text{Universe in rotation}) \tag{42}$$

with Equation (5) and Equation (42), we modify Equation (36) to obtain Equation (43) which should give the average cosmological microwave background (CMB) temperature T.

$$T = \frac{\beta}{k_b}\left(\frac{15\alpha^2 h^3 c^5 H_0^2}{8\pi^6 G}\right)^{1/4} \tag{43}$$

By varying H_0 between 67.8 and 77.6 km·s^{-1}·MParsec^{-1} of the Planck [24] and Chandra [25] probes respectively, we obtain a value of T between 2.65 K and 2.84 K. Data from Cobra (2.736(17) K [5]) and WMAP (2.72548(57) K [6]) probes confirm these results with a lower uncertainty than that currently weighing on H_0.

Let Equation (43) being equal to Fixsen's T and isolating H_0 to calculate its value.

$$H_0(T) = \frac{\pi^3 T^2 k_b^2}{\beta^2 \alpha}\sqrt{\frac{8G}{15c^5 h^3}} \approx 71.505(30)\ \text{km}\cdot\text{s}^{-1}\cdot\text{MParsec}^{-1} \tag{44}$$

Equation (44) agrees with Salvatelli who gets $H_0 \approx 72.1^{+3.2}_{-2.3}$ km·s^{-1}·MParsec^{-1} [4]. It is almost the average result between that of the Planck and Chandra probes.

2.6. Hypothesis Leading to an Exact Calculation of the Universal Gravitational and Hubble Constants

We assume that the α constant can be used as a scale factor. Applied a certain number of times, this factor can be related to some unitless ratios involving physics constants.

$$m_u = m_{ph} / \alpha^n \tag{45}$$

Let us start by incorporating Equation (5), Equation (18), Equation (44) and Equation (45) into Equation (19) in order to find N and then n. The accuracy of $N(T, G)$ will especially depend on the temperature T that will be used in Equation (46) and on the universal gravitational constant G. Any little change in other parameters (within the tolerances mentioned in the CODATA) of Equation (46) will not have any impact on the result value since T and G are much less accurate than the others that are used in this equation. Let's take $T \approx 2.72548(57)$ K from Fixsen coming from the Wilkinson Microwave Anisotropic Probe (WMAP) [6]) and $G \approx 6.67408(31) \times 10^{-11} \mathrm{m}^3 \cdot \mathrm{kg}^{-1} \cdot \mathrm{s}^{-2}$ from the CODATA 2014 [3].

$$N(T,G) = \frac{1}{\alpha^n} = \frac{m_u}{m_{ph}} = \frac{15\alpha^2\beta^2h^2c^{10}}{4\pi^5T^4k_b^4G^2} \approx 6.4071(54) \times 10^{121} \tag{46}$$

Let us define $[x]$ as being the rounded integer value of x.

$$n = \left[-\log(N)/\log(\alpha)\right] = \left[57.00332(17)\right] = 57 \tag{47}$$

For now, this result cannot be demonstrated, we must create the postulate #1.

$$\text{POSTULATE \#1:} \quad N = 1/\alpha^{57} \approx 6.303419702(84) \times 10^{121} \tag{48}$$

2.7. Calculation of the Universal Gravitational Constant

To calculate G, we need an equation giving exactly the value N obtained by Equation (48) as a function of G, but independent of H_0 and T that we do not know with sufficient precision (compared to other physics constants from CODATA).

The most frequent opportunities to see the constant G intervene in physics equations are found in the calculations of gravitational energy and gravitational force. Let us start by evaluating, on Earth, the gravitational energy E_g that there is between two electrons separated by a distance equal to the classical radius r_e of the electron.

$$E_g = \frac{Gm_e^2}{r_e} \tag{49}$$

The energy of an electromagnetic wave of wavelength λ is given by Equation (50).

$$E = \frac{hc}{\lambda} \tag{50}$$

Even in a context where the speed of light increases over time, the principle of

conservation of energy must be respected. For this reason, the photons that are on the periphery of the luminous universe continue to see their wavelength increase over time to gradually adapt to the new diameter of the universe. The same goes for all other lengths in the universe. We do not realize this because all the other physics constants change at the same time (except unitless ratios, the fine-structure constant and the geometric constants).

Let us bring the experiment made with the two electrons to the periphery of the luminous universe. By doing this, the classical radius of the electron will increase by a factor β and become r_e' (just as for the apparent radius of curvature of the universe).

$$r_e' = \frac{r_e}{\beta} \tag{51}$$

The gravitational energy of Equation (49) is now given by Equation (52).

$$E_g' = \frac{Gm_e^2}{r_e'} = \frac{Gm_e^2\beta}{r_e} \tag{52}$$

On the other hand, the electrical energy E_e remains the same whether measured here on Earth or at the outskirts of the universe. This equation is independent of the radius (although it seems to depend on it at first). Let us analyze the equation of E_e on Earth.

$$E_e = \frac{q_e^2}{4\pi\varepsilon_0 r_e} \tag{53}$$

The charge q_e of an electron is obtained by Equation (54).

$$q_e = -\sqrt{\frac{4\pi m_e r_e}{\mu_0}} \tag{54}$$

The speed of light c is related to ε_0 and μ_0 by Equation (55).

$$c = 1/\sqrt{\varepsilon_0\mu_0} \tag{55}$$

If we use Equation (54) and Equation (55) in Equation (53), we obtain Equation (56).

$$E_e = m_e c^2 \tag{56}$$

Equation (53) and Equation (56) show that the energy contained in the mass of an electron is equivalent to the electrical energy contained between two electrons spaced with a distance equivalent to the classical radius of the electron r_e. In Equation (56), it can be seen that the electric energy E_e is independent of the classical radius of an electron. Therefore, if we reproduce this experience on the periphery of the luminous universe, the electric energy E_g' that we will have will be equal to the energy E_e that we had on Earth. Let us then make the connection between the electric energy E_e' and the gravitational energy E_g' at the periphery of the luminous universe. Bringing the experiment to the periphery of the luminous universe allows seeing why a β factor is introduced into the equation.

$$\frac{E'_e}{E'_g} = \frac{m_e c^2 r_e}{G m_e^2 \beta} = \frac{c^2 r_e}{G m_e \beta} \approx 5.45 \times 10^{42} \tag{57}$$

As in Equation (48), we found that the fine-structure constant α plays a role in determining orders of magnitude. By an adjustment of the exponent of the fine-structure constant α, we obtain a result identical to that of Equation (57).

$$\frac{1}{\alpha^{20}} \approx 5.45 \times 10^{42} \tag{58}$$

We conclude that Equation (57) and Equation (58) are equal. By isolating the universal gravitational constant G, we obtain an equation that we elevate to the rank of postulate #2. It is an equation that cannot be deduced from any other known equation of current physics.

$$\text{POSTULATE \#2:} \quad G = \frac{c^2 r_e \alpha^{20}}{m_e \beta} \approx 6.673229809(86) \times 10^{-11} \text{m}^3 \cdot \text{kg}^{-1} \cdot \text{s}^{-2} \tag{59}$$

This result is in perfect agreement with the Taylor-Parker-Langenberg value which is $G \approx 6.6732(31) \times 10^{-11} \text{m}^3 \cdot \text{kg}^{-1} \cdot \text{s}^{-2}$ [32]. However, based on Equation (59), it can be seen that the tolerance of the measured value of G from CODATA 2014 [3] is underestimated by a factor of about 2.74. Qing [33] has shown that the tolerances of several recent measurements of G do not overlap with each other. Despite the very optimistic accuracy displayed for the various measures, the value of G lies between 6.672 to 6.676 × 10^{-11} $\text{m}^3 \cdot \text{kg}^{-1} \cdot \text{s}^{-2}$. The tolerance displayed in Equation (59) was calculated from the tolerances displayed for the other constants of CODATA 2014. When measuring the universal gravitational constant G, it is easy to underestimate some sources of errors, which can explain this difference. Equation (59) relies on more precise and reproducible constants.

By using different combinations of equations, shown in this article, we can deduce other equations which also give the universal gravitational constant G precisely. We will enumerate them without making any demonstration.

$$G = \frac{q_e^2 r_e R_\infty \alpha^{17}}{\varepsilon_0 m_e^2 \beta} = \frac{2\pi c^3 r_e^2 \alpha^{19}}{h\beta} = \frac{q_e^2 \alpha^{20}}{4\pi\varepsilon_0 m_e^2 \beta} = \frac{hc\alpha^{21}}{2\pi m_e^2 \beta} = \frac{c^2 \alpha^{23}}{4\pi R_\infty m_e \beta} \tag{60}$$

2.8. Improvement of the Hubble Constant and of the Average CMB Temperature

Now that we can precisely calculate N and G, we can equate Equation (19) with Equation (48) using Equation (9), Equation (18) and Equation (59).

$$N = \frac{m_u}{m_{ph}} = \frac{2\pi c^5}{hGH_0^2} = \frac{2\pi\beta m_e c^3}{h r_e H_0^2 \alpha^{20}} = \frac{1}{\alpha^{57}} \tag{61}$$

Let's associate the energy of the mass m_e of an electron with the wave energy.

$$m_e c^2 = \frac{hc\alpha}{2\pi r_e} \tag{62}$$

With Equation (62), we modify Equation (61) to obtain Equation (63).

$$H_0 = \frac{c\alpha^{19}\sqrt{\beta}}{r_e} \approx 72.09548580(32)\ \mathrm{km\cdot s^{-1}\cdot MParsec^{-1}} \tag{63}$$

The result of Equation (63) is similar to Equation (44) with Fixsen and confirms Salvatelli's value of $H_0 \approx 72.1^{+3.2}_{-2.3}\ \mathrm{km\cdot s^{-1}\cdot MParsec^{-1}}$. Thanks to various equations in this article, we can deduce new equations which will calculate H_0 precisely. We will enumerate them without making any demonstration.

$$H_0 = 4\pi c R_\infty \alpha^{16}\sqrt{\beta} = \frac{4\pi m_e c\alpha^{19}\sqrt{\beta}}{q_e^2\mu_0} = \frac{2\pi m_e c^2\alpha^{18}\sqrt{\beta}}{h} \tag{64}$$

Equating Equation (44) and Equation (63), and using Equation (62), we obtain T which is the average CMB temperature.

$$T = \frac{m_e c^2}{k_b}\left(\frac{15\beta^6\alpha^{17}}{\pi^3}\right)^{1/4} \approx 2.7367958(16)\ \mathrm{K} \tag{65}$$

2.9. Weinberg's Formula

Weinberg found an empirical equation for a typical mass m of a pion-like particle (see page 619 in the Weinberg's 1972 book available in reference [34]). This equation has also been cited by Sidharth in reference [20]. However, the result of this equation does not precisely correspond to any known value. Therefore, we think it is incomplete. It is like if a multiplying factor is missing. In the following equation, $\hbar = h/2\pi$.

$$m \approx \left(\frac{H_0\hbar^2}{Gc}\right)^{1/3} \approx 1\times 10^{-28}\,\mathrm{kg} \tag{66}$$

Let us show that the precise values of α, β, G and H_0 result in the mass m_e of an electron from a modified version of Weinberg's Equation (66). Let us multiply Equation (63) by 1 (in parenthesis, let us multiply by G and divide by Equation (59)).

$$H_0 = \frac{c\alpha^{19}\sqrt{\beta}}{r_e}\left(\frac{Gm_e\beta}{c^2 r_e\alpha^{20}}\right) = \frac{Gm_e\beta^{3/2}}{cr_e^2\alpha} \tag{67}$$

Isolating m_e, we obtain Equation (68).

$$m_e = \frac{cH_0 r_e^2\alpha}{\beta^{3/2}G} \tag{68}$$

The energy contained in the mass m_e of an electron at rest is equal to the wave energy for the Compton wavelength λ_c of the electron.

$$m_e c^2 = \frac{hc}{\lambda_c} \text{ where } \lambda_c = \frac{2\pi r_e}{\alpha} \quad \Rightarrow \quad m_e c^2 = \frac{hc\alpha}{2\pi r_e} \tag{69}$$

$$r_e^2 = \frac{\hbar^2\alpha^2}{m_e^2 c^2} \tag{70}$$

Introducing the result of Equation (70) in Equation (68), we obtain the electron mass m_e as a function of G and H_0. Of course, we get the same value than

the CODATA (except the tolerance), but this equation should not be considered as a way to get the mass of the electron since our values of G and H_0 come someway from this equation. However, as we will see, Equation (71) may be useful for other purposes.

$$m_e\left(G,H_0\right)=\frac{\alpha}{\sqrt{\beta}}\left(\frac{H_0\hbar^2}{Gc}\right)^{1/3}\approx 9.109383559(85)\times 10^{-31}\,\mathrm{kg} \tag{71}$$

The apparent age of the universe is $1/H_0$ and Equation (71) is a function of H_0. As a result, the mass m_e of the electron varies with time. Since this is the case for m_e, it is also the case of other particles and for the apparent mass of the universe m_u. Without doing it here, it can be shown that this is the case for all other "constants" with units.

Equation (71), which is a modified version of the Weinberg formula, could be used to determine and calculate the Hubble constant H_0 as a function of the universal gravitational constant G because all other constants of the equation are precisely known.

$$H_0\left(G\right)=\frac{Gcm_e^3\beta^{3/2}}{\hbar^2\alpha^3}\approx 72.104(33)\,\mathrm{km\cdot s^{-1}\cdot MParsec} \tag{72}$$

Using the value of $G\approx 6.67408(31)\times 10^{-11}\,\mathrm{m^3\cdot kg^{-1}\cdot s^{-2}}$ from CODATA 2014 [3] in Equation (72) we obtain a measured value of H_0 which is similar to the result of Equation (63). This value of H_0 corresponds to an apparent age of the universe of 13.56(6) billion years. Our H_0 value from Equation (63) gives also about 13.56 billion years.

3. Conclusions

This article seems to be very useful from a metrological point of view since it makes it possible to precisely determine several constants which were, until now, only measured. The equations found make it possible to discriminate the results of several research studies on the Hubble constant, on the universal gravitational constant and on the average CMB temperature.

A new model of the universe that uses the β constant has been introduced. This constant represents the ratio between the expansion speed of the material universe and the expansion speed of the luminous universe which is the speed of light. This constant seems to let us believe that the universe is geometric in a certain way. It may be found that β constant is essential in the evaluation of several parameters of the universe (see Equation (59), Equation (63), Equation (65), Equation (71), and many others). We have also seen this by using it to modify the Dirac hypothesis on large numbers because it allows making several links that would not be possible without it. This hypothesis allows making an important link with the fine-structure constant α. Using this link, we derived equations giving the exact values of H_0, G and T. Knowing where these parameters come from, we can explain why these parameters of the universe are not constant across space and the time.

We used a modified version of Weinberg's equation which undoubtedly shows that there is a link between the electron mass, the Hubble constant H_0 and the universal gravitational constant G. This link gives, for the first time, a precise tool to measure the Hubble constant here on Earth, without having to use star observations.

We determined that only unitless parameters are constant. To have a precise metrology system, the International Bureau of Weights and Measures (BIPM) makes the choice to impose the constancy of c. This relevant choice makes it possible to increase the precision of the other physics parameters by becoming really constant. Unitless constants, such as α, will appear to vary over time and some phenomena will become difficult to explain. To consider or not c as constant seems incompatible without really being so. One must be aware of the choice of hypotheses that are being made in the theoretical analyses of scientific documents. It is important to define the chosen choices from the beginning.

One must be aware of the choice being made in theoretical analyzes. The chosen choices must be defined right at the beginning.

By using the equations of G and H_0 shown in this article, it will probably be possible to determine more precisely the movement speeds of the different galaxies, their masses and several other parameters of the universe. By using the equation giving N in the modified hypothesis of large numbers of Dirac, it will probably be possible to establish close links between several physics' constants, which will make it possible to determine new equations that were previously unknown to us.

Conflicts of Interest

The author declares no conflicts of interest regarding the publication of this paper.

References

[1] Dirac, P.A.M. (1938) *Proceedings of the Royal Society of London A*: *Mathematical, Physical and Engineering Sciences*, **165**, 199-208. https://doi.org/10.1098/rspa.1938.0053

[2] Dirac, P.A.M. (1974) *Proceedings of the Royal Society of London A*: *Mathematical, Physical and Engineering Sciences*, **338**, 439-446. https://doi.org/10.1098/rspa.1974.0095

[3] Mohr, P.J., Newell, D.B. and Taylor, B.N. (2016) *Journal of Physical and Chemical Reference Data*, **45**, Article ID: 043102. https://doi.org/10.1063/1.4954402

[4] Salvatelli, V., Andrea, M., Laura, L.-H. and Olga, M. (2013) *Physical Review D*, **88**, Article ID: 023531. https://doi.org/10.1103/PhysRevD.88.023531

[5] Gush, H.P. (1981) *Physical Review Letters*, **47**, 745-748. https://doi.org/10.1103/PhysRevLett.47.745

[6] Fixsen, D.J. (2009) *The Astrophysical Journal Supplement Series*, **707**, 916-920. https://doi.org/10.1088/0004-637X/707/2/916

[7] Hubble, E. (1929) *PNAS*, **15**, 168-173. https://doi.org/10.1073/pnas.15.3.168

[8] Kragh, H. (2012) *Astrophysics and Space Science Library*, **395**, 23-38. https://doi.org/10.1007/978-3-642-32254-9_3

[9] Kragh, H. (2013) *Astronomy & Geophysics*, **54**, 28-30. https://doi.org/10.1093/astrogeo/att035

[10] Einstein, A. (1905) *Annalen der Physik*, **322**, 891-921. https://doi.org/10.1002/andp.19053221004

[11] Einstein, A. (1911) *Annalen der Physik*, **35**, 898-908. https://doi.org/10.1002/andp.19113401005

[12] Grøn, Ø. (2016) *American Journal of Physics*, **84**, 537. https://doi.org/10.1119/1.4944031

[13] Binney, J. and Merrifield, M. (1998) Galactic Astronomy. Princeton University Press, Princeton, 816. https://press.princeton.edu/titles/6358.html

[14] Lemaître, G. (2013) *General Relativity and Gravitation*, **45**, 1635-1646. https://doi.org/10.1007/s10714-013-1548-3

[15] Carvalho, J.C. (1995) *International Journal of Theoretical Physics*, **34**, 2507-2509. https://doi.org/10.1007/BF00670782

[16] Einstein, A. (1916) *Annalen der Physik*, **49**, 769-822. https://doi.org/10.4324/9780203198711

[17] Fatio de Duillier, N. (1949) *Royal Society of London*, **6**, 125-160. https://doi.org/10.1098/rsnr.1949.0018

[18] Rolinson, J.S. (2003) *Notes and Records of the Royal Society of London*, **57**, 35-45. https://doi.org/10.1098/rsnr.2003.0195

[19] Jérôme, J. and Jérôme, F. (2012) New Version of General Relativity that Unifies Mass and Gravity in a Common 4D Higgs Compatible Theory. https://www.researchgate.net/publication/279291155_New_Version_of_General_Relativity_that_Unifies_Mass_and_Gravity_in_a_Common_4D_Higgs_Compatible_Theory

[20] Sidharth, B.G. (2008) The Thermodynamic Universe. Cornell University, International Institute of Applicable Mathematics & Information Sciences, World Scientific, Hackensack, 304. https://doi.org/10.1142/6815

[21] Mansuripur, M. and Pin, H. (2017) Thermodynamics of Radiation Pressure and Photon Momentum. *Optical Trapping and Optical Micromanipulation*, Vol. 14, San Diego, 6-10 August 2017, 20. https://doi.org/10.1117/12.2274589

[22] Horowitz, J. (1950) *Journal de Physique et Le Radium*, **11**, 241. https://doi.org/10.1051/jphysrad:01950001105024100

[23] Newton, I. (1686) Philosophiae Naturalis Principia Mathematica. S. Pepys, Reg. Soc. Praeses, London, 510. https://doi.org/10.5479/sil.52126.39088015628399

[24] Ade, P.A.R., *et al.* (2016) *Astronomy & Astrophysics*, **594**, A13. https://doi.org/10.1051/0004-6361/201525830

[25] Bonamente, M., Joy, M.K., La Roque, S.J. and Carlstrom, J.E. (2005) *The Astrophysical Journal*, **647**, 25-54. https://doi.org/10.1086/505291

[26] Alpher, R.A. and Herman, R.C. (1948) *Nature*, **162**, 774-775. https://doi.org/10.1038/162774b0

[27] Sharp, K. and Matschinsky, F. (2015) Translation of Ludwig Boltzmann's Paper "On the Relationship between the Second Fundamental Theorem of the Mechanical Theory of Heat and Probability Calculations Regarding the Conditions for Thermal Equilibrium" Sitzungberichte der Kaiserlichen Akademie der Wissenschaften. Mathematisch-Naturwissen Classe. Abt. II, LXXVI 1877, pp 373-435 (Wien. Ber. 1877,

76:373-435). Reprinted in Wiss. Abhandlungen, Vol. II, Reprint 42, p. 164-223, Barth, Leipzig, 1909. *Entropy*, **17**, 1971-2009. https://doi.org/10.1142/9781848162938_0002

[28] Hawking, S. (1969) *Monthly Notices of the Royal Astronomical Society*, **142**, 129-141. https://doi.org/10.1093/mnras/142.2.129

[29] Fennelly, A.J. (1976) *The Astrophysical Journal*, **207**, 693-699. https://doi.org/10.1086/154537

[30] Einstein, A. (1912) *Annalen der Physik*, **347**, 355-369. https://doi.org/10.1002/andp.19123430704

[31] Llewellyn, T. (1926) *Nature*, **117**, 514. https://doi.org/10.1038/117514a0

[32] Taylor, B.N., Parker, W.H. and Langenberg, D.N. (1969) *Reviews of Modern Physics*, **41**, 375-496. https://doi.org/10.1103/RevModPhys.41.375

[33] Qing, L., *et al.* (2018) *Nature*, **560**, 582-588. https://doi.org/10.1038/s41586-018-0431-5

[34] Weinberg, S. (1972) Gravitation and Cosmology: Principles and Applications of the General Theory of Relativity. John Wiley & Sons, New York, 685. https://archive.org/details/WeinbergS.GravitationAndCosmology..PrinciplesAndApplicationsOfTheGeneralTheoryOf

Appendix A: Solving of the System of Equations

In this appendix, we will focus on detailing calculations that made it possible to solve a system of 5 unknowns with 5 equations. We will use Equation (59) to evaluate the universal gravitational constant G and Equation (63) to evaluate the Hubble constant H_0.

Let us start by rewriting Equation (4) in another form that will be more practical and list the other starting equations.

$$c = \frac{k}{n} \text{ where } n = \sqrt{\frac{1+y}{1-y}} \text{ and } y = \frac{2Gm_u}{r_u} \tag{73}$$

$$R_u = \frac{c}{H_0} \tag{74}$$

$$r_u = \frac{\beta c}{H_0} = \beta R_u \tag{75}$$

$$m_u = \frac{c^3}{GH_0} \tag{76}$$

$$H_0 = \left.\frac{\mathrm{d}v_m}{\mathrm{d}r}\right|_{r=r_u} = \frac{\beta k y}{r_u}\left(\frac{1}{(1+y)\sqrt{1-y^2}}\right) \text{ where } y = \frac{2Gm_u}{k^2 r_u} \tag{77}$$

In these equations, the unknown values are: R_u, r_u, m_u, β and k. It is a system of 5 equations with 5 unknowns that can be solved mathematically.

In Equation (73), we isolate the value of k and obtain Equation (78).

$$k = c\sqrt{\frac{1+y}{1-y}} \tag{78}$$

In Equation (77), we also isolate the value of k to obtain Equation (79).

$$k = \frac{H_0 r_u}{y\beta}(1+y)\sqrt{1-y^2} \tag{79}$$

Let us equate Equation (78) and Equation (79) to obtain Equation (80).

$$c\sqrt{\frac{1+y}{1-y}} = \frac{H_0 r_u}{y\beta}(1+y)\sqrt{1-y^2} \tag{80}$$

Let us use Equation (74) and Equation (75) in Equation (80) and simplify to get Equation (81).

$$y^2 + y - 1 = 0 \quad \Rightarrow \quad y = \frac{-1 \pm \sqrt{5}}{2} \tag{81}$$

All y parameters in Equation (73) are strictly positive. Therefore, y is positive.

$$y = \frac{\sqrt{5}-1}{2} \tag{82}$$

Putting the result of (82) in Equation (73), we obtain Equation (83).

$$k = c\sqrt{2+\sqrt{5}} \tag{83}$$

In Equation (77), substitute the value of y for the parenthesis by its algebraic

value.

$$H_0 = \frac{2Gm_u\beta}{kr_u^2}\left(\frac{1}{(1+y)\sqrt{1-y^2}}\right) \tag{84}$$

In Equation (84), replace the value of m_u with Equation (76).

$$H_0 = \frac{2c^3\beta}{kr_u^2 H_0}\left(\frac{1}{(1+y)\sqrt{1-y^2}}\right) \tag{85}$$

In Equation (85), we use Equation (75) and Equation (83), then we isolate β.

$$\beta = \frac{2}{\sqrt{2+\sqrt{5}}}\left(\frac{1}{(1+y)\sqrt{1-y^2}}\right) \tag{86}$$

In Equation (86), let us replace y by Equation (82) with the β value. Then, let us list the other results from our system of equations of and let us evaluate their value.

$$\beta = 3-\sqrt{5} \approx 0.764 \tag{87}$$

$$k = c\sqrt{2+\sqrt{5}} \approx 2c \approx 6\times 10^8 \,\mathrm{m}\cdot\mathrm{s}^{-1} \tag{88}$$

$$m_u \approx 1.8\times 10^{53}\,\mathrm{kg} \tag{89}$$

$$R_u \approx 1.28\times 10^{26}\,\mathrm{m} \tag{90}$$

$$r_u \approx 0.98\times 10^{26}\,\mathrm{m} \tag{91}$$

Let us note that β is related to the golden number which is $\varphi \approx 1.618...$

$$\beta = 4-2\varphi \quad \text{where } \varphi = \frac{1+\sqrt{5}}{2} \tag{92}$$

Journal of Modern Physics, 2019, 10, 663-672
http://www.scirp.org/journal/jmp
ISSN Online: 2153-120X
ISSN Print: 2153-1196

New Deduced Results in Subatomic Physics

Bo Lehnert

Alfvén Laboratory, Royal Institute of Technology, Stockholm, Sweden
Email: bo.lehnert@ee.kth.se

How to cite this paper: Lehnert, B. (2019) New Deduced Results in Subatomic Physics. *Journal of Modern Physics*, **10**, 663-672.

https://doi.org/10.4236/jmp.2019.106047

Received: April 2, 2019
Accepted: May 24, 2019
Published: May 27, 2019

Abstract

The Standard Model of elementary particles, with its associated concept of a vacuum state of empty space, leads to strongly restricted results in subatomic physics. Examples are given by vanishing rest masses and an associated spinless state of the photon. In a revised quantum electrodynamic theory by the author, new results have been deduced which cannot be obtained from the Standard Model. These are due to a vacuum state populated by Zero Point Energy and a corresponding nonzero electric charge density. This leads to a screw-shaped photon configuration with rest mass, spin and possibilities of needle radiation, to a deduced value of the elementary charge of the electron, muon and tauon being close to its experimental value, to a deduced mass being nearly equal to 125 GeV of the Higgs particle detected at CERN, and to the discovery of large intrinsic charges of both polarities within the volume of a particle. In their turn, these charges give rise to effects of the same magnitude as that of the strong force, and can account for the binding energy of 8 MeV of the neutron and proton. This makes a unification possible of electrodynamics with the strong nuclear force.

Keywords

Quantum Electrodynamics, Standard Model and Beyond, Zero Point Energy, Higgs Particle, Unification of Electrodynamics and the Strong Force

1. Introduction

The fundamental properties of elementary particles have earlier been discussed by the author in terms of subatomic physics, as given by a revised quantum electrodynamic theory [1,2]. These properties will here be reconsidered with special emphasis on the concepts of rest mass, spin, elementary electric charge, intrinsic electric charges, needle radiation, the strong force, the binding energy of neutrons and protons, the Higgs mass, and the relation between relativity and quantum mechanics.

The shortcomings of conventional theory, based on a vacuum state

of empty space, will first be elucidated in Section 2. This is followed in Section 3 by a description of the revised subatomic field equations of a vacuum state populated by Zero Point Energy (ZPE). In its turn, this leads to new subatomic properties of the elementary particles, as being discussed in Section 4.

2. Shortcomings of Conventional Theory

In conventional electromagnetic theory and such applications as plasma physics, particles of *given* electric charge and mass form the basis of corresponding macroscopic field equations. The latter are then related to a vacuum state of empty space. This theory is well established and will not be further discussed here.

A different situation arises, however, when attempts are made to treat the *interior* of elementary particles in terms of subatomic theory. In this section some important examples are given on what happens if the vacuum concept of empty space is being retained. It implies that the electric charge density represented by the local value $\mathrm{div}\,\mathbf{E}$ of the electric field strength $\mathbf{E}$ *vanishes* identically.

The first example concerns the conventional equations being applied to a model of the propagating photon, treated with $\mathrm{div}\,\mathbf{E} = 0$ by means of the Hertz vector, as given by Stratton [3]. According to Chapter 9 of [1], these equations have solutions in plane, cylindrical, and spherical geometry which all lead to a vanishing total angular momentum (spin). In particular for cylindrical geometry the local spin contributions s_{z1} and s_{z2} of the TM and TE wave types become

$$s_{z1} = s_{z2} \propto K^2 n \left[J_n(Kr)\right]^2 (\sin 2n\varphi) \tag{1}$$

where

$$K^2 = (\omega/c)^2 - k^2 \tag{2}$$

for a wave form $f(r)\exp[i(-\omega t + kz + n\varphi)]$ in a cylindrical frame (r, φ, z) with $J_n(Kr)$ as a Bessel function. The total integrated contribution to the spin then vanishes for all K and n. Consequently, conventional theory does not become reconcilable with a physically relevant photon model which should possess spin according to experiments.

The second example concerns the steady state with both $\mathrm{div}\,\mathbf{E} = 0$ and $\partial/\partial t = 0$. Then the charge density $\varepsilon_0 \mathrm{div}\,\mathbf{E}$ and $\mathrm{curl}\,\mathbf{B}$ of the magnetic field $\mathbf{B}$ will vanish. This implies that there are no local sources of the electromagnetic field. As also being pointed out in Section 6.1 of [1], this is in agreement with Quigg [4] who states that the symmetry of the conventional field equations does not permit masses for quarks and leptons. Consequently, the existence of particle-like states rests on a nonzero $\mathrm{div}\,\mathbf{E}$ and an associated broken symmetry between $\mathbf{E}$ and $\mathbf{B}$.

A third point concerns the conventional description of the photon in terms of plane waves. This is not only in contradiction with a nonzero spin, but also with the experimentally proved needle-like behavior, as described in Chapter 4.1 of [1]. Both these circumstances influence the way in which the concept of special relativity has to be transferred from a plane-wave model to a multidimensional model, such as that of cylindrical geometry later treated in this paper. Needless to say, this does not affect the general lines of thought of special relativity by Einstein.

3. Revised Subatomic Field Equations

The shortcomings of conventional theory impose restrictions on a treatment of subatomic physics. A way out of this dilemma is provided by the following sections. The present treatment thus includes terms with a nonzero div **E** which are not present in a conventional analysis, and where div **E** acts somewhat like a hidden variable.

3.1. The Zero Point Energy

In a study of the quantum mechanical energy levels of the harmonic oscillator, M. Planck found that there is a nonzero ground level, the Zero Point Energy (ZPE), as further described in a review by Schiff [5]. The related electromagnetic vacuum fluctuations were investigated by Casimir [6] who predicted that two metal plates separated by a small spacing will attract each other, due to the fact that only small wavelengths can exist within the spacing. Such a net differential force was first demonstrated experimentally by Lamoreaux [7]. Part of the fluctuations also carry electric charge, as pointed out by Abbott [8]. Consequently, the vacuum is not merely a state of empty space, but includes photon-like modes being each of frequency ν and energy $h\nu/2$ and which result in a real macroscopic pressure. Even if these fluctuations occur at the lowest ZPE level, their spatial inhomogeneity can produce a pressure gradient. Since the Casimir force is due to a comparatively small differential pressure, the total ZPE can become much larger. More detailed discussions are presented elsewhere [9–11].

The basis of the present subatomic field equations is thus formed by the concepts of ZPE and the Casimir force, in combination with special relativity.

3.2. The Extended Equations

With the basic concepts of the previous subsection, a revised quantum electrodynamic theory (RQED) is now established [1]. Thereby the new inclusion of terms with a nonzero div **E** becomes sources of electric charge and matter, in accordance with the incorporated effects of the ZPE. It thus leads to a four-dimensional representation

$$\Box A_\mu = \left(\frac{1}{c^2} \frac{\partial^2}{\partial t^2} - \nabla^2 \right) A_\mu = \mu_0 J_\mu \tag{3}$$

of the Lorentz invariant field equations with $\mu = 1, 2, 3, 4$. Here $A_\mu = (\mathbf{A}, i\phi/c)$ where $\mathbf{A}$ is the magnetic vector potential, ϕ the electrostatic potential, $c^2 = 1/\mu_0\varepsilon_0$ where $c \cong 2.998 \times 10^8$ m/s denotes the velocity constant of light determined by the magnetic permeability μ_0 and the dielectric constant ε_0, and $J_\mu = (\mathbf{j}, ic\bar{\rho})$ where $\mathbf{j}$ stands for the electric current density and $\bar{\rho} = \varepsilon_0 \mathrm{div}\, \mathbf{E}$ for the electric charge density. Since J_μ is relativistically invariant, it has to satisfy the condition

$$\mathbf{j}^2 - c^2\bar{\rho}^2 = const. \tag{4}$$

where the constant must vanish because J_μ disappears when there are no sources of charge and current density. This leads to the final form

$$J_\mu = \bar{\rho}\,(\mathbf{C}, ic) \tag{5}$$

where

$$\mathbf{C}^2 = c^2 \tag{6}$$

and $\mathbf{C}$ is a *velocity vector* with the modulus c.

In a three-dimensional representation the new extended *subatomic* field equations of the *vacuum* state become

$$c^2 \operatorname{curl} \mathbf{B} = (\operatorname{div} \mathbf{E})\, \mathbf{C} + \frac{\partial \mathbf{E}}{\partial t} \tag{7}$$

$$\operatorname{curl} \mathbf{E} = -\frac{\partial \mathbf{B}}{\partial t} \tag{8}$$

where

$$\mathbf{B} = \operatorname{curl} \mathbf{A}, \qquad \operatorname{div} \mathbf{B} = 0 \tag{9}$$

$$\mathbf{E} = -\nabla \phi - \frac{\partial \mathbf{A}}{\partial t}, \qquad \operatorname{div} \mathbf{E} = \bar{\rho}/\varepsilon_0 \tag{10}$$

As compared to conventional theory, these include the additional contributions from $\operatorname{div} \mathbf{E}$ due to ZPE in Equations (7) and (10), with the vector $\mathbf{C}$ of Equation (6) replacing the velocity constant c. This replacement is associated with the extension of the plane-wave representation of special relativity to a two-dimensional one, such as that of cylindrical geometry with an *incorporated* spin concept.

4. Resulting New Subatomic Properties

A number of new results have been obtained from Equations (3)–(10) which cannot be deduced in terms of the Standard Model. Corresponding particle models of steady axisymmetric states thus arise from a related generating function. As shown in Chapter 6 of [1], a radially convergent such function leads to vanishing net electric charge q_0 and magnetic moment M_0, whereas a divergent one results in net values of q_0 and M_0 under certain circumstances. In this section a number of examples [2] will be reconsidered.

4.1. Photon Model with Spin and Rest Mass

The solution for cylindrical waves in a frame (r, φ, z), with the velocity vector $\mathbf{C} = c(0, \cos\alpha, \sin\alpha)$, $\cos\alpha \ll 1$, and a constant angle α, leads to a *screw-shaped* configuration which includes spin and an associated very small but nonzero rest mass, as shown in Chapter 11 of [1]. The phase and group velocities become slightly smaller than c, the field geometry is *helical* with nonzero *axial* field components, and it becomes *limited* in space.

For a generating function with a convergent radial part there is an effective photon radius

$$\hat{r} = \frac{\varepsilon \lambda_0}{2\pi(\cos\alpha)} \tag{11}$$

with a main wavelength λ_0 of a corresponding wave packet, and a parameter $\varepsilon = 1$. As an illustration, $\cos\alpha \leqslant 10^{-4}$ and $\lambda_0 = 3 \times 10^{-6}$ m yields a photon rest mass $m_0 \leqslant 10^{-40}$ kg. The phase and group velocities then only deviate by a factor less than 5×10^{-9} from the velocity constant c. The spin thus exists at the expense of a very small reduction of the momentum which is related to the axial propagation.

There is also a photon mode originating from a generating function with a divergent radial part. A revised renormalization procedure is applied to this mode, to obtain finite values for the parameters of a wave packet as shown in Chapter 11.3.5 of [1] and in [12]. The

effective radius of Equation (11) is then obtained for $0 < \varepsilon \ll 1$. With $\varepsilon \leqslant \cos\alpha \leqslant 10^{-4}$ and $\lambda_0 = 3 \times 10^{-6}$ m we then have $\hat{r} \leqslant 5 \times 10^{-7}$ m. This represents a form of *needle radiation*.

4.2. The Elementary Charge

The main features of steady axisymmetric states can be deduced from the time-independent field equations of a separable generating function

$$F(r,\theta) = G_0 G(\rho,\theta) \qquad G = R(\rho)\cdot T(\theta) \tag{12}$$

in a spherical frame (r,θ,φ), where all relevant quantities are independent of the angle φ and $\rho = r/r_0$, with r_0, as a characteristic radial dimension. To arrive at a particle with net electric charge and magnetic moment, a divergent radial part

$$R = \rho^{-\gamma} e^{-\rho} \qquad \gamma > 0 \tag{13}$$

is chosen, in combination with a polar part T of top-bottom symmetry.

The divergence problem of infinite self-energy which arises in the resulting *point-charge-like* geometry, can be tackled by a process of *renormalization*. The conventional way of proceeding is described by Ryder [13] among others, implying that the divergent behaviour is outbalanced by adding extra *ad hoc* counter terms to the Lagrangian. In the present approach an alternative way is chosen, where the "infinity" of the divergent system is out balanced by the "zero" of a *counter-factor* [14]. Such a factor is already inherent in the present theory and has not to be imposed, as shown in Chapter 7.3 of [1].

Corresponding deductions have been performed on the electron, muon, and tauon, leading to the following results:

- There is a net electric charge $q_0 = Q_0 f_p$ where $Q_0 = (\varepsilon_0 ch)^{1/2} \simeq 8.86 \times 10^{-19}$ C and f_p is a dimensionless profile factor. Q_0 is related to the fine-structure constant, and it can be taken as an example where relativity is linked with quantum mechanics through the present theory.
- A variational analysis on the factor f_p finally results in a *minimum elementary charge* $q_0 = 1.60 \times 10^{-19}$ C within an uncertainty a few percent as compared to the experimental value of e [1, 15, 16].
- The product of the rest mass m_0 and the magnetic moment M_0 becomes

$$m_0 M_0 = (ch/4\pi)\left[1 + \left(e^2/4\pi\varepsilon_0 ch\right)\right] = 8.46 \times 10^{-34}\,\mathrm{kg}\cdot\mathrm{A}\cdot\mathrm{m}^2 \tag{14}$$

  This agrees with experimental data for $m_0 M_0$ of the electron, muon and tauon within the limit of a few percent.

The obtained characteristic charge Q_0 and the deduced minimum value of q_0 being close to the experimental value of the elementary charge e, thus suggests that the latter should be considered as a deduced quantity, and not as a fundamental and independent parameter.

4.3. The Z Boson and the Higgs Particle

The treatment of the vacuum as an empty space leads to a number of shortcomings, such as to a missing rest mass of elementary particles.

This point was made clear by P. W. Higgs and F. Englert among others. The theory by Higgs [17] is based on a *spontaneous nonlinear* mechanism of *symmetry breaking* of an empty vacuum state, by which an unstable boson of unspecified but large rest mass is being formed. This particle has zero net electric charge and zero spin. In its turn, the same particle is considered to decay into a set of all other lighter and massive elementary particles. An open point concerns the theoretically undetermined value of the rest mass.

A particle was later discovered at the projects ATLAS [18] and CMS [19] of CERN, being unstable, having vanishing net electric charge and spin, and with a rest mass of 125 GeV. This discovery was understood to be a confirmation of the heavy particle due to the theory by Higgs.

An alternative and different way of explaining the results by CERN has been presented by the author [20–22], as being characterized by *intrinsic linear broken symmetry*. It starts with a model of the Z boson determined from a convergent axially symmetric generating function. From superposition of the solutions of two such Z boson models with antiparallel spin directions, a composite model can be formed. With a mass of 91 GeV for each of the original Bosons, the composite particle obtains characteristical data given by lacking electric charge, magnetic field, and spin. It is purely electrostatic and highly unstable, and has a minimum mass close to 125 GeV. This appears to be in good agreement with the results by CERN. The composite particle solution is also consistent with the point made by Quigg [4] that the Higgs is perhaps not a truly fundamental particle, but is built out of as yet unobserved constituents.

4.4. Intrinsic Charges and the Strong Force

The local nonzero behaviour of $\operatorname{div}\mathbf{E}$ does not only generate a net integrated electric elementary charge e, but also intrinsic integrated electric charges $\pm Q_i$ of both polarities within various parts of the volume of an elementary particle [1, 2, 23]. This can be demonstrated by a model of an individual quark being deduced from a convergent generating function, in a frame of spherical coordinates (r, θ, φ) being independent of φ. We further consider a tentative model of the neutron, given by three individual quarks which are mutually bound to each other, to form a triangular configuration [24]. In a first simplified treatment equal models are used for these quarks.

The following points concern the model of an individual quark:

- In the triangular configuration each quark is assumed to have a mass of 5.57×10^{-28} kg being a third of the neutron mass.
- Integration of the local electric charge density over various parts of the quark volume results in large positive and negative intrinsic charges $\pm Q_i$ where $Q_i/e \cong 19.9$. Thus Q_i becomes an order of magnitude larger than the elementary charge.

Concerning the interaction between two quarks, the following points should be observed:

- The source terms of the present theory lead to a volume force density
$$\mathbf{f} = \bar{\rho}\,\mathbf{E}_i \qquad \mathbf{E}_i = \mathbf{E} + \mathbf{C} \times \mathbf{B} \tag{15}$$
Here part of the electric contribution $\mathbf{E}$ is outbalanced by the magnetic contribution $\mathbf{C} \times \mathbf{B}$. Therefore the total field $\mathbf{E}_i$ only

becomes noticeable within the innermost part of the quark volume. The result $(Q_i/e)^2 = 396$ implies that the interaction due to $\mathbf{E}_i$ would become more than two orders of magnitude larger than that arising between two elementary charges. But in the real situation the added influence of $\mathbf{C} \times \mathbf{B}$ partly outbalances that of $\mathbf{E}$.

- The total interaction between two quarks in the triangular configuration thus is of *short-range* character, and becomes about *two orders* of magnitude larger than that between two elementary charges.

- The mutual quark force and its corresponding work can be determined in terms of the distance between the quark centra. It is obtained from the force due to the local intrinsic charge density of quark number I, in combination with the reversed total field $\mathbf{E}_i$ generated by quark number II.

- When gradually shrinking the distance between the quark centra, a corresponding work of the mutual forces and their associated potential distributions is being traversed. This results in an outer potential barrier, followed by an intermediate well, and thus ending at an additional barrier. The mutual quark interaction thus becomes *stable* and *attractive*.

- An application to the neutron then leads to a well depth of about 7.7 MeV, being rather close to the binding energy of 8 MeV obtained from experiments reported by Bethe [24]. Since the additional net charges of the proton are comparable to the elementary charge, a similar result should also hold for the proton.

- In the triangular quark model an outer radius of about 3×10^{-15} m and a core radius of about 10^{-15} m are obtained. These values are comparable with a nuclear radius of 1.5×10^{-15} m given by experiments.

These deduced data are impaired by some uncertainties. Nevertheless the general outcome could still hold. The obtained short-range character and the order of magnitude of the attractive and stable interaction thus gives a clear indication that it should become possible to *unify* the fundamental phenomena of electromagnetics and the strong nuclear force.

4.5. Special Relativity versus Quantum Mechanics

In quantum mechanics an instantaneous behaviour of entangled states can take place through long-range interaction. A vacuum state of empty space leads on the other hand to a limited relativistic velocity propagation in subatomic physics. When $\operatorname{div} \mathbf{E} = 0$, Equations (7)–(10) thus result in a conventional transverse electromagnetic EM wave, with the velocity c. This is not reconcilable with instantaneous long-range interaction.

A possible way out of this dilemma [25] may be provided by the transition to a vacuum state with ZPE and $\operatorname{div} \mathbf{E} \neq 0$. Equations (7)–(10) then lead to two wave types. The first is an EMS nontransverse electromagnetic space-charge wave with $\operatorname{curl} \mathbf{E} \neq 0$ and a limited relativistic propagation determined by the velocity constant c. The second

type is an S wave of purely longitudinal electric space-charge character with curl $\mathbf{E} = 0$. This wave depends only on the dielectric constant ε_0, has *no* relation to relativity, and is not limited in its velocity of propagation, as defined by the vector $\mathbf{C}$ in Equation (7).

The EMS and S concepts are here proposed to be combined into a system which satisfies the requirements of long-range interaction. Thus, two spatially limited EMS particle models being at a long mutual distance become linked by an S mode which is not limited in its speed of transition. This would imply that relativity and quantum mechanics do not necessarily have to be in conflict. But it remains so far as an open question which requires more investigation. There are the remaining questions whether the S mode becomes a physical reality, and how the matching of the axial electric field components of the EMS and S modes can be realized in detail.

5. Conclusions

From the present revised subatomic field equations, new results have been obtained in terms of the Zero Point Energy. These results cannot be deduced from the conventional Standard Model. They concern the spin, rest mass and needle radiation of the photon, a deduction of the value of the elementary electric charge, and of the mass of the CERN particle. The latter deduction is not related to the theory by Higgs. The present theory has further debouched into the discovery of intrinsic electric charges and related forces acting within corresponding particle models. These forces give rise to a potential well depth being rather close to the binding energy of the neutron and proton. This provides a possibility of unifying electrodynamics and the strong nuclear force.

It is improbable that all these different obtained results should merely by chance happen to agree with experimentally confirmed facts.

Conflicts of Interest

The author declares no conflicts of interest regarding the publication of this paper.

References

[1] Lehnert, B. (2014) Revised Quantum Electrodynamics. In: Dvoeglazov, V.V., Ed., *Contemporary Fundamental Physics*, Nova Science Publishers, Inc., New York, 1-154.

[2] Lehnert, B. (2018) Impacts of Revised Quantum Electrodynamics on Fundamental Physics. *Journal of Electromagnetic Analysis and Applications*, **10**, 106-118. https://doi.org/10.4236/jemaa.2018.105008

[3] Stratton, J.A. (1941) Electromagnetic Theory. 1st Edition, Ch. 1.10 and 1.11, McGraw-Hill Book Comp., Inc., New York and London.

[4] Quigg, C. (2008) The Coming Revolution in Particle Physics. *Scientific American*, **298**, 46-53. https://doi.org/10.1038/scientificamerican0208-46

[5] Schiff, L.I. (1949) Quantum Mechanics. Ch. IV, Sec.13, McGraw-Hill Book Comp., Inc., New York, Toronto, London.

[6] Casimir, H.B.G. (1948) On the Attraction between Two Perfectly Conducting Plates. *Proceedings of the Koninklijke Nederlandse Akademie van Wetenschappen*, **51**, 793-795.

[7] Lamoreaux, S.K. (1997) Demonstration of the Casimir Force in the 0.6 to 6 μm Range. *Physical Review Letters*, **78**, 5-8. https://doi.org/10.1103/PhysRevLett.78.5

[8] Abbott, L. (1988) The Mystery of the Cosmological Constant. *Scientific American*, **258**, 106-113. https://doi.org/10.1038/scientificamerican0588-106

[9] Lehnert, B. (2014) Some Consequences of Zero Point Energy. *Journal of Electromagnetic Analysis and Applications*, **6**, 319-327. https://doi.org/10.4236/jemaa.2014.610032

[10] Lehnert, B. (2015) Zero Point Energy Effects on Quantum Electrodynamics. *Journal of Modern Physics*, **6**, 448-452. https://doi.org/10.4236/jmp.2015.64048

[11] Lehnert, B. (2016). On the Cosmical Zero Point Energy Density. *Journal of Modern Physics*, **7**, 1112-1119. https://doi.org/10.4236/jmp.2016.710100

[12] Lehnert, B. (2011) The Individual Photon in Two-Slit Experiments. *International Review of Physics*, **5**, 15-18.

[13] Ryder, L.H. (1996) Quantum Field Theory. 2nd Edition, Cambridge University Press, Cambridge.

[14] Lehnert, B. (2010) Deduced Fundamental Properties of the Electron. *International Review of Physics*, **4**, 1-6.

[15] Lehnert, B. and Scheffel, J. (2002) On the Minimum Elementary Charge of an Extended Electromagnetic Theory. *Physica Scripta*, **65**, 200-207. https://doi.org/10.1238/Physica.Regular.065a00200

[16] Lehnert, B. and Höök, J. (2010) An Electron Model with Elementary Charge. *Journal of Plasma Physics*, **76**, 419-428. https://doi.org/10.1017/S0022377809990638

[17] Higgs, P.W. (1966) Spontaneous Symmetry Breakdown without Massless Bosons. *Physical Review*, **145**, 1156-1168. https://doi.org/10.1103/PhysRev.145.1156

[18] ATLAS Collaboration. Aad, G., *et al.* (2012) Observation of a New Particle in the Search for the Standard Model Higgs Boson with the ATLAS Detector at the LHC. *Physics Letters B*, **716**, 1-29. https://doi.org/10.1016/j.physletb.2012.08.020

[19] CMS Collaboration. Chatrchyan, S., *et al.* (2012) Observation of a New Boson at a Mass of 125 GeV with the CMS Experiment at the LHS. *Physics Letters B*, **716**, 30-61. https://doi.org/10.1016/j.physletb.2012.08.021

[20] Lehnert, B. (2013) Higgs-Like Particle Due to Revised Quantum Electrodynamics. *Progress in Physics*, **3**, 31-32.

[21] Lehnert, B. (2014) Mass-Radius Relations of Z and Higgs-Like Bosons. *Progress in Physics*, **10**, 5-7.

[22] Lehnert, B. (2015) Minimum Mass of a Composite Boson. *Journal of Modern Physics*, **6**, 2074-2079. https://doi.org/10.4236/jmp.2015.614214

[23] Lehnert, B. (2017) Intrinsic Particle Charges and the Strong Force. *Journal of Modern Physics*, **8**, 1053-1066. https://doi.org/10.4236/jmp.2017.87067

[24] Bethe, H.A. (1947) Elementary Nuclear Theory. Ch. 2, John Wiley and Sons, Inc., New York and Chapman and Hall, Ltd., London, 118.

[25] Lehnert, B. (2018) Some Thoughts upon Long-Range Interaction and Entangled States. *Journal of Electromagnetic Analysis and Applications*, **10**, 193-196. https://doi.org/10.4236/jemaa.2018.1012015

Journal of Modern Physics, 2019, 10, 673-686
http://www.scirp.org/journal/jmp
ISSN Online: 2153-120X
ISSN Print: 2153-1196

Anisotropy of Stable Single Domain Ferrimagnetic Particles in a Rock Sample from Gyroremanent Magnetization and Comparison with Other Anisotropy Methods

Liam L. Belisle[1], David K. Potter[1*], Brendan C. Snow[1,2], Allyson L. Shewchuk[1]

[1]Department of Physics, University of Alberta, Edmonton, Canada
[2]CNOOC Petroleum North America ULC, Calgary, Canada
Email: *dkpotter@ualberta.ca

How to cite this paper: Belisle, L.L., Potter, D.K., Snow, B.C. and Shewchuk, A.L. (2019) Anisotropy of Stable Single Domain Ferrimagnetic Particles in a Rock Sample from Gyroremanent Magnetization and Comparison with Other Anisotropy Methods. *Journal of Modern Physics*, **10**, 673-686.
https://doi.org/10.4236/jmp.2019.106048

Received: April 28, 2019
Accepted: May 26, 2019
Published: May 29, 2019

Abstract

The orientation of stable single domain (SSD) ferrimagnetic particles in an igneous rock sample was determined by a sensitive technique utilizing gyroremanent magnetization (GRM). Components of GRM were measured in the sample upon exposure to an alternating field (AF) at various orientations in 3 orthogonal planes. The major components of GRM exhibited a $\sin(2\theta)$ dependence on AF orientation in the respective perpendicular planes. This was in accordance with theory [1] and contrary to some previously reported experimental results on magnetic recording tape, which produced a distorted $\sin(2\theta)$ dependence of the GRM [1]. The explanation is likely due to the SSD ferrimagnetic particles in the rock sample being more dispersed (less interacting) compared to the highly interacting SSD particles in the magnetic tape sample of the previous study. The GRM results were consistent with another remanence anisotropy method, anisotropy of isothermal remanent magnetization (AIRM). This method again measures the anisotropy of the remanence carrying ferrimagnetic particles, but the IRM is also acquired by larger multidomain (MD) particles as well as by the SSD particles. The results were also consistent with the visible rock anisotropy (petrofabric), the anisotropy of magnetic susceptibility (AMS), and the shear wave velocity anisotropy. A comparison of all the methods demonstrated that the fine SSD particles, which make up only a small proportion of the rock, were aligned in quite a similar orientation to that of the main rock forming minerals that constituted the bulk of the sample.

Keywords

Anisotropy, Gyroremanence, Isothermal Remanence, Magnetic Susceptibility,

Shear Wave Velocity

1. Introduction

Gyroremanent magnetization (GRM) is produced by exposing a sample containing an anisotropic distribution of fine ferro- or ferrimagnetic particles to a single alternating field (AF) application [1], or by exposing a sample containing an isotropic distribution of such particles to two successive applications of an AF [2]. GRM is theoretically only produced by stable single domain (SSD) remanence carrying particles [1]. These are the very particles that are most useful for both man-made recording processes, and for palaeomagnetic purposes for recording the magnitude and direction of the ancient geomagnetic field in rocks over geological time periods. By measuring the components of GRM produced when an AF is applied at various orientations in 3 orthogonal planes of a sample, it is possible to infer the orientation of the SSD particles in the sample. The method is the most sensitive remanence anisotropy method, and allows one to exclusively determine the anisotropic distribution of the SSD particles [3]. This means that GRM measurements represent a unique magnetic means of isolating the anisotropic distribution of SSD particles. This is important since an anisotropic distribution of these particles can deflect the natural remanent magnetization (NRM) in a rock sample away from the ancient field direction. This has potentially serious implications if the sample is used for palaeomagnetic purposes, since it could lead to errors in determining palaeomagnetic reconstructions and the behaviour (*i.e.*, palaeointensity and direction) of the Earth's ancient magnetic field. In contrast to GRM anisotropy, other anisotropy of magnetic remanence (AMR) methods may include remanence components from any multidomain (MD) ferro- or ferrimagnetic particles present in the sample [3] in addition to the components from the SSD particles. The MD components are generally less stable over geological timescales.

A key aim of the present paper is to show that GRM measurements can readily determine the anisotropy of SSD particles in a rock sample that was previously considered "quasi-isotropic" from acoustic anisotropy methods [4]. Previous GRM anisotropy studies have investigated magnetic recording tapes [1], dispersed particles from magnetic recording tapes [5], a weakly anisotropic rock sample with no visible anisotropy (petrofabric) [6], or a more strongly anisotropic rock sample, again with no visible petrofabric [3]. In the present paper the rock sample exhibited a clearly visible petrofabric arising from the alignment of the larger mineral grains (plagioclase and quartz) that constituted the bulk of the sample. This allowed us to determine whether the anisotropy of the SSD particles (which constitute a small fraction of the rock sample) from our GRM measurements was related to the overall observed petrofabric of the main rock forming minerals.

We also undertook 3 other quantitative anisotropy methods in order to help

verify the GRM anisotropy results of the SSD particles, and also to compare the SSD particle anisotropy with the overall anisotropy of the larger minerals comprising the bulk of the rock sample. These 3 methods were as follows:

- Anisotropy of isothermal remanent magnetization (AIRM), which determines the anisotropy of all the remanence carrying particles. This not only includes the SSD particles but also the larger MD particles.
- Anisotropy of magnetic susceptibility (AMS), which measures the combined AMS of all the minerals in the rock sample, including the main rock forming diamagnetic minerals (plagioclase and quartz), any paramagnetic minerals, as well as the remanence carrying ferrimagnetic minerals. In the present sample the AMS is dominated by the small fraction of ferrimagnetic particles.
- Anisotropy of shear-wave velocity. This mainly determines the anisotropy of the bulk matrix minerals (in this case mainly plagioclase and quartz).

The magnetic anisotropy methods (GRM, AIRM and AMS) allow a full 3 dimensional (3D) anisotropy to be measured on a single rock core plug sample. Most other anisotropy techniques require several samples oriented in different directions in order to generate 3D anisotropic information, since certain measurements can only be made in 1 dimension (1D) on a core plug (e.g., fluid permeability measurements), or in 2 dimensions (2D). The experimental set up for the shear wave velocity measurements only allows 2D anisotropy to be determined in one particular plane, as detailed in the Methods section below.

2. Sample

The rock sample, VOLC-B-Y, was taken from the Flin Flon Belt of the Trans-Hudson Orogeny in eastern Saskatchewan, west of the town of Flin Flon, Manitoba, and is from the Palaeoproterozoic Era (1.6 - 2.5 billion years ago). This area has been studied for some time due to the economic potential of the mineral deposits found nearby [4]. The cylindrical rock sample was 2.5 cm in diameter and 2 cm in length and is shown in Figure 1. The figure shows the sample both with and without the arbitrary sample axes (*X*, *Y*, *Z*) superimposed. The $+X$ direction has a declination of 0˚ (or 360˚) and an inclination of 0˚, the $+Y$ direction has a declination of 90˚ and an inclination of 0˚, and the $+Z$ direction has a declination of 0˚ and an inclination of 90˚.

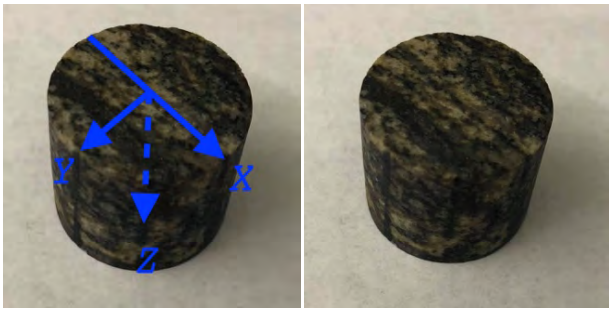

Figure 1. Sample VOLC-B-Y with (left) and without (right) the sample axes labeled. The directions of the arrows in the left hand figure indicate the $+X$, $+Y$ and $+Z$ directions.

The sample had a mass of 28.33 g and the following mineralogical composition: 61.2% plagioclase, 22.5% quartz, 8.3% biotite, 1.9% opaque minerals [4]. The ferrimagnetic particles, representing a very small fraction of the rock sample, are likely to be magnetite or titanomagnetite based on some initial tests, including remanence acquisition curves. We did not determine the Curie temperature of the ferrimagnetic particles for this sample as we did not want to heat the sample in case this induced chemical changes. The previous study by Cholach *et al.* [4] described this rock sample as being "quasi-isotropic" from their acoustic anisotropy studies. However, all our experimental results will demonstrate that the sample is significantly anisotropic.

3. Methods

3.1. Gyroremanent Magnetization (GRM) Anisotropy

This method applied an AF to the static sample at various orientations in 3 orthogonal planes [3]. This was achieved using an AF demagnetizer coil housed within a mumetal shield. The latter shielded the sample from the Earth's field. The sample was subjected to an AF of 60 mT at increments of 15˚ within a 180˚ range (from $\theta = -90^{\circ}$ to 90˚) in a particular plane (**Figure 2**). After the AF application, the sample was removed from the AF coil and the GRM components (x, y and z) were measured in a spinner magnetometer. Prior to each AF application the sample was tumble AF demagnetized in 80 mT and the remaining remanence measured, and subtracted from the subsequent GRM measurement. The demagnetizing field was higher than the AF used to impart the GRM in order to remove as much remanence as possible prior to each GRM production step. 13 pairs of magnetized and demagnetized values were obtained in the 3 orthogonal planes (XY, YZ, and ZX) giving a total of 39 measurements of GRM. For each measured plane the first listed axis was oriented at $\theta = 0^{\circ}$ and the second axis oriented at $\theta = -90^{\circ}$ or 90˚. The GRM method is extremely sensitive,

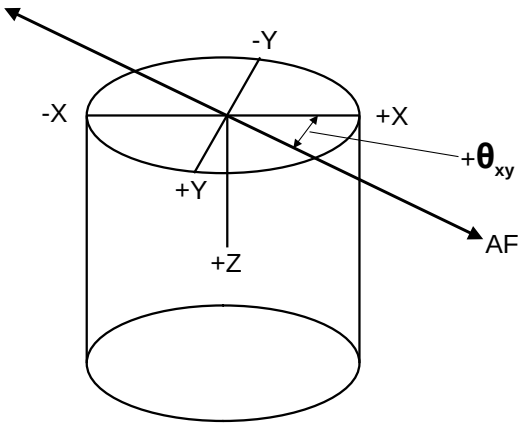

Figure 2. Example orientation of the AF axis with respect to the sample axes. The example shows the AF axis at an angle $+\theta_{XY}$ in the XY plane of the sample. This produces a GRM in the Z axis if the sample contains anisotropically distributed SSD ferrimagnetic particles in the XY plane.

but quite time consuming, taking a few hours to perform. It is effectively the remanence equivalent of the anisotropy of magnetic susceptibility (AMS) delineator (see the AMS section below), since it measures the differences in anisotropy of the SSD ferro- or ferrimagnetic particles in a particular plane, and can identify the orientations of the maximum and minimum SSD anisotropy axes within that plane. The GRM method does not, however, give the magnitudes of those axes.

3.2. Anisotropy of Isothermal Remanent Magnetization (AIRM)

This method applied a direct field (DF) to the sample to produce an isothermal remanent magnetization (IRM). This was achieved by placing the sample inside a pulse magnetizer, and applying a DF of about 100 ms duration. The resulting IRM components (x, y and z) were then measured in a spinner magnetometer. This procedure was undertaken in 3 orthogonal directions along the X, Y, and Z sample axes. This produced a total of 9 tensor components from which a 3D AIRM ellipsoid could be calculated giving the magnitudes and directions of the 3 principal anisotropy axes [3] [7]. The sample was tumble AF demagnetized before each magnetization step.

The pulse magnetization was carried out at two different DF strengths, 20 mT and 60 mT, in order to determine the anisotropy of different ferrimagnetic particle size populations. The higher field affects the SSD ferrimagnetic particles as well as the MD ferrimagnetic particles, whereas the lower field only affects the larger MD ferrimagnetic particles (the lower field is below the anisotropy field of the SSD particles). A typical AIRM determination from the 3 magnetization and 3 demagnetization steps takes around 30 minutes.

3.3. Anisotropy of Magnetic Susceptibility (AMS)

This method determines a 3D AMS ellipsoid for the sample. The sample was placed in an anisotropy delineator and rotated successively in 3 orthogonal planes in a low (500 μT) magnetic field. If the sample is anisotropic a sinusoidal voltage of twice the rotation frequency is induced in pick up coils. The amplitude of the voltage is proportional to the difference between the maximum and minimum susceptibilities in the sample plane perpendicular to the rotation axis. By adding a bulk magnetic susceptibility value to the anisotropy delineator results the magnitudes and orientations of the 3 principal AMS axes can be determined. The bulk value was measured along the Z sample axis (see **Figure 1** and **Figure 2**) using a magnetic susceptibility bridge. The sample is inserted into the coil of the bridge, which changes the coil's inductance, and this is proportional to the sample's magnetic susceptibility. The 3D AMS measurements are very rapid, with the anisotropy delineator measurements taking about a minute and the bulk susceptibility measurement taking a few seconds (with a background reading followed by a sample reading).

3.4. Observed Petrofabric

The visible rock anisotropy (petrofabric) was observed using a hand lens. This

visible petrofabric reflected the alignment of the larger component grains (plagioclase and quartz) of the sample.

3.5. Anisotropy of Shear Wave Velocity (ASWV)

2D measurements of shear wave anisotropy were possible in the XY plane of the sample. Two parallel planar transducers were placed on the flat end faces (which were oriented in the XY plane) of the cylindrical sample plug. Whilst the overall wave train propagated along the axis of the plug (the Z axis), the shear waves had a transverse motion in the perpendicular XY plane. By rotating the sample plug in the XY plane with respect to the transducers, as per the method described in [8], it was possible to detect shear wave anisotropy in the XY plane. A shear wave was propagated through the sample by one of the transducers and detected by the other, and the shear wave arrival time was recorded. Then the sample was rotated through 22.5˚ in the XY plane and a shear wave was again propagated through the sample. This process was repeated every 22.5˚ as the XY plane was rotated about 360˚. The shear wave arrival times were recorded, and the velocities determined at each orientation to create a 2D plot of the shear wave velocity anisotropy in the XY plane.

4. Results and Discussion

4.1. Gyroremanent Magnetization (GRM) Anisotropy

Application of the AF at various angles in the XY, YZ and ZX planes of the sample caused GRM components to be acquired perpendicular to each plane along the Z, X and Y axes respectively (**Figures 3-5**) consistent with GRM theory [1]. **Figures 3-5** demonstrate that the variation in magnitude of the GRM largely followed a $\sin(2\theta)$ shape in each case (from the red fitting curves), where θ was the orientation of the applied AF as shown in **Figure 2**, in accordance with GRM theory [1]. This was in contrast to some previous experimental results for a sample comprising magnetic tape [1] which exhibited a "distorted" $\sin(2\theta)$ curve. The SSD particles in the magnetic tape sample from [1] were highly interacting, since they were densely coated on the plastic tape. In contrast, the SSD particles in our natural rock sample are expected to be more dispersed and therefore less interacting. This may explain why we obtained undistorted $\sin(2\theta)$ GRM curves for our natural sample, similar to results for man-made samples containing dispersed (non-interacting) SSD particles [5].

The GRM curves allow one to determine the predominant alignment of the SSD particles within each plane. **Figure 3** shows that the z-component of the GRM was negative when the AF was oriented at $\theta = -90^\circ$ to -15° and when $\theta = 75^\circ$ to 90° in the XY plane, and positive when the AF was oriented at $\theta = -15^\circ$ to 75° in that plane (the equation of the best fit curve through the data points is $y(x) = 50\sin(2x + \pi/6)$ where x is the horizontal axis and y is the vertical axis). According to GRM theory [1] this indicates that the SSD ferrimagnetic particles in the rock sample are aligned closer to the X axis (oriented at $\theta = 0^\circ$) than the Y

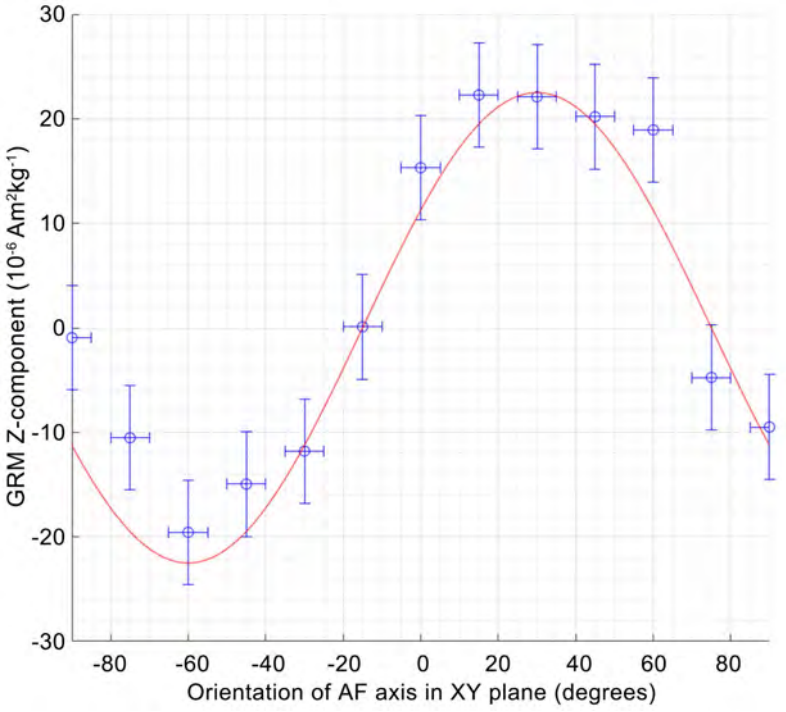

Figure 3. The z-components of GRM for orientations of the AF axis in the *XY* plane. The results indicate that the maximum alignment axis of the SSD particles in the *XY* plane occurs at an AF orientation of $\theta = -15^{\circ}$ (the AF orientation where GRM is zero in the positive slope part of the GRM curve), close to the *X* axis.

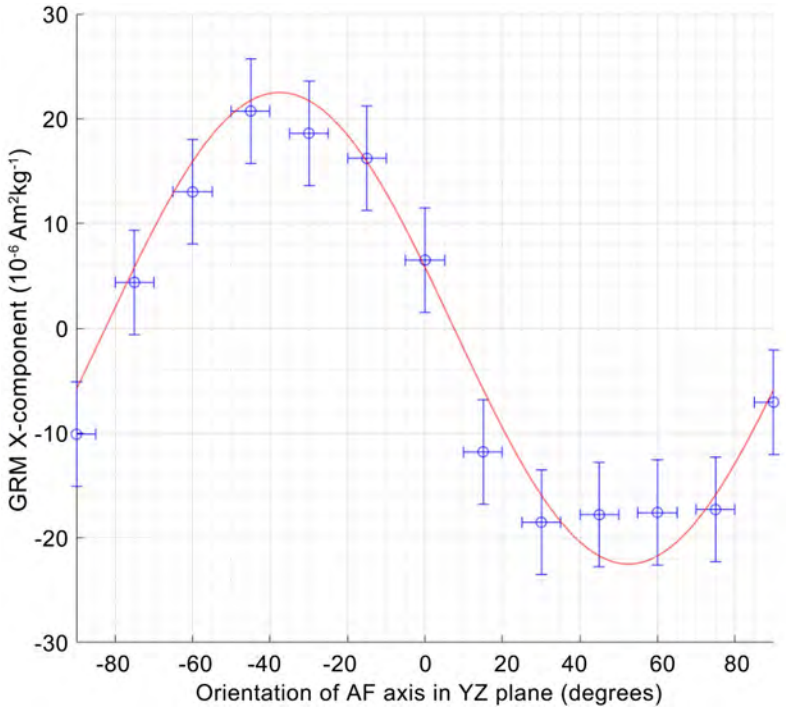

Figure 4. The x-components of GRM for orientations of the AF axis in the *YZ* plane. The results indicate that the maximum alignment axis of the SSD particles in the *YZ* plane occurs at an AF orientation of $\theta = -82.5^{\circ}$ or 97.5° (the AF orientation where GRM is zero in the positive slope part of the GRM curve), close to the *Z* axis.

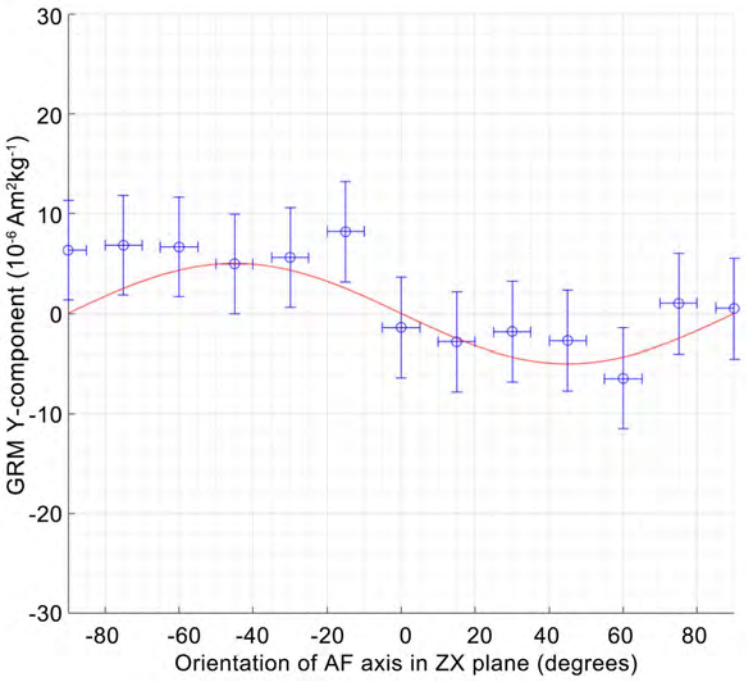

Figure 5. The y-components of GRM for orientations of the AF axis in the *ZX* plane. The results indicate that the maximum alignment axis of the SSD particles in the *ZX* plane occurs at an AF orientation of $\theta = -90^\circ$ or 90° (the AF orientation where GRM is zero in the positive slope part of the GRM curve), identical to the *X* axis.

axis (oriented at $\theta = -90^\circ$ or 90°). The maximum principal (*i.e.*, preferred alignment) axis of the SSD particles in the *XY* plane occurs at an AF orientation of $\theta = -15^\circ$ (the AF orientation where the GRM is zero in the positive slope part of the GRM curve), which is close to the X axis.

Figure 4 shows that the *x*-component of the GRM was negative when the AF was oriented at $\theta = -90^\circ$ to -82.5° and when $\theta = 7.5^\circ$ to 90° in the *YZ* plane, and positive when the AF was oriented between $\theta = -82.5^\circ$ to 7.5° in that plane (the equation of the best fit curve through the data points is $y(x) = 50\sin(2x + \pi/12)$). According to GRM theory [1] this indicates that the SSD ferrimagnetic particles in the rock sample are aligned closer to the *Z* axis (oriented at $\theta = -90^\circ$ or 90° in this case) than the *Y* axis (oriented at $\theta = 0^\circ$). The maximum principal axis of the SSD particles in the *YZ* plane occurs at an AF orientation of $\theta = -82.5^\circ$ or 97.5° (the AF orientation where the GRM is zero in the positive slope part of the GRM curve), which is very close to the Z axis.

Likewise Figure 5 shows that the *y*-component of the GRM was negative when the AF was oriented at $\theta = 0^\circ$ to 90° in the *ZX* plane, and positive when the AF was oriented at $\theta = -90^\circ$ to 0° (the equation of the best fit curve through the data points is $y(x) = 15\sin(2x)$). According to GRM theory [1] this indicates that the SSD ferrimagnetic particles are slightly more aligned along the *X* axis (oriented at $\theta = -90^\circ$ or 90° in the *ZX* plane) than the *Z* axis (oriented at $\theta = 0^\circ$) given that the GRM magnitudes in Figure 5 are much less than those for the previous two planes shown in Figure 3 and Figure 4. The maximum principal axis of the SSD

particles in the ZX plane occurs at an orientation of $\theta = -90^\circ$ or 90° (the AF orientation where the GRM is zero in the positive slope part of the GRM curve), which is identical to the X axis in the ZX plane.

Thus the combined GRM results indicate that the maximum principal anisotropy axis of the SSD ferrimagnetic particles (*i.e.*, the preferential alignment axis) is close to the X sample axis, the intermediate principal anisotropy axis is close to the Z sample axis, and the minimum principal anisotropy axis is close to the Y sample axis.

4.2. Comparison with Other 3D Anisotropy Results (AIRM and AMS)

Table 1 shows the orientations (declinations and inclinations) and magnitudes (both the absolute and normalized magnitudes) of the three principal AIRM axes for both the 20 mT and 60 mT DF strengths. The orientations of the principal anisotropy axes determined at the two field strengths are very similar. This demonstrates that the SSD ferrimagnetic particles (which are preferentially affected by the higher field) are aligned in a very similar orientation to the MD ferrimagnetic particles (which are preferentially affected by the lower DF). The percentage AIRM, 100 [(max − min)/(max + int + min)], for a DF of 20 mT is slightly larger at 26% than for a DF of 60 mT at 18%. This may be due to the MD ferrimagnetic particles being more aligned than the smaller SSD ferrimagnetic particles, or the MD ferrimagnetic particles may be slightly more elongated, or it could merely be due to the non-linear acquisition of IRM with applied field strength [7].

The orientations of the principal AIRM axes compare well with the GRM results.

Table 1. The magnitudes and orientations (Dec = Declination, Inc = Inclination) of the 3 principal anisotropy axes of the rock sample from 3D Anisotropy of Isothermal Remanent Magnetization (AIRM) and Anisotropy of Magnetic Susceptibility (AMS) measurements.

Anisotropy Technique	Principal Axes				
	Axes	IRM Magnitude (10^{-3} Am^2kg^{-1})	Normalised Magnitudes	Dec (˚)	Inc (˚)
AIRM (20 mT)	Max.	35.45	0.46	349.7	0.5
	Int.	26.53	0.34	254.0	84.9
	Min.	15.78	0.20	259.7	−5.1
AIRM (60 mT)	Max.	70.03	0.42	344.3	7.0
	Int.	55.22	0.34	210.0	80.0
	Min.	39.50	0.24	255.2	−7.1
		Mass Magnetic Susceptibility (10^{-8} m^3kg^{-1})			
AMS	Max.	2478.9	0.39	353.4	−2.7
	Int.	2172.8	0.35	291.0	84.1
	Min.	1638.2	0.26	263.1	−5.2

Both techniques show that the orientations of the principal anisotropy axes are close to the X, Y and Z sample axes, with the X axis being the maximum axis (largest IRM magnitude), the Z axis intermediate, and the Y axis being the minimum axis.

Table 1 also shows the orientations and magnitudes (absolute and normalized) of the three principal AMS axes. The orientations of the principal AMS axes compare well with the GRM results and AIRM principal axes. The AMS magnitudes were also consistent with the GRM and AIRM results. The X axis had the largest magnetic susceptibility, the Z axis was intermediate, and the Y axis had the minimum magnetic susceptibility.

The AMS results represent the sum effect of all the minerals (diamagnetic, paramagnetic, ferrimagnetic etc.) in the sample. In our sample the AMS signal is dominated by the ferrimagnetic fraction. The percent AMS is slightly lower (at 13%) than for the AIRM results. This is likely due to the sample containing both SSD and MD ferrimagnetic particles. Uniaxial SSD ferrimagnetic particles have a maximum magnetic susceptibility perpendicular to the long axes of the particles, whereas MD ferrimagnetic particles have a maximum magnetic susceptibility along the long axes of the particles [7] [9]. Thus for a mixture of SSD and MD particles with the same alignment orientation (as the AIRM results show in Table 1) the AMS results from each set of particles can partially cancel (in the present sample) or substantially cancel each other out (in some other cases) thus reducing the % AMS.

The main visible petrofabric lineations on the rock are oriented close to the X axis (declination = 0˚ or 360˚) in the XY plane as seen in Figure 1. The GRM results of Figure 3 indicated that the SSD ferrimagnetic particles are preferentially aligned in a very similar orientation at $\theta = -15^{\circ}$ (declination = 345˚ for comparison with values in Table 1) in the XY plane. This relatively small difference in orientation between the visible rock fabric and the alignment of the SSD ferrimagnetic particles may not be significant given the uncertainty bars shown on the GRM plots. Alternatively, the small difference may be real if the SSD particles are not aligned exactly with the overall rock fabric of the larger plagioclase and quartz grains. The lineations in XY also appear to extend in the Z axis, suggesting a somewhat planar fabric in the ZX plane, consistent with the X and Z axes being the maximum and intermediate axes from the GRM, AIRM and AMS results.

4.3. Anisotropy of Shear Wave Velocity and Comparison with Other Anisotropy Results in the *XY* Plane

Since the shear wave velocity anisotropy measurements could only be performed in 2D in the XY plane we will compare the shear wave results with the visible petrofabric and GRM results in the XY plane. We will also compare this 2D data with the 3D data from the AIRM and AMS results. The 2D shear wave velocity results in the XY plane are plotted in Figure 6 and fit with a least squares fitting method, which generated an 8^{th} degree polynomial to fit the dataset. The results

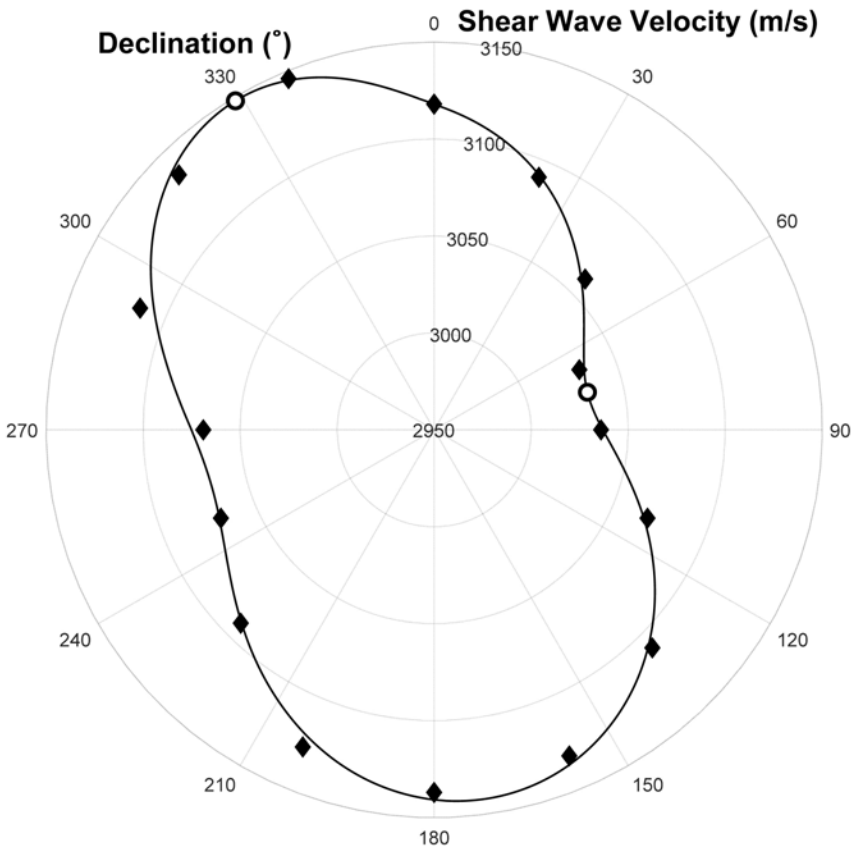

Figure 6. Shear wave velocity results at various orientations in the *XY* plane of the rock sample. Experimental data points (black diamonds) were fit with a least squares curve fitting program (black curve). The circles at declinations 329˚ and 76˚ are the maximum and minimum velocities respectively from the fitting curve.

form a "figure of 8" pattern, demonstrating anisotropy in the *XY* plane. If the sample had been isotropic in the *XY* plane then the results would have formed a circle. From the best fit curve the declination of the maximum shear wave velocity axis was at 329˚ (or −31˚ anticlockwise from 0˚) with a magnitude of 3148 m/s, and the minimum axis was at 76˚ with magnitude of 3030 m/s. It is not presently clear why the shear wave velocity results do not form a perfectly symmetrical "figure of 8". It might be due to slight differences in the coupling of the transducers to the sample during each experimental measurement.

The orientation of the maximum principal axis from the shear wave anisotropy results (declination = −31˚ or 329˚ from the best fit curve) is not too far from that of the GRM results (declination = −15˚ or 345˚). If one considers the maximum experimental shear wave value at a declination = −22.5˚ or 337.5˚ (rather than the maximum value derived from the fitting curve) then the difference between the shear wave and GRM results is even less. The shear wave results show that the overall rock anisotropy from the main rock forming minerals (plagioclase and quartz) has quite a similar orientation to that of the small fraction of SSD ferrimagnetic particles (from the GRM results). One possible reason for the relatively small difference between the orientation of the maximum axis from

the shear wave results compared to the GRM results could be the different sampling frequency in the *XY* plane (every 22.5˚ for the acoustic measurements, and every 15˚ for the GRM measurements). Alternatively, the difference could be real if the small fraction of SSD ferrimagnetic particles are not aligned in exactly the same orientation as the overall rock fabric. Whilst there is a close correspondence between the orientation results for the different methods for this sample (Table 2), it may not always be the case for other samples. The advantage of performing all the different methods described here is that it allows one to determine the anisotropy of the different mineral types and, in the case of the ferrimagnetic fraction, different particle size fractions (SSD versus MD etc.).

Table 2 shows a comparison of the results for all the anisotropy methods in the *XY* plane. The declination and inclination of the maximum and minimum principal axes is quite similar for all the methods. For the results based on 2D data the inclinations are nominally 0˚ since no information in the third dimension is included. For the results based on 3D methods we give the maximum and minimum principal axes (which were very close to the *XY* plane) based on the full 3D data, and so these determinations include small inclinations. The results demonstrate that the orientations of the fine SSD and MD ferrimagnetic particles (from the GRM, AIRM and AMS results) are quite similar to those of the main rock forming minerals plagioclase and quartz (from the shear wave velocity anisotropy and visible petrofabric).

Table 2. The orientations of the maximum and minimum principal axes in the *XY* plane from the various anisotropy techniques. Negative declination values are anticlockwise from 0˚ or 360˚ (e.g., −10.3 is the same as 349.7 for comparison with Table 1), and are given for easy comparison with the GRM plots of Figures 3-5.

Anisotropy Technique in *XY* Plane	Principal Axis in *XY* Plane	Declination (degrees)	Inclination (degrees)
Shear Wave Anisotropy from 2D Measurements	Maximum	−31* (−22.5)†	0.0
	Minimum	76.0* (67.5)†	0.0
GRM at 60mT from 2D Measurements	Maximum	−15.0	0.0
	Minimum	75.0	0.0
Visual Petrofabric from 2D Observations	Maximum	0.0	0.0
	Minimum	90.0	0.0
AIRM at 20 mT from 3D Measurements	Maximum	−10.3	0.5
	Minimum	79.7	−5.1
AIRM at 60 mT from 3D Measurements	Maximum	−15.7	7.0
	Minimum	75.2	−7.1
AMS from 3D Measurements	Maximum	−6.6	−2.7
	Minimum	83.1	−5.2

*From the shear wave best fit curve. †From the individual shear wave velocity values.

5. Conclusions

1) The magnitudes of the primary GRM components for the natural rock

sample studied here exhibited a $\sin(2\theta)$ dependence on AF axis orientation in respective perpendicular planes. This was consistent with theory [1] and previous experiments on man-made samples [5] for non-interacting SSD particles, and contrary to the distorted $\sin(2\theta)$ experimental GRM curve previously reported for interacting SSD particles on magnetic recording tape [1].

2) The sign of the GRM with AF orientation in the XY, YZ and ZX planes indicated that the magnitudes of the three principal axes of the SSD particles in the rock sample were in the order $X > Z > Y$.

3) The orientations of the principal anisotropy axes from the GRM results were consistent with those determined from anisotropy of isothermal remanent magnetization (AIRM) and indicated that the alignment of MD ferrimagnetic particles was similar to that of the smaller SSD ferrimagnetic particles. Anisotropy of magnetic susceptibility (AMS), which measures the combined effect of all the minerals in the sample, but is dominated in this case by the ferrimagnetic particles, also gave principal axes whose orientations were consistent with those from the GRM and AIRM results.

4) The orientation of the overall rock anisotropy of the main rock forming minerals (dominated by plagioclase and quartz), as determined by both the visual petrofabric and quantitative shear wave velocity anisotropy results, was also consistent with the magnetic anisotropy results (GRM anisotropy, AIRM and AMS, which were all dominated by the ferrimagnetic particles). This indicated that the main rock forming minerals for the sample studied were aligned in quite similar orientations to the smaller amount of fine grained ferrimagnetic particles.

5) The results from all methods indicated that the sample is significantly anisotropic, and is not "quasi-isotropic" as suggested from acoustic measurements by a previous study [4].

Acknowledgements

D. K. P. thanks the Natural Sciences and Engineering Research Council of Canada (NSERC) for a Discovery Grant.

Conflicts of Interest

The authors declare no conflicts of interest regarding the publication of this paper.

References

[1] Stephenson, A. (1980) *Nature*, **284**, 49-51. https://doi.org/10.1038/284049a0

[2] Edwards, J. (1982) *Geophysical Journal of the Royal Astronomical Society*, **71**, 199-214. https://doi.org/10.1111/j.1365-246X.1982.tb04993.x

[3] Potter, D.K. (2004) A Comparison of Anisotropy of Magnetic Remanence Methods—A User's Guide for Application to Paleomagnetism and Magnetic Fabric Studies. In: Martin-Hernandez, F., Luneburg, C.M., Aubourg, C. and Jackson, M., Eds., *Magnetic Fabric: Methods and Applications*, Geological Society, London, Spe-

cial Publications, 21-35.

[4] Cholach, P.Y., Molyneux, J.B. and Schmitt, D.R. (2005) *Canadian Journal of Earth Sciences,* **42**, 533-554. https://doi.org/10.1139/e04-094

[5] Stephenson, A. and Potter, D.K. (1987) *IEEE Transactions on Magnetics*, **23**, 3820-3830. https://doi.org/10.1109/TMAG.1987.1065524

[6] Stephenson, A. (1981) *Physics of the Earth and Planetary Interiors*, **25**, 163-166. https://doi.org/10.1016/0031-9201(81)90149-7

[7] Stephenson, A., Sadikun, S. and Potter, D.K. (1986) *Geophysical Journal of the Royal Astronomical Society*, **84**, 185-200. https://doi.org/10.1111/j.1365-246X.1986.tb04351.x

[8] Snow, B.C. (2018) Nanoparticle Magnetic Characterization and Comparison of Rock Anisotropy Methods. MSc Thesis, University of Alberta, Alberta, 95.

[9] Potter, D.K. and Stephenson, A. (1988) *Geophysical Research Letters*, **15**, 1097-1100. https://doi.org/10.1029/GL015i010p01097

Nomenclature

AF:	Alternating Field
AIRM:	Anisotropy of Isothermal Remanent Magnetization
AMS:	Anisotropy of Magnetic Susceptibility
AMR:	Anisotropy of Magnetic Remanence
ASWV:	Anisotropy of Shear Wave Velocity
DF:	Direct Field
GRM:	Gyroremanent Magnetization
IRM:	Isothermal Remanent Magnetization
MD:	Multidomain
NRM:	Natural Remanent Magnetization
SSD:	Stable Single Domain
X, *Y*, *Z*:	The *X*, *Y* and *Z* axes of the sample (see **Figure 1** and **Figure 2**)
XY, *YZ*, *ZX*:	The *XY*, *YZ* and *ZX* planes of the sample
x, *y*, *z*:	The *x*, *y* and *z* components of magnetic remanence

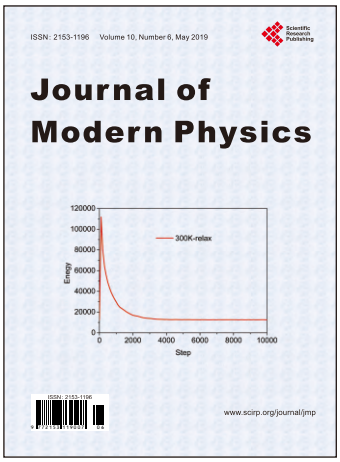

Call for Papers

Journal of Modern Physics

ISSN: 2153-1196 (Print) ISSN: 2153-120X (Online)
http://www.scirp.org/journal/jmp

Journal of Modern Physics **(JMP)** is an international journal dedicated to the latest advancement of modern physics. The goal of this journal is to provide a platform for scientists and academicians all over the world to promote, share, and discuss various new issues and developments in different areas of modern physics.

Editor-in-Chief

Prof. Yang-Hui He City University, UK

Subject Coverage

Journal of Modern Physics publishes original papers including but not limited to the following fields:

Biophysics and Medical Physics
Complex Systems Physics
Computational Physics
Condensed Matter Physics
Cosmology and Early Universe
Earth and Planetary Sciences
General Relativity
High Energy Astrophysics
High Energy/Accelerator Physics
Instrumentation and Measurement
Interdisciplinary Physics
Materials Sciences and Technology
Mathematical Physics
Mechanical Response of Solids and Structures
New Materials: Micro and Nano-Mechanics and Homogeneization
Non-Equilibrium Thermodynamics and Statistical Mechanics
Nuclear Science and Engineering
Optics
Physics of Nanostructures
Plasma Physics
Quantum Mechanical Developments
Quantum Theory
Relativistic Astrophysics
String Theory
Superconducting Physics
Theoretical High Energy Physics
Thermology

We are also interested in: 1) Short Reports—2-5 page papers where an author can either present an idea with theoretical background but has not yet completed the research needed for a complete paper or preliminary data; 2) Book Reviews—Comments and critiques.

Notes for Intending Authors

Submitted papers should not have been previously published nor be currently under consideration for publication elsewhere. Paper submission will be handled electronically through the website. All papers are refereed through a peer review process. For more details about the submissions, please access the website.

Website and E-Mail

http://www.scirp.org/journal/jmp **E-mail: jmp@scirp.org**

What is SCIRP?

Scientific Research Publishing (SCIRP) is one of the largest Open Access journal publishers. It is currently publishing more than 200 open access, online, peer-reviewed journals covering a wide range of academic disciplines. SCIRP serves the worldwide academic communities and contributes to the progress and application of science with its publication.

What is Open Access?

All original research papers published by SCIRP are made freely and permanently accessible online immediately upon publication. To be able to provide open access journals, SCIRP defrays operation costs from authors and subscription charges only for its printed version. Open access publishing allows an immediate, worldwide, barrier-free, open access to the full text of research papers, which is in the best interests of the scientific community.

- High visibility for maximum global exposure with open access publishing model
- Rigorous peer review of research papers
- Prompt faster publication with less cost
- Guaranteed targeted, multidisciplinary audience

Scientific Research Publishing

Website: http://www.scirp.org

Subscription: sub@scirp.org

Advertisement: service@scirp.org